Technische Universität München

Physik Department E20

Molecular Nanoscience and Chemical Physics of Interfaces

Scanning tunneling microscopy investigation of structure and electronic properties of surface-confined tetrapyrrolic species

Dissertation

Alissa Charlotte Wiengarten

Technische Universität München

Lehrstuhl E20 - Molekulare Nanowissenschaften und Chemische Physik von Grenzflächen

Scanning tunneling microscopy investigation of structure and electronic properties of surface-confined tetrapyrrolic species

Alissa Charlotte Wiengarten

Vollständiger Abdruck der von der Fakultät für Physik der Technischen Universität München zur Erlangung des akademischen Grades eines Doktors der Naturwissenschaften genehmigten Dissertation.

Vorsitzender: Univ.-Prof. Dr. J. Leo van Hemmen

Prüfer der Dissertation: 1.   Univ.-Prof. Dr. Johannes V. Barth

                         2.   Univ.-Prof. Dr. Joost Wintterlin,

                              Ludwig-Maximilians-Universität München

Die Dissertation wurde am 24.06.2015 bei der Technischen Universität München eingereicht und durch die Fakultät für Physik am 21.07.2015 angenommen.

Abstract

On-surface chemical reactions and the adsorption behavior of functional molecules on metal surfaces are studied; aiming for the formation of covalent nanostructures and derivatives of molecules with enhanced properties. For a future application in devices and the creation of new two-dimensional materials it is required to understand the processes on surfaces on the molecular level. In this work, the structural and electronic properties of tetrapyrrolic molecules are investigated in a well-defined environment, namely on single crystal surfaces in an ultra-high vacuum chamber, by means of scanning tunneling microscopy and complementary methods.

Catalyzed by a silver substrate, covalent oligomeric nanostructures are formed on the surface for different porphyrin molecules. The coupling leads to a decrease of the electronic band gap and the properties of the structures can further be tuned by the incorporation of a metal ion in the tetrapyrrolic macrocycle. Intramolecular ring-closing reactions are observed, with different product distributions for metalated and metal-free porphyrins.

The adsorption-induced change of the symmetry and electronic structure of a molecule is described for iron-phthalocyanine on a copper surface. Furthermore, for two metallo-porphyrins adsorbed on a silver surface the binding affinity towards small gas molecules is studied, motivated by the functionality of heme in oxygen transport.

Finally, the intermolecular interactions in a model system for a bimolecular organic solar cell are investigated.

II

Contents

1 Introduction

One of the first laboratory experiments was the inclined plane built by Galileo Galilei. He paved the way for the subsequent history of laboratory systems that in some way reduced a phenomenon to its basic traits or reproduced it in a controlled manner with the goal to understand its fundamental principles. This concept is of invaluable importance for science, as research had been limited to descriptive observations of phenomena before. By far shorter is the history of surface science employing metal, semiconductor and insulator surfaces as its laboratory systems and aiming to understand the processes that take place at interfaces.

Although some pioneering studies focus on several effects related to surfaces and interfaces such as the work of Irving Langmuir on adsorption chemistry and kinetics, [1] the discovery of the photo effect [2] and of electron diffraction, [3] only in the 1960ies surface science became a field of research on its own. This breakthrough was triggered by mainly three inventions, namely electron spectroscopy as a surface-sensitive tool, vacuum chambers enabling to retain clean surfaces and slightly later computers that allow complex modeling. [4] Only 20 years later the invention of the scanning tunneling microscope (STM) allowed to atomically resolve conducting surfaces and structures on surfaces. [5] This ability was extended to insulating surfaces with the invention of the atomic force microscope. [6]

Surface science deals with the characterization of solid-vacuum and solid-liquid interfaces, where the topmost $10\,\text{Å}$ of a bulk material are regarded as the surface region. Processes on surfaces are investigated, such as adsorption, desorption, diffusion and self-organization. Furthermore, the electronic structure of surfaces is explored as well as the growth and properties of thin films. Surface science also contributes to the field of heterogeneous catalysis with studies on surface reactions and the catalytic activity of adsorbates. [7,8] The most prominent application is the fabrication of semiconductor devices where it is important to understand the interfacial processes. As foreseen by Richard Feynman, [9] the structure size in electronic and optoelectronic devices is still shrinking which requires an understanding of the components on the atomic level. Porphyrin molecules came into the focus of surface science studies because of their relevance in many biological systems and their versatile tunable properties. [10] The macrocycle consisting of four pyrrole rings which are connected by methine groups is very stable and can host different metal ions. As part of hemoglobin, porphyrins with an iron center are responsible for the oxygen transport in blood. [11] Magnesium porphyrins on the other hand play an important role in the photosynthesis in plants. [12] These and other characteristic features of porphyrins enabled a variety of applications. Due to their ability to coordinate small gas molecules porphyrins are employed as gas sensors, [13–15] whereas their optical properties are explored for artificial photosynthesis, [16] organic solar cells, [17] light emitting diodes [18] and photosensitizers in photodynamic therapy. [19] Moreover, porphyrins are employed as catalysts. [20, 21] Their properties can further be tuned by adding different substituents at the macrocycle and

upon adsorption on metal surfaces the substrate often acts as an additional ligand. [10]
Recently, porphyrins became part of extensive research on molecular systems suitable for the
employment in molecular electronics [22] and optoelectronics. In order to overcome the limi-
tations in structural size for semiconductor materials functional properties of single molecules
are explored, such as switching or rectifying. [22, 23] For the application in a device these func-
tional units need to be connected to allow an efficient charge transport. [24] For this reason,
covalent coupling reactions between a variety of molecules on metal surfaces have been investi-
gated. [25, 26] Furthermore, the goal is to create new two-dimensional materials. [27, 28]

In this work, functional molecules as porphyrins are studied in a well-defined environment, *i.e.*
the laboratory system is an ultra-high vacuum chamber where the sample is cooled in order
to reduce thermal motion and increase spectral resolution. A scanning tunneling microscope
enables to characterize the geometric structure of the molecules, probe their electronic states
and study the intermolecular interactions.

The concept of this approach is to understand the basic properties of a system before designing
a device or application. The adsorption of a molecule on a metal surface can drastically change
its properties due to the strong interaction with the substrate. Its geometry can be distorted in
comparison to the gas phase conformation, [29, 30] the electronic states are shifted and broad-
ened because of the interaction with the metal [31] or the magnetic properties of a molecule can
be influenced by the substrate. [32, 33] It was also shown that the catalytic activity of adsorbed
molecules depends on their adsorption site [34] as well as their affinity to bind ligands is influ-
enced by the substrate. [35, 36]

This work shows that the interaction with the underlying metal can have a substantial impact
on the functionality of adsorbed molecules and needs to be investigated in a well-defined envi-
ronment in order to understand and tune the properties of a future device.

In the following chapters different molecular systems are discussed and characterized mainly by
STM and several complementary techniques. The mode of operation and theory of STM are
elucidated in chapter 2 (ch.). Furthermore, the instrumentation of the ultra-high vacuum system
is explained as well as the sample preparations. The chapter finishes with the short introduction
of the complementary methods.

In the third chapter, on-surface chemical reactions involving different porphine molecules are
investigated. Porphines are the macrocycle of each porphyrin molecule and they can host a
metal ion in their center. Heat-induced and surface-assisted covalent coupling reactions are
observed for non-metalated porphines on Ag surfaces and for Co-porphines as well, leading to
the formation of covalently coupled oligomers. With the introduction of bromine atoms at the
periphery of the molecules a more directed growth of the nanostructures is aimed for.

Chapter 4 deals with intramolecular ring-closing reactions on tetraphenylporphyrins on a Ag(111)
surface. Enhancing the symmetry of the core of the molecule by the incorporation of a metal

ion in the center changes the reaction outcome. A very similar molecule, the diphenylporphyrin, undergoes the same ring-closing reactions and couples covalently at elevated temperatures.

In the following chapter, the surface-induced symmetry reduction apparent in STM images of a molecule similar to porphyins, namely Fe-phthalocyanine, is discussed. Moreover, polymerization reactions on the Cu(111) surface are observed.

Chapter 6 addresses the reactivity of surface-anchored metallo-porphyrins towards small ligands. The interaction with the metal substrate strongly influences the binding affinity of the metal centers and their catalytic activity.

At last, a model system for a bimolecular organic solar cell is investigated. The interaction of the two compounds is studied on the Ag(111) surface and the electronic band gap is measured. The results are summarized in the conclusion.

2 Experimental Methods

The main experimental technique employed in this work is scanning tunneling microscopy (STM). Its theory, the working principle and the experimental details are elucidated in the following. Furthermore, several other techniques were applied by coworkers in joint efforts to substantiate some of the findings obtained during the STM measurements. A brief overview about these complementary methods is given in the last part of this chapter.

## 2.1 Scanning Tunneling Microscopy

The current arising from electrons tunneling between a sharp metal tip and a conducting surface due to an applied bias depends exponentially on the vacuum gap width between tip and surface. This relation was first measured by Binnig and Rohrer in 1982 [37] and let to their invention of the scanning tunneling microscope (STM). [5] The STM enables to acquire images of conducting surfaces, structures on these surfaces and adsorbates with atomic resolution. [5, 38] Since the tunneling current depends exponentially on the distance between tip and surface, the topography of a surface can be measured by scanning the surface with the tip in a two-dimensional pattern. Either the tunneling current or the vacuum gap width are kept constant and the variation in the respective other parameter gives the surface topography.
In 1986, Binnig and Rohrer were awarded the Nobel Prize for their invention. [39] Since then, a very wide field of research based on the STM evolved, *e.g.* the characterization of metal and semiconductor surfaces, [38] of adsorbates on surfaces, [40] of molecular orbitals [41] and spin-polarized STM. [42]
In the following, the theory of STM, the different modes of operation and the instrumentation are summarized.

2.1.1 Theory of Scanning Tunneling Microscopy

The first theoretical description of electron tunneling between two solids was given by Bardeen in 1961. [43] He calculated the tunneling current by evaluating the time-dependent many-particle wave function of the whole system. After the first STM was put into operation Tersoff and Hamann employed Bardeen's method to calculate the tunneling current of an STM and the local density of states (LDOS) of several surfaces. [44, 45] Although their theory is only correct for tip-surface distances of several Å and tips exhibiting s-wave character, it explains the imaging of surface reconstructions, scattered waves of surface states and defects. The following description gives a summary of this first approach by Tersoff and Hamann. However, several different theories were developed up to now, which account for a wide range of experimental observations (for an overview see [46, 47]).
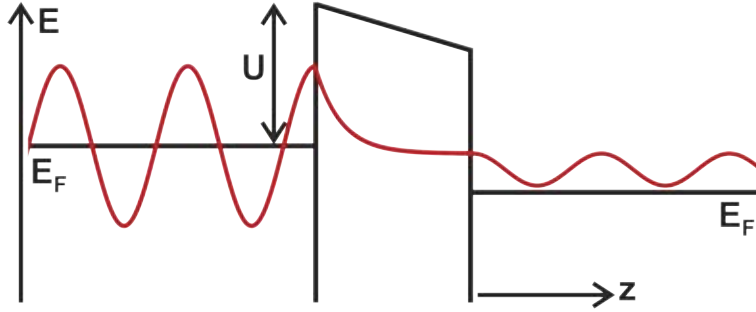
Figure 2.1: *One-dimensional tunneling junction: Shape of the wave function of electrons tunneling through the vacuum gap between two metals.*

The imaging in STM relies on electrons overcoming a certain potential barrier U, namely the work function of the respective material. In classical mechanics electrons cannot overcome a potential barrier that is higher than their own energy E, thus it cannot explain the phenomenon of tunneling. However, in quantum mechanics electrons are described by wave functions ψ obeying the Schrödinger equation

$$-\frac{\hbar^2}{2m}\frac{d^2}{dz^2}\psi(z) + U(z)\psi(z) = E\psi(z)$$

where m is the electron mass and the direction of z is shown in figure 2.1 (fig.). This equation has solutions for $U < E$ as well as for the case of $U > E$, *i.e.* if the potential barrier is higher than the energy of the electrons they can still penetrate into the barrier with a certain probability which exponentially decays with z [47] (see fig. 2.1).

Bardeen [43] described the tunneling of electrons between two electrodes A and B, separated by a vacuum barrier, by solving the Schrödinger equation of the combined system:

$$i\hbar\frac{\partial\psi}{\partial t} = \left(-\frac{\hbar^2}{2m}\frac{\partial^2}{\partial z^2} + U_A + U_B\right)\psi$$

where ψ is the wave function of the whole system and U_A and U_B are the potential functions of the two electrodes (see fig. 2.2).

Since there is a certain probability for electrons tunneling from electrode A to B, the wave function of the whole system ψ is calculated by first order perturbation theory:

$$\psi = \psi_\mu e^{-\frac{iE_\mu t}{\hbar}} + \sum_{\nu=1}^{\infty} c_\nu(t)\psi_\nu e^{-\frac{iE_\nu t}{\hbar}}$$

where ψ_μ is the wave function of electrode A with eigenvalues E_μ and ψ_ν is the wave function of electrode B with eigenvalues E_ν, t is the time and $c_\nu(t)$ are the coefficients that need to be
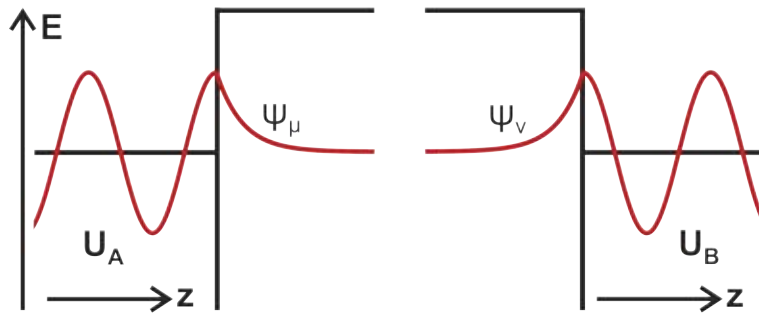
Figure 2.2: *One-dimensional tunneling junction: Wave functions of tip and sample.*

determined from the Schrödinger equation of the whole system and which give the tunneling probability.

Based on Bardeen's theory, Tersoff and Hamann [44, 45] gave an expression for the tunneling current between the two electrodes A (tip) and B (surface):

$$I = \frac{2\pi e}{\hbar} \sum_{\mu,\nu} f(E_\mu)(1 - f(E_\nu + eV))|M_{\mu\nu}|^2\delta(E_\mu - E_\nu). \tag{2.1}$$

The function $f(E)$ is the Fermi function, V is the applied bias and $|M_{\mu\nu}|^2$ is the tunneling matrix element derived by Bardeen and it is proportional to the tunneling probability. The δ-function in the end of equation 2.1 (eq.) accounts for the condition of elastic tunneling, *i.e.* electrons can only tunnel into states of the same energy.

As a first approximation, it is assumed that the applied biases are small and that the temperature is small, such that the Fermi function becomes a step function. It follows that

$$I = \frac{2\pi}{\hbar}e^2V \sum_{\mu,\nu} |M_{\mu\nu}|^2\delta(E_\nu - E_F)\delta(E_\mu - E_F) \tag{2.2}$$

where E_F is the Fermi energy.

The equation for the tunneling current can be further simplified by assuming that the tip is point like. Consequently, I is independent of the wave function of the tip ψ_μ:

$$I \propto \sum_\nu |\psi_\nu(\vec{r_0})|^2\delta(E_\nu - E_F) = \rho_s(\vec{r_0}, E_F). \tag{2.3}$$

Thus, if the tip is assumed to be featureless, the tunneling current is proportional to the local density of states $\rho_s(\vec{r_0}, E_F)$ of the surface at $\vec{r_0}$ and at the energy E_F. This finding will be compared to a more detailed calculation of I in the following.

In order to calculate I from eq. 2.2, Tersoff and Hamann calculated the tunneling matrix element

which was given by Bardeen:

$$M_{\mu\nu} = \frac{\hbar^2}{2m} \int d\vec{S} \ (\psi_\mu^* \vec{\nabla} \psi_\nu - \psi_\nu^* \vec{\nabla} \psi_\mu).$$ (2.4)

The integral is evaluated on a surface S which has to lie in the vacuum gap between tip and surface.

$M_{\mu\nu}$ is calculated by firstly giving an expression for ψ_ν by expanding it and secondly assuming that the tip is spherical at the apex and thus exhibits s-wave character which gives an expression for ψ_μ. Therefore, this assumption is only valid for small tip radii, on the other hand, for broader tips a more detailed description about the local conformation would be required.

Inserting the expressions for the two wave functions into eq. 2.4 and thus into eq. 2.2 gives an experimentally accessible expression of the tunneling current:

$$I = \frac{32\pi^3}{\hbar} e^2 V \phi^2 D_t(E_F) \ \frac{R^2}{\kappa^4} e^{2\kappa R} \times \sum_\nu |\psi_\nu(\vec{r_0})|^2 \delta(E_\nu - E_F)$$ (2.5)

where ϕ is the work function of the tip, D_t is the density of states (DOS) per unit volume of the tip, R is the tip radius and $\kappa = \frac{\sqrt{2m\phi}}{\hbar}$ is the minimum inverse decay length of the wave functions in vacuum.

If values typical for many metals are inserted, the conductance σ amounts to:

$$\sigma = \frac{I}{V} = 0.1 R^2 e^{2\kappa R} \rho_s(\vec{r_0}, E_F)$$ (2.6)

with ρ_s being the LDOS of the surface:

$$\rho_s(\vec{r_0}, E_F) = \sum_\nu |\psi_\nu(\vec{r_0})|^2 \delta(E_\nu - E_F).$$

As $|\psi_\nu(\vec{r_0})|^2 \propto e^{-2\kappa(R+d)}$ was derived during the expansion of ψ_ν, it follows that

$$\sigma \propto e^{-2\kappa d}$$

where d is the distance between tip and surface. The same exponential dependence was measured by Binning and Rohrer in their first STM experiments. [37] Furthermore, eq. 2.6 gives the same proportionality as eq. 2.3, *i.e.* the proportionality of the tunneling current is the same if the tip is assumed to be point-like. Thus, in this model the properties of the tip are assumed to be known (namely point-like or s-wave character) and with this the tunneling current only depends on the electronic structure of the surface and the tip-surface distance. If the tunneling current is held constant, a convolution of the electronic states of the surface and its topography is recorded. However, in order to understand the imaging of structures, it is necessary to take into account the electronic states of the tip as well since the conductance measured in STM is a convolution

of the electronic states of the sample and the tip. [47]
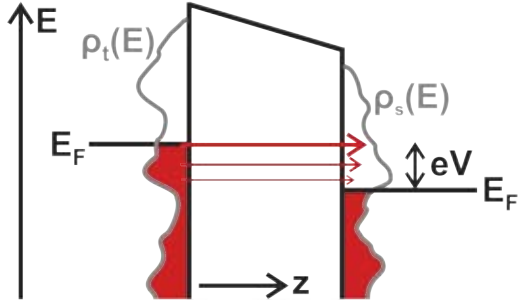
Figure 2.3: *Tunneling junction with positive bias applied to the sample: Electrons tunnel from occupied states of the tip into unoccupied states of the surface.*

Figure 2.3 shows schematically how the tunneling process is influenced by the DOS of both tip and sample. If a bias eV is applied to the sample the two Fermi levels are not aligned anymore but shifted towards each other by eV. In the case of positive bias in fig. 2.3 electrons can tunnel from occupied states of the tip into unoccupied states of the surface. The electrons close to the Fermi energy contribute most to the tunneling current which is marked by the thicker red arrow since they have the highest energy. If the polarity of the applied bias is inverted the electrons tunnel from occupied states of the sample into unoccupied states of the tip.

2.1.2   Scanning Tunneling Spectroscopy

Since the tunneling current in STM depends on the density of electronic states of the surface, the STM enables to investigate not only the topography of a surface but also its electronic structure. Whereas in the normal scanning mode, all electronic states up to eV contribute to the tunneling current, in scanning tunneling spectroscopy (STS) only a small energy range is chosen to contribute to the tunneling process. STS was first proposed by Selloni *et al.* in 1985 [48] and they computed how the derivative of the tunneling current I is related to the electronic states of the surface using a simplified tunneling model. The first tunneling spectra were recorded by Binnig *et al.* on the Ni(100) surface. [49] In general, STS can be employed to study surface states and resonances, [50, 51] catalytically active sites on the surface [52] and energy levels of adsorbed molecules. [41]

Based on the calculations summarized above the change in I in dependence of the applied bias V can be calculated by using the Wentzel-Kramers-Brillouin (WKB) approximation. [53] In the previous chapter I was calculated under the assumption that the applied bias is small. However, in STS measurements larger biases are applied to the tunneling junction. Thus, all electronic

states up to an energy of eV contribute to I in the WKB-approximation:

$$I \propto \int_0^{eV} \rho_s(E)\rho_t(E)T(E,eV)dE \qquad (2.7)$$

where ρ_t is the DOS of the tip which is assumed to be constant since clean metallic tips often exhibit this feature. T is the transmission probability and it accounts for the exponential dependence of I on the tip-surface distance:

$$T(E,eV) = e^{-2\kappa d}.$$

Differentiating eq. 2.7 with respect to V gives [53,54]:

$$\frac{dI}{dV} \propto e\rho_s(eV)T(eV,eV) + e\int_0^{eV} \rho_s(E)\frac{d}{d(eV)}(T(E,eV))dE. \qquad (2.8)$$

The integral describes the V-dependence of $T(E,eV)$ which is a monotonically increasing function in the WKB-approximation. Therefore, the integral in eq. 2.8 gives a continuous background in the dI/dV signal which is proportional to the DOS of the surface at the applied bias. Consequently, by measuring the derivative of I the electronic states of the surface can be probed with submolecular resolution. The ability to position the tip precisely over certain features and to probe the electronic states on a very small lateral scale has great advantages in comparison to space-averaging techniques such as photoemission spectroscopy. [53] Moreover, with STS both occupied and unoccupied states can be probed.

Experimentally, STS can be realized in two different ways. The first method is to keep the tip-surface distance constant while the applied bias is continuously altered in a certain range. The recorded tunneling current is differentiated with respect to the bias. [54] As shown above, the derivative is proportional to the DOS of the surface.

The second method makes use of a small modulation voltage which is superimposed with the applied dc bias V_{dc} between tip and surface. The modulation voltage exhibits sinusoidal shape and its frequency ω has to be larger than the feedback loop cut-off. Thus, I is modulated by ω but the feedback loop does not correct the tip-surface distance and the ac signal of I gives the derivative. The component of I which is in phase with ω, measured with a lock-in amplifier, directly gives the dI/dV signal at V_{dc}. [49,53,55]

Spectroscopy can be either performed at one particular site on the surface or an ST spectrum can be acquired at each point of the image. If the modulation bias technique is used to record the dI/dV signal at a certain V_{dc} over a small two-dimensional area, it will be referred to as dI/dV mapping in the following.

2.1.3   Modes of operation

The two most employed modes of operation in order to acquire topography images are described in the following. More specialized modes are described elsewhere. [56]

Constant current mode

In the constant current mode the height of the tip over the surface is adjusted in such a way that the tunneling current is constant during the x-y scan over the surface. A feedback loop applies a voltage to the piezo which controls the z-movement of the tip and thus alters the height of the tip in order to keep the tunneling current constant. From the voltage applied to the z-piezo the topography at each point of the surface can be determined. For this operation mode the surface does not have to be atomically flat, *i.e.* steps and adsorbates can easily be imaged. However, the scanning speed is limited by the response time of the feedback loop. [5, 56]

Constant height mode

The constant height mode enables faster scanning speeds since the feedback loop is open in order to keep the height of the tip over the surface constant during the x-y scan. [57] The topography of the surface is derived from the change in the tunneling current at each point. The disadvantage of this mode is that the surface has to be very flat so that the tip does not crash into the surface during scanning. Furthermore, to avoid drift a high stability is required.

2.1.4   Instrumentation

The STM utilized in this work was developed by G. Meyer, S. Zöphel and K. Schaeffer at the Freie Universität Berlin [58, 59] and is commercially available from CreaTec Fischer & Co. GmbH. [60] It is installed in an ultra-high vacuum (UHV) chamber and usually operated at $6\,\text{K}$. In the following, the UHV chamber with its different components and the STM scanner itself are described. Subsequently, the sample preparation is addressed.

UHV chamber

In order to investigate surfaces via STM a very clean environment, *e.g.* UHV, is required. At ambient pressures, small molecules such as water, oxygen and carbon monoxide easily cover metal surfaces or even react with them. If the pressure is decreased the number of particles per unit volume decreases and the mean free path of the particles increases. As a rough estimation, it is assumed that the surface is investigated over a time span of $10^4\,\text{s}$ and that the desired maximal coverage with adsorbates during this time is $\frac{1}{100}$ of a monolayer. It follows that the pressure has to be $5 \cdot 10^{-12}\,\text{mbar}$. These low pressures are very hard to achieve and since most of the remaining gas molecules do not change the surface structure pressures in the range of $10^{-10}\,\text{mbar}$ are sufficient for the majority of the experiments. [61]
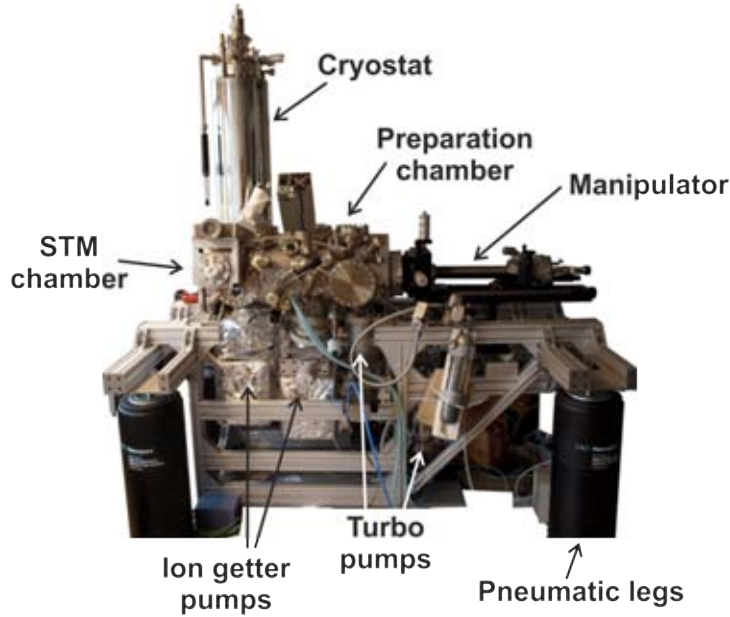
Figure 2.4: *UHV chamber: STM chamber with cryostat on the left and preparation chamber on the right. At the bottom of the chamber the turbo and ion getter pumps are mounted. The whole frame is placed on four pneumatic legs. Adapted from [62].*

The UHV system used for this work consists of two chambers, namely the preparation chamber and the STM chamber with a cryostat on top (see fig. 2.4). The chambers are connected via a gate valve. The UHV condition is achieved by several pumps. A dry diaphragm pump accomplishes a pressure of 1 mbar in the first stage of the pumping system so that the first turbo molecular pump (from Alcatel [63]) can be operated. It is followed by the main turbo pump (from Leybold [64]) which is directly connected to the preparation chamber. Turbo molecular pumps are able to maintain UHV conditions by rotating tilted blades mounted to the rotor and inducing a flow of the remaining particles out of the chamber. [61] Furthermore, in each chamber one ion getter pump further decreases the pressure by ionizing the residual gases with field-emitted electrons and accelerating them onto a titanium (Ti) electrode where they react with the Ti and stick to a getter plate. Another method to decrease the pressure is the evaporation of cerium (Ce). If the walls of the chamber are covered with Ce, remaining particles can react with the Ce and are trapped at the walls. At last, the Ti sublimation pump decreases the pressure for several hours when Ti is deposited onto a getter plate which is cooled by liquid nitrogen. With the combination of these pumps the usual base pressure is $5 \cdot 10^{-10}$ mbar. The pressure in both chambers is monitored by cold cathode gauges from Pfeiffer. [63] They ionize gas molecules and the resulting ion current is a measure for the amount of gas molecules in the chamber and thus for the pressure. [8]

The preparation chamber is equipped with several tools for sample preparation and cleaning. A

sputter gun ionizes Ar atoms which can be dosed into the chamber via a leak valve. After clean-
ing the sample, the crystallinity can be examined via low energy electron diffraction (LEED).
With a quadrupole mass spectrometer (from Scientific Instruments [65]) the composition of the
residual gases in the chamber or the purity of other gases dosed via leak valves can be deter-
mined.

The molecules required for most of the experiments are evaporated onto the sample via organic
molecular beam epitaxy (OMBE), *i.e.* the molecules are evaporated from a quartz crucible which
is heated resistively. In order to increase the molecular flux the temperature of the crucible is
increased. Furthermore, different metals can be deposited onto the surface. Cobalt (Co) and
iron (Fe) can be evaporated from a wire which is coiled around a tungsten (W) filament that is
heated resistively. Moreover, Fe was also evaporated by electron bombardment from an electron
beam evaporator with the following parameters: $I_{filament} = 1.66\,\text{A}$, $I_{emission} = 13\,\text{mA}$, Flux =
$2.0\,\text{nA}$, $U = 675\,\text{V}$, $t_d = 2\,\text{min}$.

Additionally, up to five sample holders can be stored inside the preparation chamber or a load-
lock can be employed so that different crystals can be studied without breaking the vacuum.

The sample holder is positioned on the manipulator which can be moved from the preparation
chamber into the STM chamber and it can be cooled with liquid helium, either during sample
preparation or in order to pre-cool the sample for the STM measurements. In the STM chamber
the STM scanner is mounted in direct contact to a cryostat which is cooled with liquid helium.
The outer part of the cryostat is filled with liquid nitrogen as a first cooling shield. The inner
part is filled with liquid helium and both parts are equipped with aluminum (Al) radiation
shields. The STM is located inside a radiation shield which is directly attached to the inner part
of the cryostat and thus the whole STM scanner can be stabilized at an equilibrium temperature
of $6\,\text{K}$. Since the pressure gauge in the STM chamber is outside of the radiation shield where
the temperature is higher, it is assumed that the pressure inside the shield is even lower than
measured by the gauge.

The whole system with both chambers is connected via a frame which is positioned on four
pneumatic legs. When inflated with air, they damp low frequency vibrations from the building
and the ground.

STM scanner

The configuration of the STM scanner is shown in fig. 2.5a. The purpose of this beetle-type
design was rigidity and simplicity. [66] The sample is positioned on the base plate on which
three piezo electric tubes are glued. The piezo electric effect enables a very precise control
of the tip movement. If a voltage is applied to a piezo electric material it is deformed in a
certain direction. [47] Since the length scale of the deformation amounts to several Å/V at
low temperatures movements with subatomic resolution can be induced in a controlled way.
The three piezo electric tubes are each contacted with four metal electrodes from the outside

(for triggering the x-y movement) and one from the inside (for triggering the z-movement, see fig. 2.5b). On top of each tube a sapphire sphere is mounted. The tip is positioned above the sample and it is fixed to a ramp that lies on the three sapphire spheres. The coarse movement of the tip is realized by the three piezo tubes. For this purpose the ramp is divided into three equal parts each of which is slightly inclined. If the same voltage is applied to the three piezos and if the deformation is slow and uniform the ramp follows the movement of the piezos. A net displacement of the ramp is achieved by a slow deformation of the piezos followed by a fast deformation in another direction. The ramp cannot follow the faster movement because of its inertia and if both steps are repeated after each other the ramp is displaced relatively to the piezos. Since the three segments of the ramp are inclined a movement in z-direction is realized as well. The tip is mounted on the inner piezo in the center of the ramp which is responsible for the fine movement of the tip. [59]
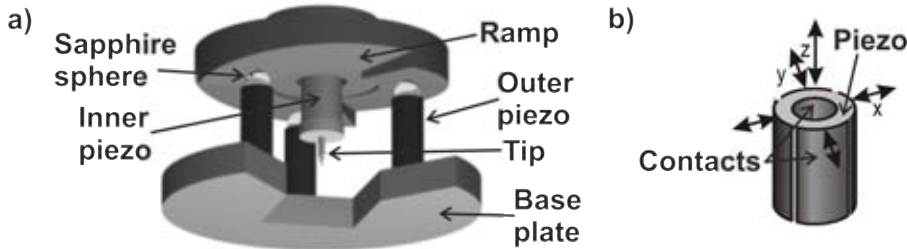
Figure 2.5: *a) STM scanner with tip attached to ramp and outer piezos on base plate. The coarse movement of the ramp is triggered by the outer piezos and the fine movement during scanning by the inner piezo. b) Outer piezo with electrical contacts. By applying voltages the piezo tube can be deformed in all three directions of space. Taken from [59].*

The base plate with the STM scanner is hanging at three long soft springs that are attached to the cryostat (see fig. 2.6). During cooling the base plate is pressed against a plate which is in direct contact with the inner cryostat. The STM scanner can be released to hang freely at the three springs via a pulling mechanism which can be operated from outside. In order to minimize vibrations the scanner is released during measurements. Vibrations of buildings are in the range from 1 to 100 Hz. Both the pneumatic legs and the springs damp these low frequency vibrations. Another method to further decrease the coupling of the STM with low frequency vibrations is to keep the resonance frequency of the whole STM scanner as high as possible by designing it to be rigid. [47] Additionally, three magnets placed below the base plate act as eddy current dampers.

The tips used in this work are chemically etched W tips. They are fabricated by mounting a W wire (diameter: 0.25 mm) in such a way that it hangs in the center of a loop of a gold wire (see fig. 2.7). In the loop a thin film of NaOH solution (2 mol/L) is created by dipping it into a

Figure 2.6: *Picture of the STM scanner without cooling shield and without sample. The tip is in the center above the block for the sample holder with six metal contacts. Two outer piezos are visible on the base plate and the three long springs that are attached to the cryostat. Picture taken by Knud Seufert.*

solution. The W wire is hold from the top and the part below the loop should be longer than the length required for the tip. An electro-chemical cell is realized by applying a voltage between the W wire and the wire of the loop (3 to 4.5 V). Thus, the part of the W wire in the solution is etched and W-oxide is created. The following chemical reaction takes place:

$$W(s) + 2OH^- + 2H_2O \rightarrow WO_4^{2-} + 3H_2(g)$$
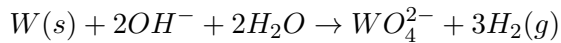
The part of the W wire in solution becomes thinner during the etching process until the waist is thin enough so that it cannot hold the weight of the bottom part anymore and it falls. The bottom part should be caught so that it can be used as a tip. Since the etching slowly removes the material and in the end there is a very high strain at the waist, this technique usually yields very sharp tips. [47] After etching the tip needs to be cleaned immediately with distilled water to remove the solvents and by sputtering the W-oxide is removed. Both parts of the W wire can be used as a tip. The W wire is slightly bent in a zig-zag fashion in order to hold it rigidly in the tip holder.

In the vacuum chamber the tip is cleaned by argon (Ar) ion sputtering. During the STM measurements the tip needs to be frequently treated as well since it often changes the structure at the apex by interaction with the substrate or residual gases. For this purpose a bias higher than usually used during measurements, *i.e.* up to 10 V is applied between tip and sample or the current is increased in order to strengthen the tip-surface interaction. Thus, the tip can pick up material from the surface or drop adsorbates from the apex of the tip. Another procedure is to bring the tip into physical contact with the surface. If the surface below the tip is clean metal the tip can be covered with that metal which is desired in many cases (see *e.g.* ch. 2.1.2). It is
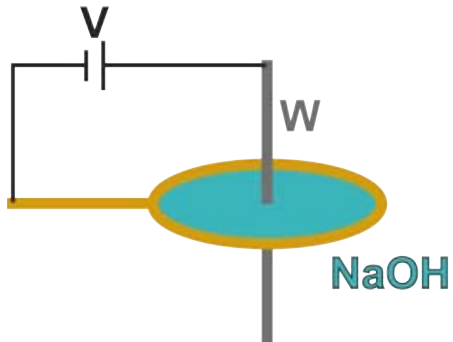
Figure 2.7: *Etching of a W tip in a film of NaOH solution. The gold wire is the counter electrode of the electro-chemical cell.*

also possible to apply a combination of both methods. However, the structure at the apex of the tip cannot be changed in a controlled way and is mostly unknown. [53] A commonly used method to test if the tip is metallic at the apex is to record a tunneling spectrum on a bare metal surface. Silver (Ag) and copper (Cu) surfaces exhibit characteristic surface states. [67, 68] If no other peaks are observed in the dI/dV curve the tip is assumed to be suited for spectroscopy. The scanning of the tip over the surface is controlled by a digital signal processor (DSP) (see fig. 2.8). The tunneling current I is amplified and converted into a voltage and this voltage is converted into a digital signal. The feedback loop compares the voltage resulting from the tunneling current to the preset value for the tunneling current and applies a voltage to the piezos in order to adjust the tip-sample distance such that the tunneling current stays constant. The voltage signal for the piezos is amplified to achieve the desired movement. Furthermore, the DSP controls the bias between tip and sample. The STMAFM 2.0 software [60] enables to adjust all parameters for scanning and for dI/dV measurements which are acquired by using an internal lock-in amplifier with $V_{rms} = 18\,\text{mV}$ and $f = 2.97\,\text{kHz}$.

2.1.5   Sample preparation

Single crystal cleaning

The different metal crystals were cleaned in UHV environment by several cycles of Ar ion sputtering and annealing. The Ar^+ ions are generated by backfilling the chamber with Ar gas ($2.5 \cdot 10^{-5}\,\text{mbar}$) through a leak valve and ionizing the gas particles with an ion gun by electron impact ionization. The applied voltage of the sputter gun is usually $800\,\text{V}$. The charged particles are accelerated towards the crystal and collide with the surface where they remove material from the surface. Consequently, other adsorbates on the surface are either sputtered away or they can be buried deeper below the surface. [61] During sputtering the current given by the Ar^+ ions is measured to be around $4.5\,\mu A$. Subsequently, the crystal is annealed at $720\,\text{K}$. During annealing
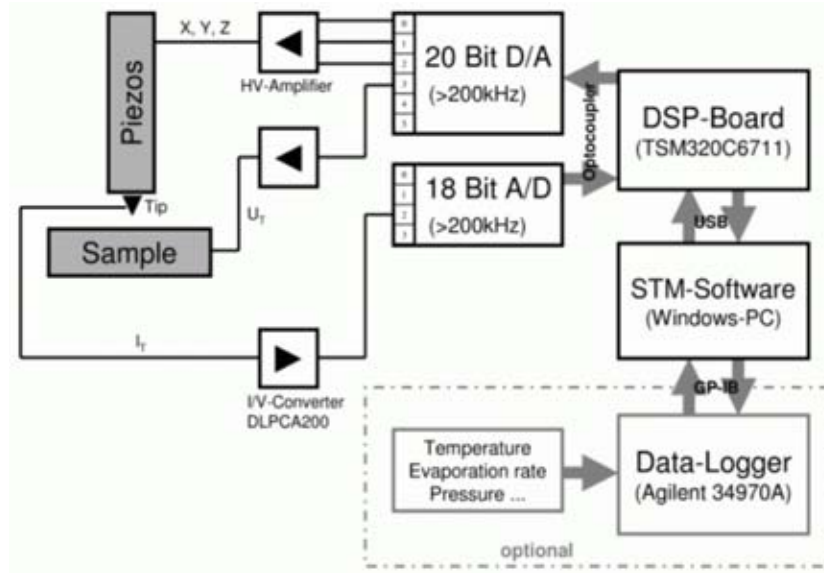
Figure 2.8: *Schematic of the electronics controlling the STM measurements. All signals are processed digitally and regulated via the software STMAFM 2.0. Taken from [60].*

impurities from deeper layers of the crystal as well as remaining Ar ions are brought to the surface and desorb. Repeated cycles of sputtering and annealing yield clean crystal surfaces.

Crystal surfaces

The single crystals employed in this work are cut in such a way that a certain plane of the fcc lattice is perpendicular to the surface normal, *i.e.* the atoms in the top layer are arranged in the respective crystal structure. The (111) surfaces exhibit a hexagonal structure and three dense-packed directions. In high resolution STM images these structures can be resolved. In fig. 2.9a,b STM images of the Cu(111) and Ag(111) surfaces are shown, respectively. Their lattice constants amount to $2.56\,\text{Å}$(Cu) and $2.89\,\text{Å}$(Ag). [61]
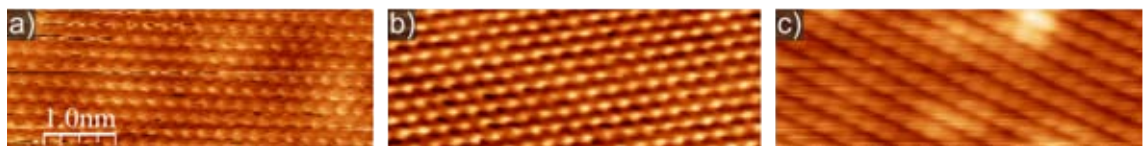
**Figure 2.9:** *STM images with atomic resolution of the three different crystals employed: a) Cu(111), b) Ag(111), c) Ag(100). [$5.5 \times 2.1\,\text{nm}^2$; a) -0.02 V, 3.7 nA; b) -0.96 V, 0.11 nA; c) -0.6 V, 0.13 nA]*

The (100) surface is four-fold symmetric with two-dense packed directions that are perpendicular to each other (fig. 2.9c). The lattice constant amounts to $2.89\,\text{Å}$ as well.

Sample holder

The crystal is fixed on an oven mounted on the sample holder (see fig. 2.10). A molybdenum (Mo) ring holds the crystal on the oven and a tantalum (Ta) wire (diameter 0.5 mm) coiled around the oven is connected to the Cu heating wires. The heating current required to heat the sample to 720 K is typically around 2.6 A. The temperature of the sample is measured by a K-type thermocouple which is attached to the Mo ring in close proximity of the crystal surface. All four cables, the two Cu wires required for heating and the two thermocouple wires are soldered to metal contacts on a ceramic plate at the back of the sample holder. If the sample holder is grabbed on the manipulator, metal springs are pressed against the metal contacts so that the sample can be heated and the temperature can be measured. If the sample is placed in the STM, it is contacted to establish the bias between tip and sample.
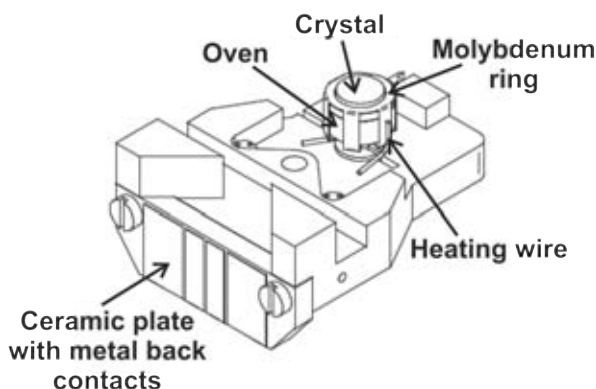
Figure 2.10: *Sample holder with a crystal mounted on the oven which can be heated with the Cu heating wires. Adapted from [69].*

Preparations

During the different sample preparations described in the following chapters the molecules are evaporated from the OMBE onto the cleaned crystal. Before depositing molecules for the first time under UHV conditions they need to be degassed in order to evaporate all remaining solvents or catalysts that are not desired on the surface. The degassing time and temperature depends on the molecule and its synthesis. For each experiment the temperature of the crucible T_{cru}, deposition time t_d, sample temperature T_S during deposition and the resulting coverage are given in table 1 (tab.) and in the respective chapter.

For the experiments addressing the interaction of porphyrins with gaseous ligands, small gas molecules (CO and O_2) are dosed via a leak valve by backfilling the whole chamber to pressures

Molecule	Substrate	T_{cru} (K)	T_S (K)	t_d (min)	Coverage (% ML)
2H-P	Ag(111)	470	350	30	0.2
2H-P	Ag(111)	510	300	30	1
2H-P	Ag(111)	510	530	90	0.59
2H-P	Ag(111)	510	570	90	0.45
2H-P	Ag(111)	510	610	90	0.34
2H-P	Ag(100)	520	300	3	0.44
2H-P	Ag(100)	500	640	30	0.76
Co-P	Ag(111)	540	300	5	0.17
Co-P	Ag(111)	530	300	30	0.62
Trans-Br-P	Ag(111)	520	180	5	sub-ML
Cis-Br-P	Ag(111)	520	250	5	sub-ML
2H-TPP	Ag(111)	600	300	4 to 7	sub-ML
DPP	Ag(111)	560	300	1	sub-ML
FePc	Cu(111)	680	300	30	sub-ML
BO-ADPM	Ag(111)	490	300	23	sub-ML
C_{60}	Ag(111)	690	320	50	sub-ML

Table 1: *Evaporation parameters for all molecules used in this work. Abbreviations: ML: monolayer, 2H-P: Free-base porphine, Co-P: Co-porphine, Trans-Br-P: 5,15 Dibromoporphine, Cis-Br-P: 5,10 Dibromoporphine, 2H-TPP: Tetraphenylporphyrin, DPP: 5,15 Diphenylporphyrin, FePc: Fe-Phthalocyanine, BO-ADPM: B,O-chelated azadipyrromethene.*

between $5 \cdot 10^{-8}$ to $3 \cdot 10^{-7}$ mbar. In most of the experiments the sample is kept inside the STM chamber. During gas dosage the shutter in front of the cryostat is opened and the sample warms up to approximately 20 K.

One layer of insulating boron nitride (BN) can be grown on the Cu(111) surface by chemical vapor deposition of borazine $(HBNH)_3$. The chamber is backfilled with borazine (p: $1 \cdot 10^{-7}$ mbar) for 5 min while the sample is held at approximately 1030 K and cooled down slowly after the gas dosage. A detailed description is given in refs. [70, 71].

After the respective preparation the sample is cooled on the manipulator by liquid helium with a cooling rate of approximately 1 K/s. When the sample reached a temperature of 100 K it is transferred to the STM chamber where it is further cooled to 6 K.

The molecules 2H-P and Co-P were purchased from Frontier Scientific, 2H-TPP and FePc from Sigma-Aldrich, DPP from PorphyChem and C_{60} from Alfa Aesar. The trans-Br-P and cis-Br-P were synthesized by Thien H. Ngo (National Institute for Materials Science, Japan). The synthesis of BO-ADPM is described in ref. [72].

2.2   Complementary methods

In the following, experimental techniques that were not applied by the author, but utilized by coworkers in order to gain a more comprehensive understanding, are briefly introduced. The combination of several surface-sensitive techniques allows a more profound characterization of the different systems than afforded by STM measurements only. The spectroscopic methods of near edge X-ray absorption fine structure spectroscopy (NEXAFS), X-ray photoelectron spectroscopy (XPS) and ultraviolet photoelectron spectroscopy (UPS) enable to probe a wide range of unoccupied and occupied states and to determine the elemental and chemical composition of adsorbates as well as their orientation relative to the underlying surface. Moreover, in temperature-programmed desorption (TPD) measurements the occurrence of chemical reactions on surfaces can be monitored, *e.g.* by recording the desorption of hydrogen or molecular fragments. Finally, density functional theory (DFT) gives the opportunity to model and interpret experimental results.

### 2.2.1   Near edge X-ray absorption fine structure spectroscopy

Near edge X-ray absorption fine structure spectroscopy (NEXAFS) is a spectroscopic method that probes electronic states of adsorbates on different surfaces. In molecules both electronic and geometric properties are determined by exciting inner shell electrons into unoccupied molecular orbitals with linearly polarized soft X-rays. This method is particularly suited for the characterization of atoms with a low atomic number Z, as *e.g.* C, O and N which are present in most organic compounds. [73,74]

In the NEXAFS technique, the X-ray absorption is recorded as a function of the photon energy at a certain absorption edge. Radiation with tunable energy, high brilliance and well-defined linear polarization are needed. Synchrotron radiation fulfills these requirements in an optimal way.

In general, the dominant processes in the energy range of soft X-rays are photoabsorption and -emission. If a core electron is excited in the irradiated material it leaves behind a core hole which is subsequently filled by an electron from a higher energy level. This second process either occurs radiatively by emission of a fluorescence photon or nonradiatively by emission of an Auger electron. [73] Both the emitted photons and electrons can be used to detect the excitation of a core electron at a particular energy of the X-rays, such that the absorption probability is monitored. In the following, only the detection of electrons is considered since they give a higher yield than fluorescence photons for low Z molecules.

For NEXAFS, the energy of the X-rays is chosen in such a way that core electrons are excited into unoccupied states of the adsorbates which are slightly below and above the ionization energy. Due to the low inelastic mean free path of electrons in matter, the electrons leaving the surface come from a depth of a few nanometers or less. Thus, this method is sensitive to sur-

faces and subtraction of the signal from the substrate allows a characterization of the adsorbates. NEXAFS measurements in the electron yield mode require UHV to minimize energy losses of the ejected electrons. Furthermore, in this environment unwanted contamination of the sample surface with molecules and atoms from the residual gases is significantly reduced.
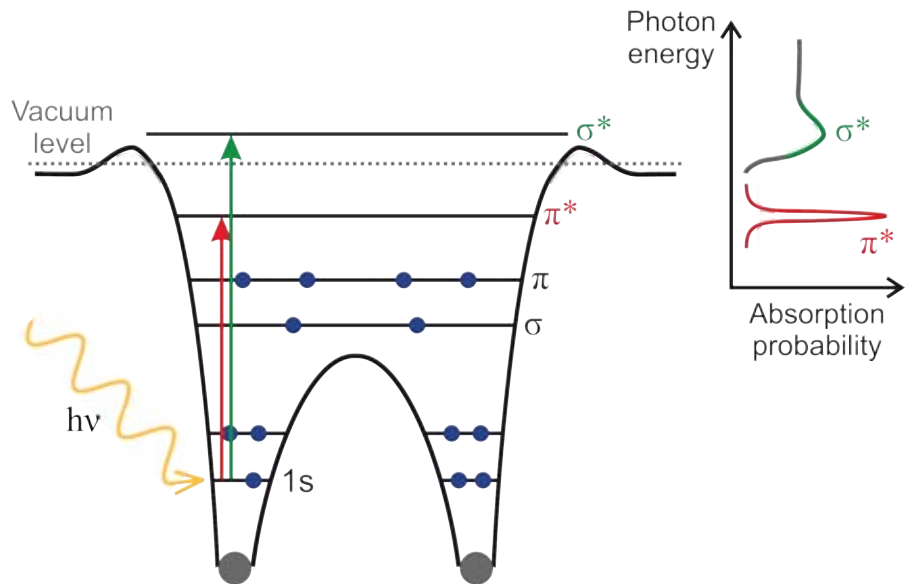
Figure 2.11: *Absorption signal for NEXAFS: Excitation of core electrons into the unoccupied molecular orbitals of a diatomic molecule induced by soft X-rays. $\pi^\star$ resonances usually lead to sharp peaks in the absorption spectrum, while $\sigma^\star$ states above the vacuum level exhibit a broader line shape.*

The excitation of a core electron of an adsorbed diatomic molecule is depicted in fig. 2.11. An electron in the 1s level of one of the atoms is excited into an unoccupied molecular orbital by absorption of a photon of given energy. The $\pi^\star$ states lie below the vacuum level. Thus, if the energy of the incoming photons matches the energy difference between the core level and the unoccupied $\pi^\star$ state, resonant excitation occurs and secondary electrons following core hole decay are detected resulting in a sharp peak in the absorption spectrum. As soon as the photon energy reaches the ionization threshold of a particular atomic core level an abrupt ionization step is observed in the absorption spectrum. Since $\sigma^\star$ states often lie above the vacuum level the respective resonances are superimposed with the ionization step. Moreover, they generally exhibit a broader line width than the $\pi^\star$ states. Recording the NEXAFS spectra across the K-edges of all atoms present in the adsorbate molecules enables to analyze the electronic structure of the molecules and the bonds between the atoms in the molecule, as the unoccupied molecular orbitals are bond-specific. [73–75]

Another notable feature of NEXAFS is the angle-resolved measurement of the absorption probability which can provide information about the geometric orientation of molecules or of specific functional groups. The absorption of linearly polarized X-rays is maximized if the vector of the

electric field of the electromagnetic radiation is parallel to the main axis of an orbital, whereas it is minimal if the electric field vector is perpendicular to the main axis of an orbital. Thus, by recording the absorption probability at different angles between normal and grazing incidence, the orientation of selected molecular orbitals relative to the surface can be determined.

The NEXAFS data presented here were recorded at the BESSY II storage ring (Berlin, Germany). The emitted electrons were retarded with a bias voltage of -150 V before detection in order to detect only electrons coming from the surface region (partial electron yield mode, PEY). For each of the three recorded incidence angles (20, 53 and 90°) the photocurrent signal of a contaminated gold grid traversed by the X-ray beam was recorded simultaneously with the PEY spectra. After the energy scale was referenced against a characteristic peak at 285 eV of the gold grid spectrum, the signal of a bare Ag(111) crystal was subtracted from the sample spectrum, followed by correction for the photon flux and normalization of the edge jump to one.

2.2.2   Photoelectron spectroscopy

With photoelectron spectroscopy (PES) the occupied states of adsorbates on surfaces are probed by irradiation with photons. This method gives element-specific information and is highly surface-sensitive. [8, 76]

If a material absorbs photons with a certain energy, bound electrons can be emitted and leave the material with a given kinetic energy. This phenomenon, known as the photoelectric effect, was first observed by H. Hertz in 1887. [77] Under the condition that the energy of the photons $\hbar\omega$ is large enough to overcome the work function ϕ of the material and the binding energy E_B of the respective electron, the kinetic energy of the emitted electron is given by:

$$E_{kin} = \hbar\omega - \phi - |E_B|\,.$$

The work function can be determined by the energy cut-off, where $E_{kin} = 0$. If ϕ is known, the binding energy of the emitted electrons can be calculated from their kinetic energy.

The photo emission spectrum, *i.e.* the intensity of emitted electrons plotted as a function of the kinetic energy, can be evaluated on the one hand qualitatively since the binding energies of core level peaks are element-specific. As a result, the composition of the first few layers of the sample can be determined. Similar to NEXAFS, the escape depth of the emitted electrons is of the order of 1 nm which renders PES surface-sensitive as well. Furthermore, a PES spectrum gives information about the relative amount of detected species by their different peak intensities.

Typically, one distinguishes between two variants of PES: X-ray photoelectron spectroscopy (XPS) employs X-rays (100 eV to 10 keV), while ultraviolet photoelectron spectroscopy (UPS) uses UV photons with energies between 5 and 100 eV.

For XPS experiments either a laboratory X-ray source is used or synchrotron radiation generated in a storage ring. In the latter case, a monochromator selects photons of well-defined energy before the beam impinges on the surface. The emitted electrons are detected by an electron

energy analyzer. Due to the short mean free path of the electrons all PES experiments are usually carried out in UHV. The analyzer selects electrons with a specific kinetic energy. Moreover, by applying a retarding voltage to the electron lens system at the entrance of the analyzer the kinetic energy can be scanned in a pre-determined interval, such that the $Intensity(E_{kin})$ spectrum is measured.

Because of the high energy of X-rays, XPS probes core levels of atoms. These levels are element-specific and they also vary moderately in energy depending on the chemical environment of the emitter atom. Thus, the chemical state of atoms in molecules can be determined.

In contrast, for UPS lower energy photons are provided either by a gas discharge lamp or by a synchrotron light source. With this method, the energy-dependent DOS of the valence band can be resolved with much higher resolution than for XPS. [76]

The UPS data shown in ch. 3.1.2 was recorded at the Materials Science beamline of the ELETTRA storage ring in Trieste, Italy. The UHV chamber is operated at a base pressure of $2 \cdot 10^{-10}$ mbar and is equipped with a SPECS PHOIBOS 150 electron energy analyzer of 150 mm mean radius fitted with a 1D-DLD detector. The light was linearly polarized with an energy of 30 eV and an energy resolution of 0.13 eV was employed. The electron detection geometry was varied between normal and grazing emission (60° off-normal, corresponding to normal incidence of the photon beam) with an acceptance angle of $\pm 7°$.

The XPS data presented in ch. 6.3 was recorded with a laboratory Al K_α X-ray source in grazing electron emission geometry. The UHV chamber exhibits a base pressure of $8 \cdot 10^{-11}$ mbar and is equipped with a hemispherical electron analyzer (Phoibos 100 CCD by SPECS).

2.2.3 Temperature-programmed desorption

During a temperature-programmed desorption (TPD) experiment the desorption of selected atoms or molecules is detected with a mass spectrometer while the sample is heated in a controlled way with a linear heating-ramp. This technique enables to determine the characteristic desorption temperature for atoms or molecules from a certain surface. In our specific case, by detecting the hydrogen (H_2) evolution, the occurrence of chemical reactions involving the release of hydrogen can be evidenced.

The TPD experiments presented here were carried out in a separate custom-built UHV system using a liquid nitrogen cooled quadrupole mass spectrometer with a Feulner cup [78] that can be brought within a few millimeters of the sample. The heating rate was controlled by a proportional-integral-derivative controller and kept constant within $< \pm 0.1$ K/s. The pressure during TPD measurements was between 2 to $8 \cdot 10^{-11}$ mbar and typically the background pressure of H_2 was on the detection limit of the mass spectrometer before TPD measurements begin.

2.2.4 Computational details

Most of the structural models shown in the following are obtained with the Software Hyper-Chem. [79] The geometry optimization was carried out either with the semiempirical AM1 and extended Hückel methods or molecular mechanics (MM+) simulations. Moreover, frontier orbitals are calculated using extended Hückel methods.

Several experimental findings of this work are corroborated and complemented by density functional theory (DFT) calculations. In ch. 3.1.2 the calculations of the electronic structure of porphines were performed using the software package StoBe, [80] which describes the Kohn-Sham orbitals by a linear combination of Gaussian type orbitals. The molecules are isolated (without surface) for all calculations and a revised Perdew, Burke and Ernzerhof (RPBE) exchange-correlation functional was used. [81, 82] These basis sets were used for the calculation of the shape of the frontier orbitals and their energetic separation.

The calculations discussed in ch. 4.1 were performed using the Gaussian Software package with the 6-311G basis in combination with Perdew-Burke-Ernzerhof (PBE) [81] exchange and correlation functionals. The different molecular structures were optimized towards the minimal ground state energy and the calculations were carried out in gas phase for an isolated molecule, using the default convergence criteria of the program.

3 Covalent coupling of porphines

Covalent nanostructures composed of functional molecules are of great importance for molecular electronics, optoelectronics and light-harvesting. [22, 25, 26, 83–85] They enable to overcome the limitation for minimal structure sizes and a precise control of the electronic properties of a device. The advantage of forming such structures artificially on well-defined surfaces is that these systems can be characterized with sub-molecular resolution in an UHV environment by local probe techniques. [86, 87]

Porphyrins on metal surfaces as well-studied systems [40, 88–91] are a promising candidate for the formation of covalent nanostructures on the one hand due to their versatile and tunable properties and on the other hand because covalently fused porphyrin tapes can already be synthesized in solution. [92–95] These tapes were shown to exhibit exceptional electronic features - a decreasing band gap with increasing tape length [93, 94, 96] - and nonlinear optical properties. [94, 97] Furthermore, calculations suggested that fused porphyrins can be employed as molecule-sized memory units [98] or for efficient excitation energy transfer. [85] Thus, it is desired to create these tapes on surfaces as well. As spray deposition techniques still exhibit practical limitations, [99, 100] the synthesis of covalent networks under UHV conditions on metal surfaces is aimed for and was realized for a range of different molecules [25, 26] and for porphyrins as well. [86, 101, 102]

In this chapter, the thermally-induced and surface-assisted covalent coupling of porphine molecules on Ag surfaces is described. The porphine molecule is the macrocycle of each porphyrin [103–105] and it can either host two hydrogen atoms in the center (free-base) or a metal ion which can be incorporated in the macrocycle on the surface by codeposition of a metal (similarly to tetraphenyl-porphyrins [89, 106–108]). It is shown, that triply- and doubly-fused porphine tapes can be formed on the Ag(111) and Ag(100) surfaces in a certain temperature range under the condition of a high coverage of molecules on the surface. Because of the extended conjugated π-systems of these oligomers the electronic properties are modified and similarly as in solutions a reduction of the band gap is observed. The same reaction can be induced for a metal porphine with a Co center, however the free-base and the Co-porphine exhibit different preferred binding motifs. Finally, a common method for the formation of ordered covalent nanostructures is the substitution of hydrogen atoms by halogen atoms at certain positions of the molecule so that a directed growth can be achieved. The halogen-C bond is dissociated at lower temperatures on metal surfaces than the C-H bond leading to a directed growth of nanostructures. [25, 26, 86, 102, 109, 110] This approach, referred to as Ullmann coupling, is employed for porphine molecules with two Br atoms as substituents. On the Ag(111) and Ag(100) surfaces the Br-porphines are observed to form metal-organic chains (via Ag coordination) and at higher substrate temperatures covalent structures.

3.1   Free-base porphine on Ag(111)

In ref. [104] it is shown that after room temperature (RT) deposition of free-base porphine (2H-P) onto a Ag(111) surface the molecules are arranged as dispersed monomers, if the coverage is below 0.8 monolayers (ML, definition of one ML is given in [104]). The molecules do not assemble in a regular pattern because of a repulsive interaction between them which is caused by a charge transfer from the substrate. [104]

Figure 3.1b shows 2H-P molecules on Ag(111) with a coverage of 0.2 ML ($T_{cru} = 470$ K, $T_S = 350$ K and $t_d = 30$ min, STM image acquired by Felix Bischoff). As depicted in fig. 3.1a, the two central hydrogen atoms impose a symmetry axis on the 2H-P molecule. This principal symmetry axis of the molecule (marked with dotted line) is always oriented perpendicular to one of the three dense-packed directions of the underlying substrate. The molecule appears square-like in STM images (see fig. 3.1a) with a depression in the center. The two protrusions on the macrocycle at the position of the pyrrolic nitrogen atoms (N-H) enable to identify the principal symmetry axis of the molecules in STM images as well as tautomers. [23, 104]
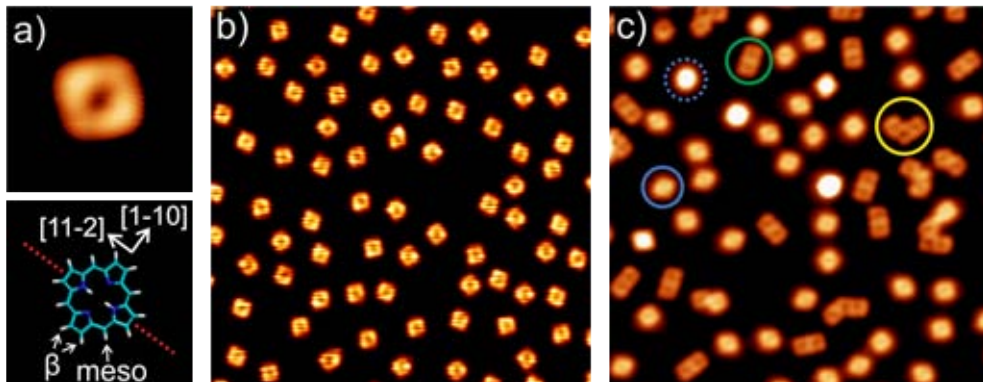

Figure 3.1: *2H-P on Ag(111). a) STM image of a monomer with structural model. The symmetry axis given by the central hydrogen atoms is perpendicular to the dense-packed direction [1-10] of the crystal. C, N, and H atoms are indicated in cyan, blue, and white, respectively. b) Room temperature deposition: Molecules are singly distributed over the surface. c) After annealing at 570 K: Monomers (blue circle), dimers (green circle) and a few oligomers (e.g. trimers, yellow circle) are observed. b) adapted from [104] and a,c) from [111]. [a] 2.5 × 2.5 nm², -0.15 V, 0.12 nA; b,c) 22.1 × 22.1 nm²; a) -0.2 V, 0.1 nA b) -0.8 V, 0.2 nA; c) -0.2 V, 0.1 nA]*

3.1.1   Homocoupling

In order to couple 2H-P molecules covalently, two different approaches are employed. In the first approach, slightly more than one ML of 2H-P is deposited onto a Ag(111) surface ($T_{cru} = 510$ K, $T_S = 300$ K and $t_d = 30$ min) and annealed at 570 K for 20 min. This preparation results in a sub-ML of monomers, dimers and a few oligomers (marked by circles in fig. 3.1c). The

most abundant oligomer is the dimer shown in fig. 3.2a. Its center-to-center distance amounts to 8.5 ± 0.3 Å which is significantly less than measured and calculated for organo-metallic coupling. In ref. [112] it is shown that Cu-P molecules couple via Cu adatoms on a Cu(110) surface with a center-to-center distance between two porphine units of 10.8 Å. On the other hand, geometry optimization, based on the semi-empirical AM1 method in the framework of the Hyper-Chem package, [79] gives a center-to-center distance of 8.5 Å for a covalently coupled dimer as shown in fig. 3.2a. The same number is obtained by geometry optimization carried out with the DFT code StoBe (see below). Thus, it is assumed that upon annealing dehydrogenation reactions take place at the periphery of the molecule and that the macrocycles couple covalently via C-C bonds.
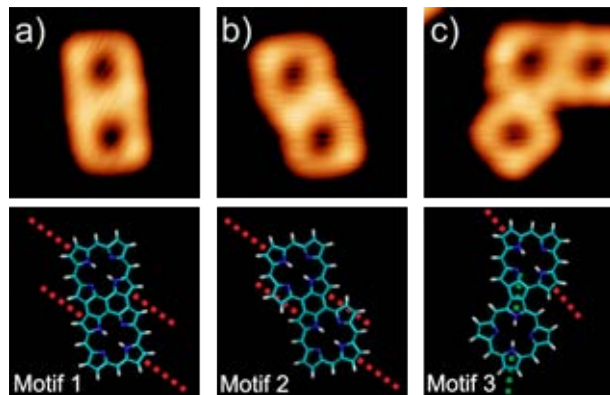

Figure 3.2: *Three different binding motifs for covalent coupling of 2H-P on Ag(111): STM topograph and tentative structural model. a) First motif: $\beta - \beta, meso - meso, \beta - \beta$. b) Second motif: $meso - \beta, \beta - meso$. c) Third motif: $\beta - \beta, meso - \beta$. Adapted from [111]. [$2.5 \times 2.5$ nm^2, -0.15 V, 0.12 nA]*

Overall, three different binding motifs are observed which are depicted with their respective tentative model in fig. 3.2. The structural models obtained with Hyper-Chem are assigned by comparison to the STM images. The first binding motif ($\beta - \beta, meso - meso, \beta - \beta$, named after the hydrogen positions marked in fig. 3.1a) involves six dehydrogenation reactions and the formation of three C-C bonds between the two porphine units (see fig. 3.2a), since the edges of the dimer are collinear. The second binding motif ($meso - \beta, \beta - meso$) is attributed to four dehydrogenation reactions and the formation of two C-C bonds (see fig. 3.2b) resulting in an offset of 2.2 ± 0.5 Å between the two porphine units. The two protrusions marking the symmetry axis of the molecules are still visible in the oligomers, thus the orientation of the porphine units in the oligomers towards the substrate can be determined. Within the precision of the measurement ($\pm 5°$), for motif 1 and 2 both units are oriented along the dense-packed directions of the crystal (marked in fig. 3.5a) in the same way as the monomers.

Finally, the third binding motif ($\beta - \beta, meso - \beta$) is assumed to involve four dehydrogenation reactions and the formation of two C-C bonds (see fig. 3.2c). The formation of only a single

C-C bond in this motif is excluded because of disagreement of the images with models involving a single bond. In contrast to the first two binding motifs, only one of the porphine units in the third binding motif is oriented along the dense-packed directions of the crystal. The second unit deviates by approximately 15° from these crystal directions, resulting in an angle of 45° between the two units. Similarly, the gas phase geometry optimization of the third binding motif by Hyper-Chem yields an angle of 45° between the two porphine units. Consequently, the covalent interaction between the molecules is stronger than the site-specific molecule-substrate interactions since one of the porphine units deviates from its preferred adsorption site. The fact that the same covalent coupling reactions are observed on a surface with a different geometry, namely the Ag(100) surface, supports the conclusion that the substrate does not enforce the particular conformations of the oligomers (see also ch. 3.2).

Additionally, species of the size of a monomer and a greater apparent height are observed after annealing (marked with blue dotted circle in fig. 3.1a and shown in fig. 3.3). Their appearance is cross-like at negative biases (fig. 3.3a) and rhombic at positive sample biases (fig. 3.3b). The dI/dV spectrum of the brighter species shows a clear peak around -0.1 V whereas the spectra acquired on 2H-P molecules are nearly featureless (see fig. 3.4). In good agreement with the dI/dV spectra, the dI/dV maps show pronounced differences between the bright species and a 2H-P monomer. At -0.1 V the bright species exhibits a cross-shaped state whereas the monomer appears dim (fig. 3.3c,d). In comparison, fig. 3.3f shows a difference in the electronic structure between the two monomers at a different bias as well.
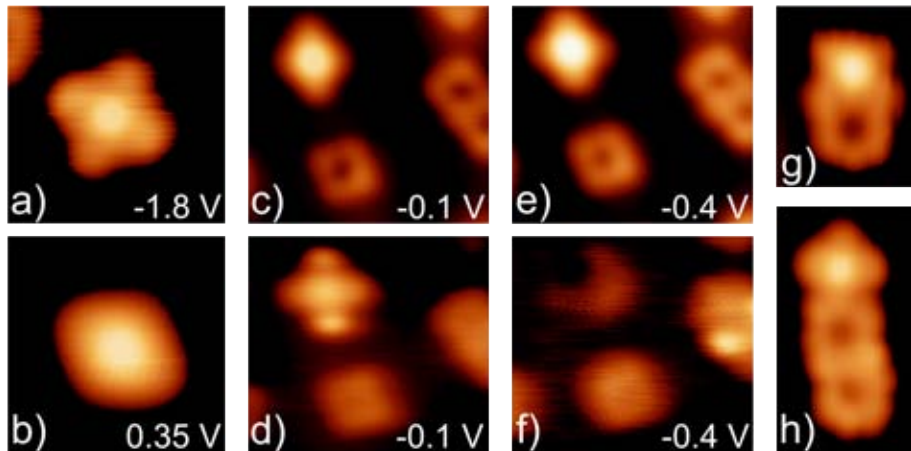
Figure 3.3: *Bright monomer species assigned to 2H-P interacting with one Ag atom. a) Cross-shaped appearance at negative bias and b) square-shaped appearance at positive bias. c) Topography image and d) dI/dV map showing a pronounced state on the bright monomer species and less density of states for the monomer and dimer. e) Topography image and f) dI/dV map indicating clear differences between the three species at another bias. g) Dimer and h) trimer interacting with Ag atoms. [a,b) 2.5 × 2.5 nm², c-f) 4.5 × 4.1 nm², g) 2.7 × 2.1 nm², h) 3.7 × 2.1 nm², a) -1.8 V, 0.09 nA, b) 0.35 V, 0.2 nA, c,d) -0.1 V, 0.2 nA, e,f) -0.4 V, 0.2 nA, g,h) -1.4 V, 0.09 nA]*

Due to the similarity in the topographic appearance to other metalated porphines such as Co-P

(see ch. 3.3) the brighter species are assigned to 2H-P molecules that reacted with a Ag atom. Since these species exhibit a range of different apparent heights there might be different configurations of the Ag atom in the center of the macrocycle. As shown in fig. 3.3h,i not only monomers can incorporate a Ag atom into the macrocycle but also oligomers.
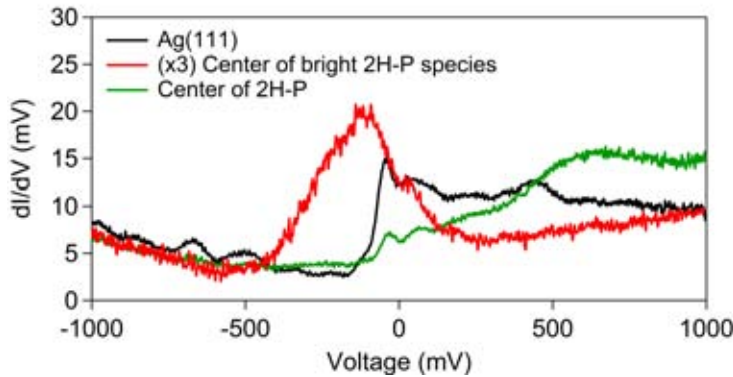
Figure 3.4: *Scanning tunneling spectra (dI/dV ∝ DOS) on the bare metal (black line), on the center of a 2H-P monomer (green line) and on the center of a bright monomer (red line). In agreement with the dI/dV map at -0.1 V in fig. 3.3d a peak is present around this bias for the bright 2H-P species but not for the 2H-P.*

Employing this first approach to covalently couple porphine molecules $49 \pm 2\%$ of all molecules reacted to form oligomers. The average oligomer length is 2.1 ± 0.3 porphine units and the oligomer coverage is 0.11 ± 0.02 ML of 2H-P. The efficiency of the reaction could not be improved considerably by a prolongation of the annealing time because the reaction on the surface is limited by desorption of the molecules. At 530 K the desorption rate for monomers amounts to 3% ML/min. Thus, the amount of reactants on the surface is limited by desorption.

Therefore, in the second approach a continuous supply of molecules onto the heated surface is applied that counteracts the desorption. Three different substrate temperatures during deposition are employed (530, 570 and 610 K) and the deposition time is 90 min for all cases. As depicted in fig. 3.5a,b this procedure results in a sub-ML of monomers and oligomers although T_S is lower than in the first approach. For the same temperature as employed in the first approach the percentage of molecules bound in oligomers is clearly increased from 49% to 80% (fig. 3.5c,d). A further increase of T_S to 610 K during deposition of molecules leads to an average oligomer length of 8.2 porphine units and 97% of the molecules are nonmonomers (fig. 3.5e,f). However, the surface coverage of oligomers stays approximately constant for the three different temperatures of the second approach (see tab. 2 for details). Thus, the second approach enables to increase the average oligomer length and the percentage of molecules bound in oligomers. Furthermore, a higher coverage of oligomers is achieved. Table 2 summarizes the statistical analysis.
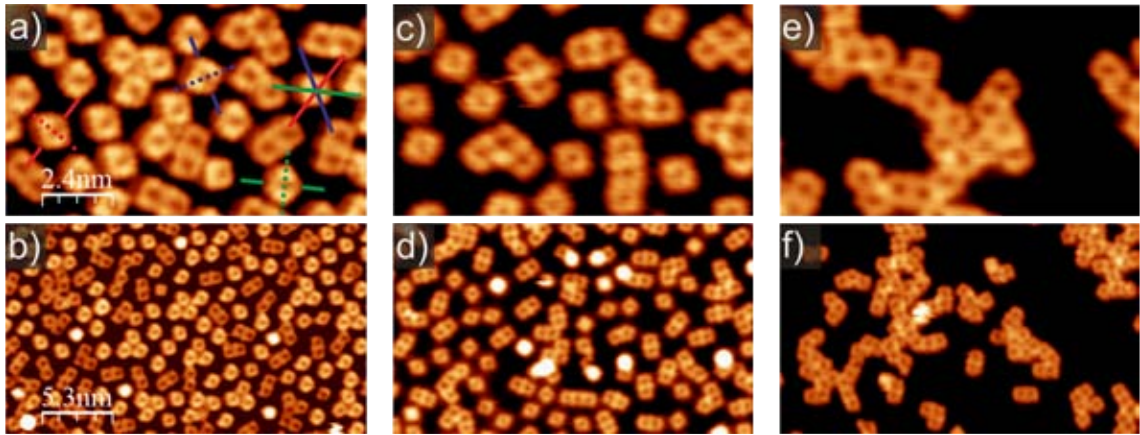
Figure 3.5: *Deposition of 2H-P on heated substrate (Ag(111)) at three different substrate temperatures T_S: a,b) $T_S = 530\,K$; c,d) $T_S = 570\,K$; e,f) $T_S = 610\,K$. The percentage of reacted molecules and the average length of oligomers increases with increasing T_S. The solid lines give the dense-packed directions of the crystal. Adapted from [111]. [a,c,e) $12.6 \times 7.3\,nm^2$; b,d,f) $28.1 \times 16.4\,nm^2$; a) -0.5 V, 0.3 nA; b) 1.21 V, 0.3 nA; c,d) -1.8 V, 0.07 nA; e) -1 V, 0.09 nA; f) -0.7 V, 0.1 nA]*

| Substrate temperature T_S	530 K	570 K	610 K
Average oligomer length	2.1 ± 0.3	2.7 ± 1.3	8.2 ± 10.8
Coverage	59 ± 4	45 ± 4	34 ± 4
Monomer coverage	29 ± 4	9 ± 2	1 ± 0.5
Oligomer coverage	30 ± 4	35 ± 3	33 ± 3
Percentage of nonmonomers	51 ± 2	80 ± 3	97 ± 3
Binding motif 1	81 ± 5	74 ± 5	67 ± 6
Binding motif 2	13 ± 3	12 ± 3	14 ± 5
Binding motif 3	6 ± 3	14 ± 3	20 ± 5

Table 2: *Statistical analysis of average oligomer length, coverages, percentage of nonmonomers and occurrence of the three binding motifs in dependence of the substrate temperature during deposition. Coverages are given in % of one ML of 2H-P on Ag(111) which is defined in [104]. Errors correspond to standard deviation.*

As well as for the first approach three different binding motifs are observed in the oligomers obtained by the second approach. The first binding motif is clearly abundant at all three substrate temperatures, however, it slightly decreases with increasing temperature from 81 % to 67 % (see tab. 2). The second motif stays constant within the error bars and the occurrence of the third motif increases with temperature from 6 % to 20 %. This behavior seems counterintuitive on first sight since the first motif involves six dehydrogenation reactions and the other two motifs only four. Furthermore, no singly-fused oligomers were observed. At first, an adsorption-site determined reaction can be excluded because within the precision of the modeling none of the binding motifs is commensurate with the lattice of the crystal. Another explanation for the preferred occurrence of motif 1 can be found in the wet chemistry approach for synthesizing porphyrin tapes. As an intermediate *meso – meso* linked porphyrins are synthesized due to the *meso*

position being more reactive than the β positions. [92, 113] If this property is preserved on the Ag surface the reactivity of the *meso* position can be an explanation of the preferred occurrence of motif 1. Once the *meso* positions reacted to form a C-C bond between two molecules the steric hindrance of the remaining hydrogen atoms at the β positions results in strain-facilitated dehydrogenations and the formation of the other two C-C bonds yielding motif 1. The partial lifting of the molecule or rotation around the *meso* C-C bond seems feasible at these substrate temperatures where considerable amounts of molecules desorb. In accordance with this explanation is the increasing occurrence of motif 3 with temperature since more energy is available for dehydrogenation at the less reactive positions.

Generally, eliminative on-surface reactions involve diffusion of the reactants, dehydrogenation or dehalogenation and covalent coupling. The dehydrogenation or dehalogenation can occur upon adsorption followed by the diffusion of the radicals which covalently couple when they come close enough. [26, 28, 86, 102] Another possibility involves the diffusion of the unreacted educts and only when two educts are close to each other dehydrogenation and covalent bond formation take place. [114, 115] In the case of 2H-P on Ag(111) it is observed that firstly, the surface is decisive for the reaction. The energy required to cleave the C-H bond in vacuum amounts to 4.5 eV [116] which is significantly more than the thermal energy available during the reactions on the surface, thus the surface acts as a catalyst for the reaction. Furthermore, no oligomers are observed if the surface temperature is below 470 K, thus the reaction does not take place in the crucible. Secondly, the coverage of molecules on the surface during the reaction is decisive for the efficiency of the reaction. In the first approach the coverage decreases with time which limits the amount of available educts. The second approach provides a high coverage of molecules over the entire reaction time. It was also observed for another on-surface reaction that the coverage plays an important role. [117] However, in the first approach the coverage is high at the beginning of the annealing time. Nevertheless the first approach is less efficient. With these findings it cannot be stated how the on-surface reaction takes place. If all molecules dehydrogenated already upon adsorption, only radicals should be present after annealing. However, as depicted in fig. 3.6 it is not possible to distinguish between porphine radicals and unreacted porphines in STM images. Figure 3.6c,d show that the appearance in STM of a thermally debrominated 5,15 Dibromoporphine is very similar to a RT deposited 2H-P (fig. 3.6a) as well as to 2H-P deposited onto a heated sample (fig. 3.6b).

The objective to form extended oligomers is achieved by employing the second approach. As shown in fig. 3.5f oligomers consisting of up to 90 porphine units are observed. Nevertheless, the covalent nanostructures lack order. Figure 3.7a,b depicts the most abundant trimers, c and d appear less frequently. Even though the triply-fused dimer is formed preferentially most of the longer oligomers do not exhibit the straight shape of porphyrin tapes but involve many turns and angles. Thus, a more directed growth of oligomers is required in order to form extended and regular nanostructures. One method to achieve directed growth is to substitute some hydrogen
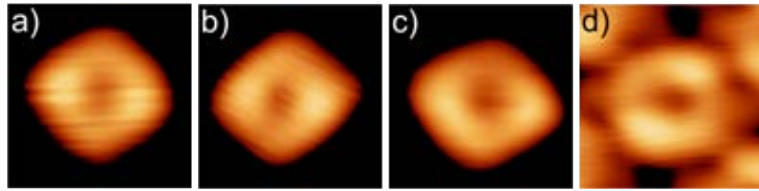
Figure 3.6: *a) 2H-P on Ag(111) after RT deposition (adapted from [104]) and b) after deposition onto a heated sample. There is no clear difference in appearance to thermally debrominated 5,15 di-bromoporphine (c,d). Adapted from [111]. [1.6 × 1.6 nm²; a) -0.8 V, 0.2 nA, b) -0.7 V, 0.1 nA, c) -0.8 V, 0.08 nA, d) -0.1 V, 0.1 nA]*

atoms at the periphery of the molecule with halogen atoms which are more reactive. A wide range of examples can be found in literature [26, 86, 102, 109] and one example involving the porphine is shown in ch. 3.4.
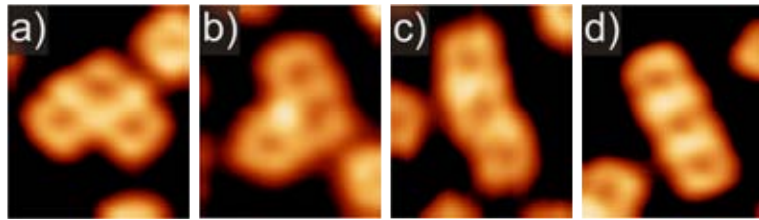
Figure 3.7: *Different trimers observed for the second approach. a,b) Most abundant motifs. c,d) Less frequently observed motifs. Adapted from [111]. [3.8 × 3.2 nm²; -1.8 V, 0.07 nA]*

3.1.2   Electronic structure and physical properties

In order to further characterize the porphine oligomers, space-averaging techniques were employed. Katharina Diller carried out the NEXAFS measurements and simulations and the DFT calculations. Francesco Allegretti supervised the UPS measurements.

Figure 3.8c shows the NEXAFS spectrum recorded on a sub-ML of porphine monomers on Ag(111). Its similarity to the spectrum of a multilayer points to a weak modification of the spectrum by the charge transfer from the substrate to the molecules in the first layer. [104] Consequently, the calculated magic angle curve (fig. 3.8g) agrees well with the measured one (fig. 3.8e). For a sample prepared via the second approach at $T_S = 610$ K, *i.e.* nearly all molecules are bound in oligomers, the NEXAFS spectrum shows pronounced differences (see fig. 3.8d). The first peak is quenched while the angular dependence is similar. These changes have often been attributed to a partial filling of the LUMO from the substrate. [105, 118] On the other hand, the DFT calculation of the NEXAFS spectrum of the triply-fused dimer (fig. 3.8h) is very similar to the experimental one (fig. 3.8f) although the calculations do not involve any substrate. Therefore, the NEXAFS spectra point towards a chemical change of the oligomers in

comparison to the monomers rather than a modified interaction with the substrate. However, it should be emphasized that in the experiment oligomers of different length and with different binding motifs are present on the surface whereas the calculations only involve a single triply-fused dimer.

The vanishing π^* resonance in the 90° curve for both the monomer and the oligomer sample imply a flat adsorption of the molecules for both cases.
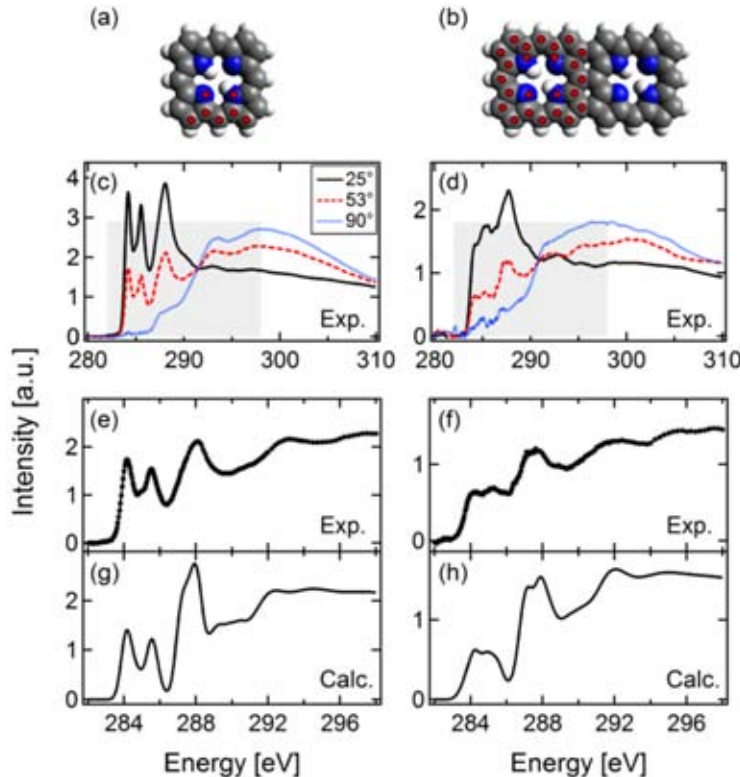
Figure 3.8: *Experimental and simulated C K-edge NEXAFS spectra of 2H-P monomers (RT deposition) on the left and oligomers (deposition at $T_S = 610 \, K$) on the right. Red dots in the structural models of the 2H-P monomer (a) and dimer (b) mark the inequivalent C and N atoms which were taken into account for the calculations. c,d) Angle-resolved spectra with gray areas indicating the zoomed-in region shown in e and f. g,h) Simulated spectra in the same energy range as e,f. Taken from [111].*

The electronic states of the triply-fused dimer as the most abundant coupling motif are probed by STS and UPS. Similarly to the monomer the $\mathrm{d}I/\mathrm{d}V$ curves show no pronounced states for dimers either. In contrast, $\mathrm{d}I/\mathrm{d}V$ maps show a clear difference between monomers and dimers. Figures 3.9 and 3.10a to d show the topography and the $\mathrm{d}I/\mathrm{d}V$ signal at different negative biases, which means that the occupied states of the molecules are probed. At -0.45 V the dimers exhibit a pronounced state in the center whereas the monomers appear darker. The state of the dimer appears in a broad range of biases from -0.55 to -0.25 V. A possible explanation why this peak is not observed in $\mathrm{d}I/\mathrm{d}V$ curves is that the peak is too broad due to interaction with the

substrate.
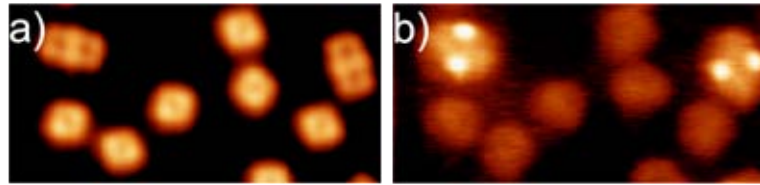
Figure 3.9: *a) STM topography image and b) simultaneously recorded dI/dV map at -0.45 V. A two-lobed state is present on the center of the two dimers whereas the monomers exhibit less contrast at this bias. Adapted from [111]. [11 × 5.3 nm^2; 0.21 nA]*

The occupied states are also probed by UPS on a sample which is prepared at $T_S = 570$ K resulting in 80 % of the molecules bound in oligomers. In comparison to the monomer sample (green line in fig. 3.11) the oligomer sample (blue line) shows additional peaks in the UP spectrum. For the monomers a clear HOMO state is observed at 2.2 eV and the LUMO is shifted partially below the Fermi level because of a charge transfer from the substrate indicated by a small peak close to the Fermi level. [104] The LUMO is shifted even further below the Fermi level for the oligomers as marked by the blue bar and the HOMO is shifted closer to the Fermi level to 1.5 eV which results in a reduced band gap for the oligomers. The HOMO peak of the monomers is visible as well in the oligomer spectrum since 20 % of the molecules are still monomers.
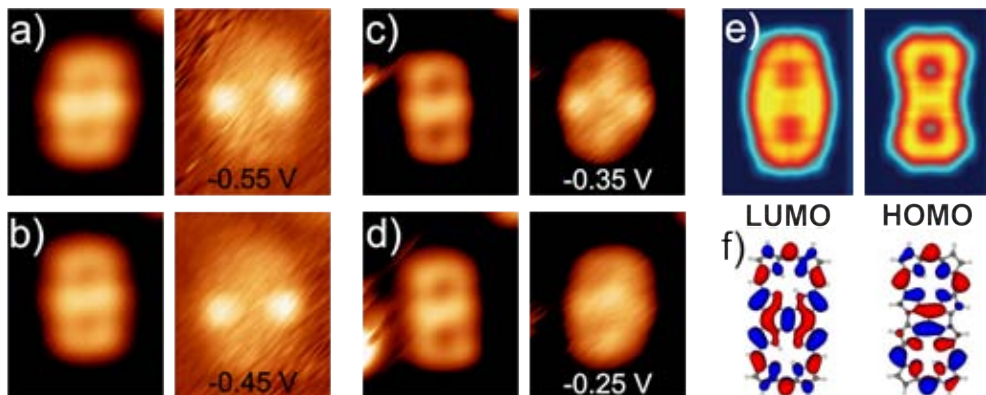
Figure 3.10: *Electronic states of the triply-fused dimer. a) to d) STM topography images and dI/dV maps at different biases. a) -0.55 V, b) -0.45 V, c) -0.35 V, d) -0.25 V. e) STM images of the HOMO and the LUMO obtained by Hückel calculations. f) Kohn-Sham frontier orbitals (HOMO and LUMO) calculated using the software package StoBe. The shape of the state observed in the dI/dV maps resembles the calculated LUMO. Adapted from [111]. [2.7 × 3.3 nm^2; 0.2 nA]*

Figure 3.11b shows DFT calculations of the ground states of the porphine monomer and dimer. Usually the actual gap values are not reproduced by DFT [119] but the same trend of a reduction in the band gap is observed. This finding is in good agreement with the observation of a

decreasing band gap for an increasing tape length in solution. [120–123]
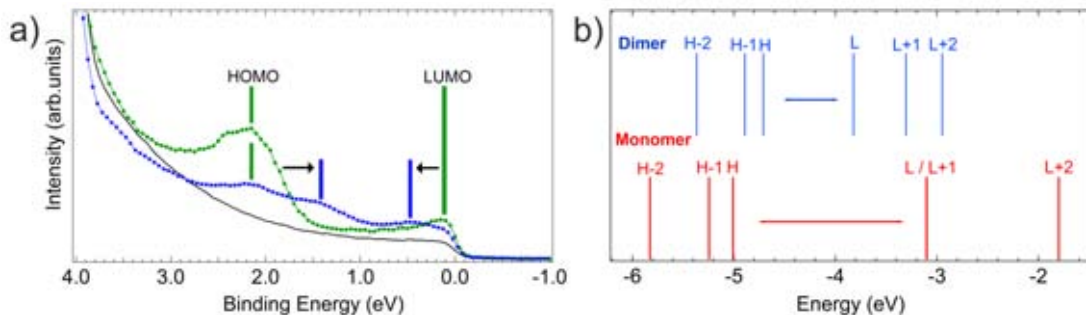
Figure 3.11: *Band gap reduction upon dimerization. a) UP spectra recorded in grazing emission geometry for a monomer sample (green curve) and a oligomer sample (blue curve, $T_S = 570\,K$). The black line corresponds to a spectrum on the clean Ag(111) surface. b) DFT ground state calculation of the Kohn-Sham energies for the triply-fused dimer (blue) and monomer (red). The dimerization leads to a splitting of the degenerate LUMO (L) and LUMO+1 (L+1) orbitals of the monomer. Adapted from [111].*

Furthermore, the shift of the LUMO below the Fermi level can be rationalized by the appearance in STM images. In fig. 3.10e charge density contour plots representing the LUMO and the HOMO of the triply-fused dimer are shown which are obtained by extended Hückel calculations. [124] The waist of the molecule is broadened for the LUMO and narrow for the HOMO. Similarly, the calculated Kohn-Sham frontier orbitals (software package StoBe) exhibit the same shape for both orbitals (fig. 3.10f). Since the state observed in the dI/dV maps is clearly visible on the waist of the dimer, it resembles the calculated shape of the LUMO rather than the HOMO despite being in the occupied domain. Consequently, the shape of the state on the dimer points to a partial filling of the LUMO as well.

## 3.2   Free-base porphine on Ag(100)

In order to test the influence of the substrate geometry on the coupling reaction of 2H-P on Ag, the molecule is deposited onto a Ag(100) surface which has two dense-packed directions and is four-fold symmetric (see ch. 2.1.5). Room temperature deposition ($T_{cru} = 520\,K$, $t_d = 3\,min$) of 0.44 ML of 2H-P results in singly distributed molecules (see fig. 3.12). Due to the alignment with the substrate the molecules show two different orientations that form an angle of 90°.

Several annealing steps are carried out revealing that the desorption rate is significantly smaller on the Ag(100) surface in comparison to Ag(111). At 600 K it amounts to 0.8 % of a ML/min. Furthermore, higher temperatures are required to reach the same percentage of nonmonomers as on Ag(111). The interaction with the substrate is stronger leading to a reduced desorption
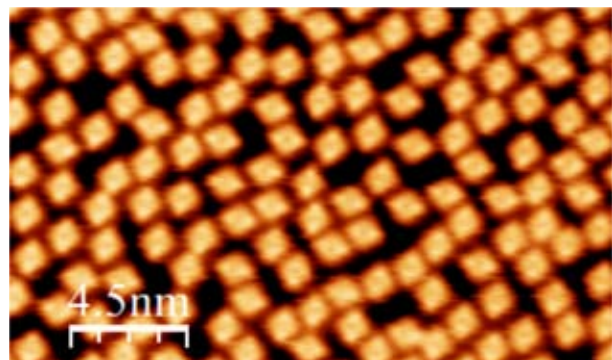
Figure 3.12: *Room temperature deposition of 2H-P onto Ag(100). The molecules are dispersed and show two different orientations due to the two-fold symmetry of the substrate. [24.1 × 14.3 nm^2; -0.5 V, 0.2 nA]*

rate, therefore mainly the first approach is employed, *i.e.* a ML sample is annealed after the deposition of molecules. Varying the annealing temperature and duration shows that the percentage of nonmonomers increases with both temperature and time, at least as long as there are still monomers present on the surface. Moreover, the amount of porphines interacting with a Ag atom (see fig. 3.3) increases with time and temperature as well.
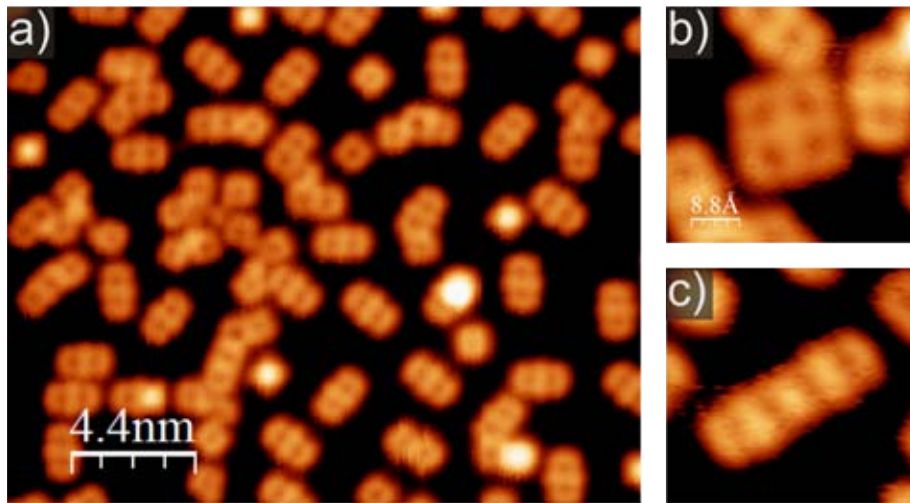
Figure 3.13: *a) 2H-P on Ag(100) after annealing at 620 K for 40 min. Different oligomers and a few monomers are observed. b,c) Two oligomers that are only observed for annealing temperatures above 590 K (on both Ag(100) and Ag(111)). [a) 23.7 × 18.6 nm^2; b,c) 4.8 × 4.5 nm^2; a,b) -0.6 V, 0.14 nA; c) -0.5 V, 0.1 nA]*

Figure 3.13 shows the surface after annealing at 620 K for 40 min with monomers and oligomers which are mainly dimers. With increasing annealing temperature oligomers with a high symmetry are observed as *e.g.* depicted in fig. 3.13b and c. However, they represent a minority of the formed oligomers and are observed on the Ag(111) surface as well.

The annealing step on Ag(100) (620 K for 40 min) yields a composition of molecules which shows

similarities to 2H-P deposited onto the Ag(111) surface heated to 570 K during deposition for 90 min. Despite these different preparation procedures both samples yield a similar percentage of nonmonomers, 86 % on Ag(100) and 80 % on Ag(111), a similar average oligomer length, 2.6 on Ag(100) and 2.7 on Ag(111), and roughly similar total coverages, 0.35 ML on Ag(100) and 0.45 ML on Ag(111) (see also tab. 3). Given the fact that increasing the annealing time only leads to a moderate increase in the percentage of molecules bound in oligomers, the above comparison indicates that a higher temperature is required on the Ag(100) surface than on the Ag(111) surface in order to achieve the same efficiency of covalent coupling.

Furthermore, the occurrence of the three binding motifs is compared for both surfaces (see tab. 3). The first binding motif is slightly more abundant on Ag(100) and motif 2 occurs significantly less often on Ag(100) than on Ag(111). The different adsorption sites on both surfaces might play a role for the different occurrence of the binding motifs.

	2H-P on Ag(100) annealing at 620 K	2H-P on Ag(111) $T_S = 570$ K during deposition
Average oligomer length	2.6 ± 1.04	2.7 ± 1.3
Coverage	35 ± 3	45 ± 4
Percentage of nonmonomers	86 ± 5	80 ± 3
Binding motif 1	80 ± 6	74 ± 5
Binding motif 2	4 ± 2	12 ± 3
Binding motif 3	16 ± 3	14 ± 3

Table 3: *Statistical analysis of average oligomer length, coverage, percentage of nonmonomers and occurrence of the three binding motifs for 2H-P on Ag(100) after annealing at 620 K and deposition of 2H-P onto Ag(111) held at 570 K (see ch. 3.1.1). Coverages are given in % of one ML of 2H-P on Ag(111) which is defined in [104]. Errors correspond to standard deviation.*

In order to increase the percentage of molecules bound in oligomers, porphines are deposited onto the Ag(100) surface heated to 640 K for 30 min. This procedure yields no increase of nonmonomers in comparison to annealing at 620 K for 40 min, however longer oligomers are observed (see fig. 3.14).

Due to bad resolution during all measurements on this sample no statistical analysis of the binding motifs is carried out. Moreover, some porphines decompose at this temperature (fig. 3.14b) and also at an annealing temperature of 600 K (fig. 3.14c) and 620 K (fig. 3.14d).

In summary, the covalent coupling reactions take place on the Ag(100) surface as well, however the desorption rate is significantly smaller and higher annealing temperatures are required. Therefore, on Ag(111) longer oligomers are formed before the molecules start to decompose at high temperatures.
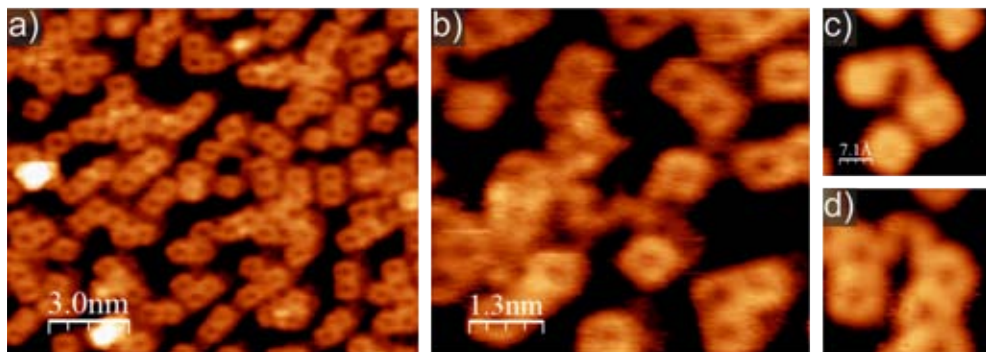
Figure 3.14: *Deposition of 2H-P onto Ag(100) at 640 K. a) Overview STM image: Longer oligomers than at lower temperatures are observed. b) Some 2H-P are partially decomposed (in the center of the image). Decomposition is also observed at lower annealing temperatures: c) at 600 and d) at 620 K. [a) $16.3 \times 13.8\,nm^2$; b) $6.8 \times 6.3\,nm^2$; c,d) $3.8 \times 3.8\,nm^2$; a,b) -0.7 V, 0.1 nA, c) -0.5 V, 0.2 nA, d) -0.6 V, 0.11 nA]*

3.3   Co-porphine on Ag(111)

The incorporation of a metal ion in the center of the porphine molecule changes many properties such as the interaction with the substrate, the electronic structure or the shape of the orbitals. In the following, the covalent coupling of a metal-porphine, namely Co-porphine (Co-P), is studied.
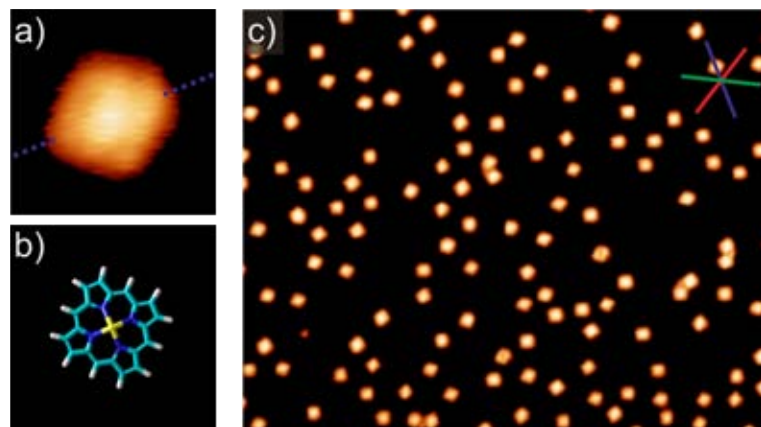
Figure 3.15: *Co-porphine deposited onto Ag(111) at RT. a) STM image of a single molecule with b) structural model. The Co atom is indicated in yellow and the main molecular axis in blue. The center of the molecule appears as a protrusion at all biases. c) Overview STM image of a sub-ML coverage (0.17 ML). The molecules are dispersed over the whole surface. [a) $1.6 \times 1.6\,nm^2$, 0.13 nA; c) $33.5 \times 26.9\,nm^2$, 0.13 nA. The sample bias is unknown due to a missing grounding during these measurements.]*

For the Co-P a higher evaporation temperature than for the 2H-P is required due to the higher molecular weight. At first, Co-P is deposited onto the Ag(111) surface held at RT ($T_{cru} = 540\,K$, $t_d = 5\,min$). This preparation procedure results in a sub-ML (0.17 ML) of dispersed molecules,

very similar to the case of 2H-P (see fig. 3.15).

The Co-P appears with a protrusion in the center caused by the Co ion. The high resolution STM image (fig. 3.15a) reveals that the molecule does not appear four-fold symmetric but one of the molecular axes shows a greater apparent height than the other one (main molecular axis marked with blue dotted line in fig. 3.15a). This behavior is observed for Cu-P [105] and for a range of other molecules as well, *e.g.* metal phthalocyanines (see [125, 126] and ch. 5) and is attributed to an electronic effect due to different interactions with the substrate for the two molecular axes. All Co-P are oriented along the dense-packed directions of the crystal with the main axis perpendicular to the dense-packed directions.

3.3.1 Covalent coupling

Aiming for the formation of covalent bonds between the Co-P molecules a sample with a higher coverage (0.62 ML, $T_{cru} = 530$ K, T_S = RT and $t_d = 30$ min) is annealed at 570 K for 20 min in a first step. After subsequent cooling to 6 K the molecules are arranged in different domains consisting of rows of molecules (see fig. 3.16). The rows within the domains are oriented in three different directions pointing to an alignment with the crystal. It is not clear what the driving force for this arrangement is. The average intermolecular distances amount to 14.5 ± 0.5 Å within the rows and 16.5 ± 0.5 Å between the rows which is too large for any coupling between the molecules and also their appearance is not changed in comparison to RT deposition. Since 2H-P molecules show a coverage-dependent arrangement on the Ag(111) surface, [104] the higher coverage in comparison to the first RT deposition (see fig. 3.15c) could be an explanation for the arrangement of the Co-P.
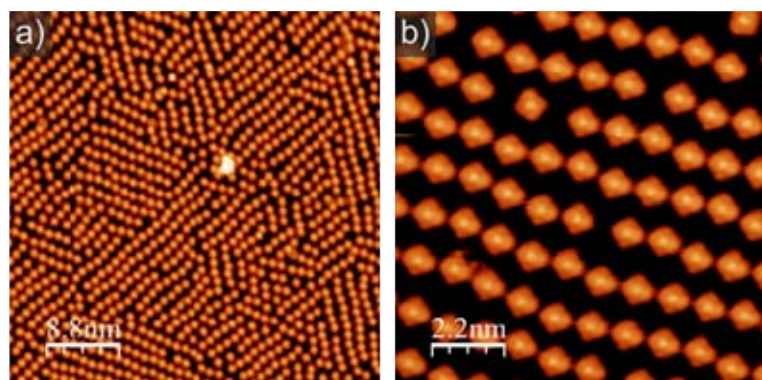
Figure 3.16: *STM images of 0.62 ML Co-P on Ag(111) after annealing at 570 K for 20 min. Three different domains with rows of molecules oriented in the same direction are present. The driving force for this arrangement is not understood. [a) 47.6 × 47.6 nm^2, 0.1 nA; b) 11.9 × 11.9 nm^2, 0.2 nA. The sample bias is unknown due to a missing grounding during these measurements.]*

Coupling between Co-P molecules is observed for annealing temperatures between 600 and

630 K. In order to determine the nature of the bond and the binding motifs structural models of covalently coupled Co-P oligomers are superimposed with the STM images (see fig. 3.17) since the binding motifs cannot be clearly distinguished in the images. Due to the good agreement of the models with the STM image a coupling via Ag atoms can be excluded and the formation of covalent C-C bonds is assumed.
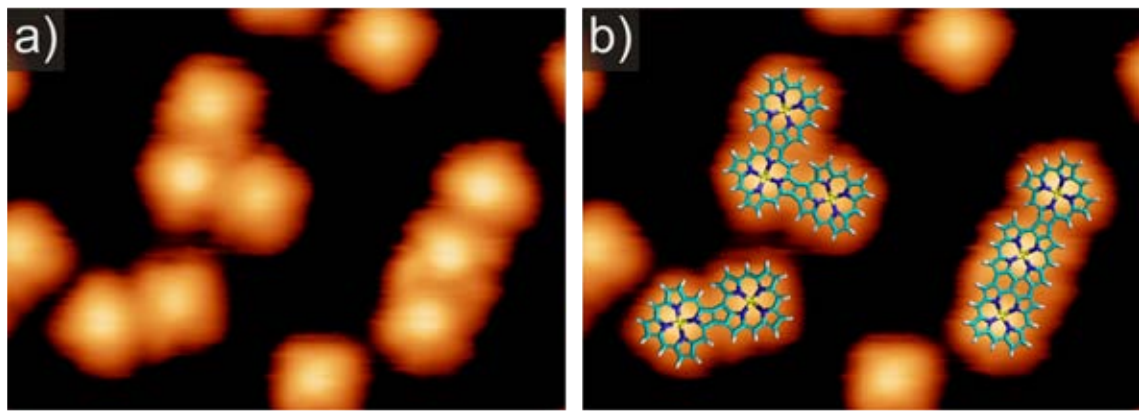
Figure 3.17: *STM image of one Co-P dimer and two trimers: a) without and b) with structural models of the dimer and respective trimers overlaid. Due to the good agreement of the STM image with the structural models of covalently coupled oligomers a coordination via adatoms is excluded. Furthermore, the binding motifs in each oligomer can be determined. [7.1 × 5.1 nm², -0.65 V, 0.12 nA]*

In contrast to the case of the 2H-P, for the Co-P only the binding motifs 1 and 3 are observed and motif 3 is clearly abundant ($96 \pm 11\%$, the large error is due to small statistics). Two dimers are shown in fig. 3.18 with their respective structural model.
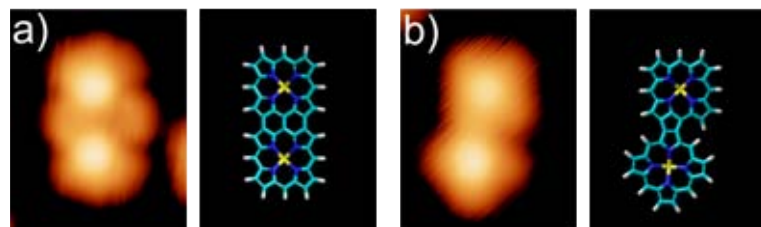
Figure 3.18: *Two binding motifs that are observed for Co-P after annealing on Ag(111) represented by two dimers (STM image and structural model). a) Binding motif 1 ($\beta - \beta, meso - meso, \beta - \beta$). b) Binding motif 3 ($\beta - \beta, meso - \beta$). [2.8 × 2.3 nm², -0.65 V, 0.12 nA]*

It is not clear, why the occurrence of the binding motifs is changed drastically in comparison to the 2H-P. The substrate temperature is slightly higher during annealing and the flux of molecules during deposition is twice as high as for the 2H-P. However, for the Co-P the covalent coupling is induced during annealing, after the deposition of the molecules, thus the flux cannot be decisive for the reaction. Furthermore, the desorption rate of Co-P at these temperatures is very small

in comparison to 2H-P. At 600 K no desorption is observed and at 630 K the desorption rate amounts to 0.019 ML/min which is less than the rate for 2H-P at 570 K. Since the desorption limits the efficiency for 2H-P coupling, high percentages of nonmonomers can be achieved by annealing for the Co-P.
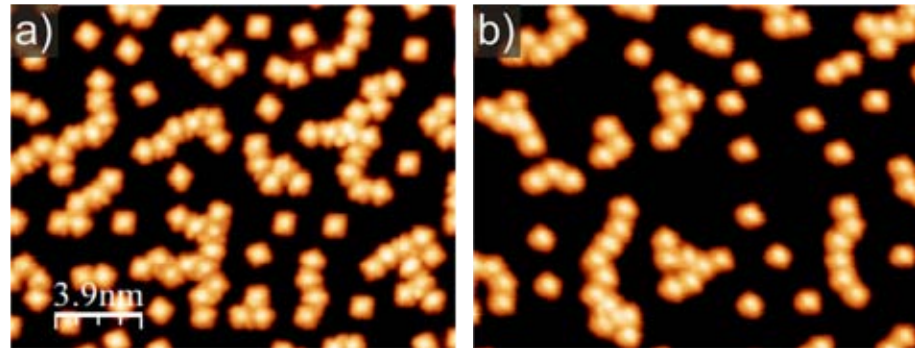
Figure 3.19: *Overview STM images of Co-P oligomers on Ag(111) formed by two different approaches. a) The sample is annealed at 630 K for 10 min and b) the sample is annealed at a lower temperature for a longer time (at 610 K for 140 min). Both approaches yield the same percentages of nonmonomers and average oligomer length. [20.9 × 16.1 nm^2, a) -0.65 V, 0.12 nA; b) -0.9 V, 0.1 nA]*

Two parameters are found to influence the percentage of molecules bound in oligomers, namely the annealing temperature and the duration. At an annealing temperature of 600 K very few oligomers are observed whereas after annealing at 630 K for 10 min $80 \pm 5\%$ of the molecules are nonmonomers. Secondly, after annealing a sub-ML of Co-P at 610 K for 20 min only $22 \pm 3\%$ of all molecules are bound in oligomers whereas annealing at the same temperature for 140 min yields $82 \pm 6\%$ nonmonomers. Thus, within the error bars, the longer annealing duration at the lower temperature (610 K) results in the same percentage of nonmonomers as annealing at a temperature 20 K higher. Moreover, the average length of oligomers is very similar for both approaches (see fig. 3.19).

These findings do not explain the differences in the occurrence of binding motifs between 2H-P and Co-P, however as shown in ch. 4.1 the presence of a metal ion in the center of the macrocycle can change the reactivity of the periphery of the molecule. In order to give a sound explanation DFT calculations need to by carried out.

3.3.2   In-situ metalation of oligomers

As shown for many different metals porphyrins can be easily metalated on a substrate under UHV conditions. [36, 89, 106–108] The same procedure is employed to a sample with 2H-P monomers and oligomers resulting in the metalation of both species with Co (see fig. 3.20d). A slight preference for the metalation of monomers in comparison to oligomers is observed: $79 \pm 4\%$ of the monomers are metalated but only $71 \pm 5\%$ of the oligomers. The similarity in appearance

(compare fig. 3.20 a to c) and the observation of the same features in $\mathrm{d}I/\mathrm{d}V$ maps leads to the conclusion that Co-P oligomers can either be formed by covalent coupling of Co-P monomers or by metalation of 2H-P oligomers. These two approaches give the opportunity to tune the structure of the Co oligomers since the occurrence of binding motifs is clearly different for both approaches.
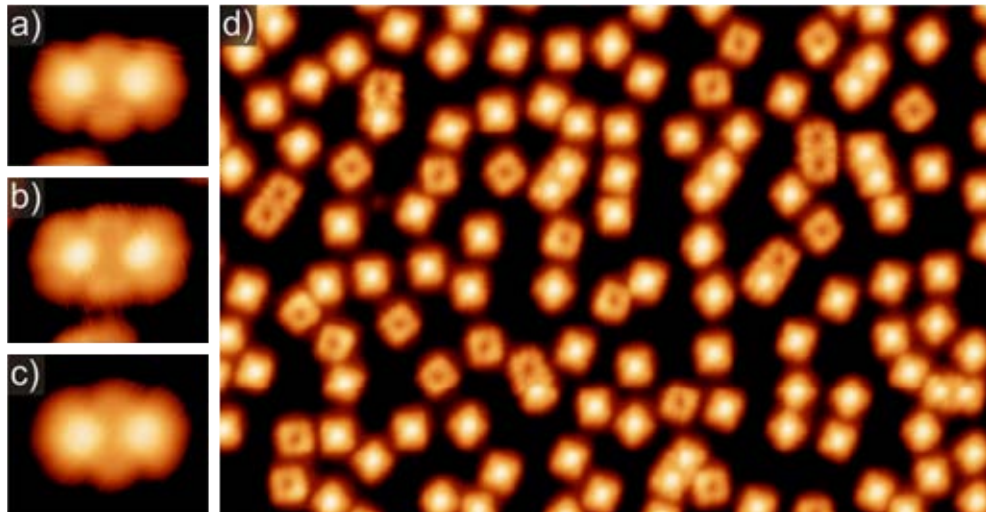

Figure 3.20: *Metalation of 2H-P oligomers with Co. a) Co-P dimer formed upon annealing Co-P at 630 K. b,c) 2H-P dimers formed upon deposition onto the sample heated to 530 K are metalated with Co. The similar appearance of a) to c) points to the formation of the same chemical species during both approaches. d) Overview STM image of 2H-P monomers and oligomers metalated with Co. [a-c) 2.8 × 2.3 nm², d) 46.1 × 30.5 nm², a) -0.65 V, 0.12 nA; b) -0.5 V, 0.15 nA; c) -0.2 V, 0.1 nA; d) -0.6 V, 0.12 nA]*

In the following, the electronic structure of the Co-P monomers and oligomers is discussed. Figure 3.21 shows $\mathrm{d}I/\mathrm{d}V$ spectra recorded along a line over a monomer along with the STM image of the monomer. The colored dots in the STM image mark the position where the respective $\mathrm{d}I/\mathrm{d}V$ spectrum is acquired. At the edges of the molecule a state around -700 mV is present (red lines), whereas in the center a broad peak around -480 mV is observed (blue line). Consequently, there are at least two occupied orbitals on different positions on the molecule in the displayed energy range.

The shape and location of the two different monomer orbitals are visualized in $\mathrm{d}I/\mathrm{d}V$ maps at different negative biases (see fig. 3.22). At a sample bias of -0.65 V a state is visible on the four corners of the monomer with two opposing corners showing a higher density of states than the other two. Energetically very close, at -0.55 V, a state in the center of the molecule is observed. This state is visible up to the Fermi energy. These findings are in good agreement with the $\mathrm{d}I/\mathrm{d}V$ spectra (fig. 3.21).
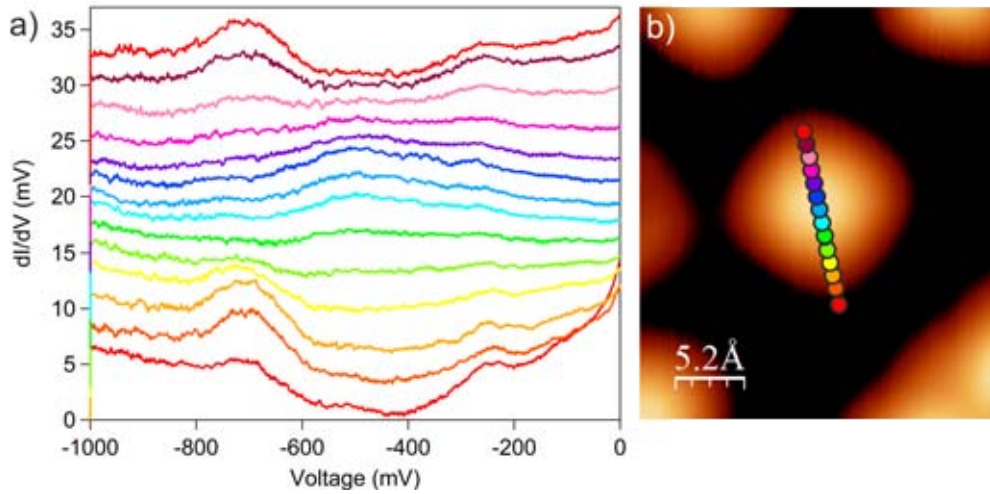
Figure 3.21: *STS on a Co-P monomer. a) dI/dV spectra recorded along a line over a Co-P monomer (plotted with offset for clarity). b) STM image of the monomer with colored dots marking the position of the respective spectrum. At the periphery of the molecule a state is present around -700 mV and in the center another state is observed at slightly lower energies (around -480 mV). [a) 0.15 nA, b) 2.8 × 3.2 nm², -0.6 V, 0.15 nA]*
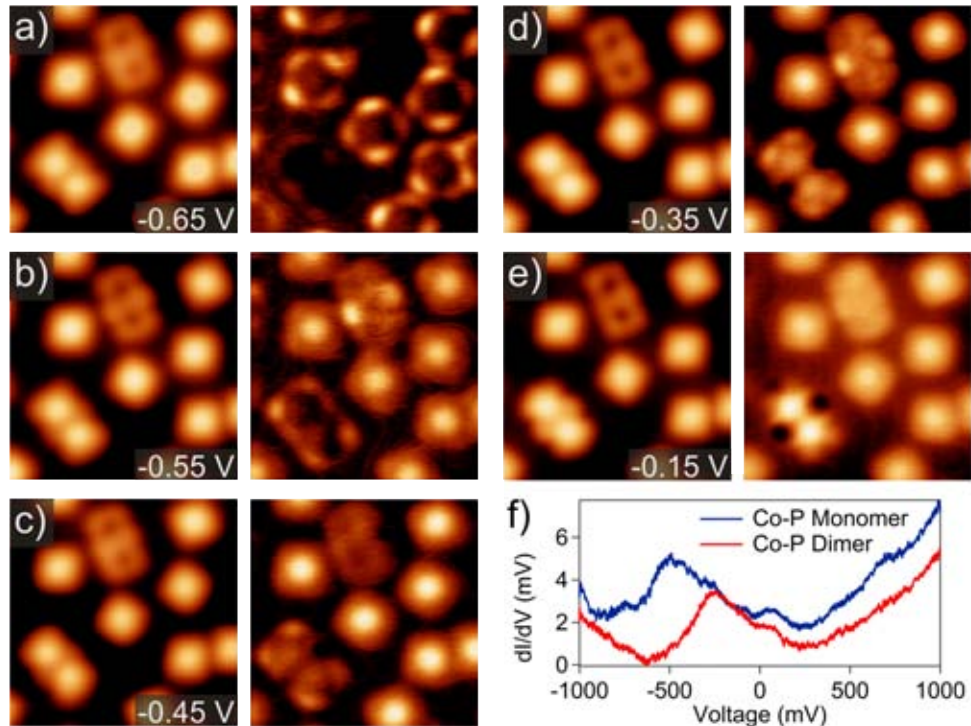
Figure 3.22: *Electronic states of the Co-P monomer and triply-fused dimer. a) to e) STM topography image (left) with simultaneously recorded dI/dV map (right) at different negative biases. a) -0.65 V, b) -0.55 V, c) -0.45 V, d) -0.35 V, e) -0.15 V. f) dI/dV curves recorded in the center of a Co-P monomer and dimer, respectively. The orbital associated with this peak is located in the center of the molecules and it is shifted closer to the Fermi level for the dimer in comparison to the monomer. [a-e) 5.9 × 5.9 nm², 0.2 nA]*

The dI/dV maps also reveal the electronic structure of a Co-P triply-fused dimer in comparison to the monomer and to a 2H-P triply-fused dimer. At -0.65 V, both dimers exhibit no density of states, however at -0.55 V they appear very differently. As mentioned above, the LUMO of the 2H-P dimer, two lobes on the central waist of the dimer, is shifted below the Fermi level between -0.55 V and -0.15 V. In contrast, the Co-P dimer exhibits a state that is localized on the edges of the molecule, very similar in shape to the state at -0.65 V on the monomer. Hence, the states on the Co-P dimer more resemble a superposition of two Co-P monomers than a 2H-P dimer. Indeed, at -0.45 V the two Co centers of the Co-P dimer show a higher density of states than at -0.55 V pointing to the onset of a state localized on the Co at this bias. Towards Fermi the density of states on the Co centers increases whereas the rest of the dimer appears dim. Thus, both the dimer and the monomer exhibit a state localized on the Co ion but their onset energy is different. This shift in energy between the state on both species is obvious in the dI/dV spectra in fig. 3.22f.

For a similar system, Co-tetraphenylporphyrins (Co-TPP) on Ag(111), the HOMO exhibits two lobes that are located on the α-pyrroles (bent upwards). This state was attributed to Co d states interacting with the π-system of the macrocycle and it reflects the bent conformation of the macrocycle where two opposing pyrrole rings point upwards and the other two downwards. [90] In the case of Co-P four lobes on the macrocycle are observed for the HOMO, whereas two of them appear slightly brighter than the other two. Since this state is not present for 2H-P it is attributed to an interaction of the macrocycle with Co d states as well. Due to its planarity Co-P is not expected to be distorted on the surface. Thus, the off-center spatial distribution of this state is not triggered by a non-planar deformation of the macrocycle. However, both molecular axes interact differently with the underlying substrate because of its three-fold symmetry. Thus, the difference in brightness between the lobes of the HOMO can be explained by the interaction of the macrocycle with the substrate which is different for the two molecular axes.

3.4   Dibromoporphines on Ag

In order to trigger the shape of nanostructures certain positions on the molecules can be designed to be more reactive than others. One example is the Ullmann coupling [27, 102, 110, 123, 127, 128] where hydrogen atoms are replaced by halogen atoms. The C-halogen bond is dissociated at far lower temperatures than the C-H bond enabling the formation of structures with a high symmetry. Another approach is to block certain positions on the molecules by *e.g.* attaching unreactive side groups (see ch. 4.2.2).

The first approach (Ullmann coupling) is employed to 2H-P molecules by synthesizing 5,15 di-bromoporphines (trans-Br-P) and 5,10 dibromoporphines (cis-Br-P) (synthesis by Thien Ngo, National Institute for Materials Science, Japan). STM images and structural models of both molecules are shown in fig. 3.23a,b. Both molecules exhibit two additional round protrusions at

the edge of the square-like shape of the macrocycle. For the trans-Br-P these protrusions caused by the two Br atoms are in opposing positions on the macrocycle. Note that in fig. 3.23a the positions of the two inner hydrogen atoms are visible on the macrocycle as well. The cis-Br-P shows two additional protrusions on neighboring sides of the molecule in agreement with the structural model. It is expected that upon adsorption on the Ag surface the Br atoms are split off the macrocycle at lower temperatures than hydrogen atoms at the periphery of the molecule. Since the radicals are most reactive at the two empty *meso*-positions the formation of straight chains of coupled molecules is anticipated.
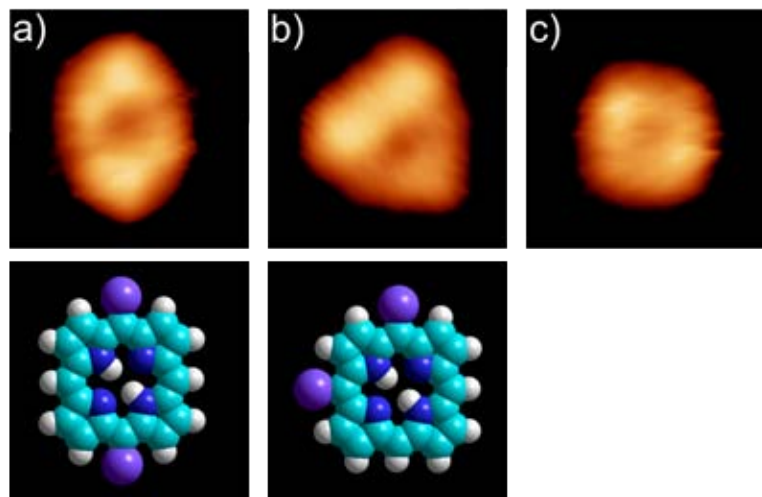
Figure 3.23: *Three different species observed upon deposition of Br-porphines onto Ag(111) held at $\approx$ 180 K. a) Trans-Dibromoporphine with structural model, Br indicated in purple, b) Cis-Dibromoporphine with structural model, c) 2H-P contaminant or debrominated porphine. [2.4 $\times$ 2.4 nm^2, a,c) -0.55 V 0.08 nA; b) -0.8 V, 0.1 nA]*

In the following, both molecules are compared for similar deposition temperatures on the Ag(111) surface (see fig. 3.24). In order to image the unreacted molecule, trans-Br-P is deposited onto Ag(111) held between 170 to 190 K (T_{cru} = 520 K, t_d = 5 min). This preparation results in a sub-ML coverage of molecules arranged in islands or small agglomerates and single molecules (see fig. 3.24a). Outside of the islands unreacted molecules (with both Br atoms attached to the macrocycle) are observed to arrange in small agglomerates or as individual units. They are identified by the two opposing additional protrusions on the macrocycle (marked by purple circle in fig. 3.24a2). However, some of the molecules exhibit only one additional protrusion on the macrocycle (marked by light blue circle) and others exhibit an appearance similar to 2H-P (marked by green circle and depicted in fig. 3.23c). Within the islands these three different species are observed as well along with small protrusions between the molecules (marked by black circle). The small protrusions show no spectral features and because no other contaminants are expected from the synthesis they are attributed to detached Br atoms. Thus, some molecules already debrominate on the surface held between 170 and 190 K.

Since 2H-P do not arrange in islands on Ag(111) the Br atoms are assumed to interact attractively with the hydrogen atoms at the periphery of the molecules. Moreover, the detached Br atoms stabilize the islands in a similar way as described *e.g.* in ref. [129].
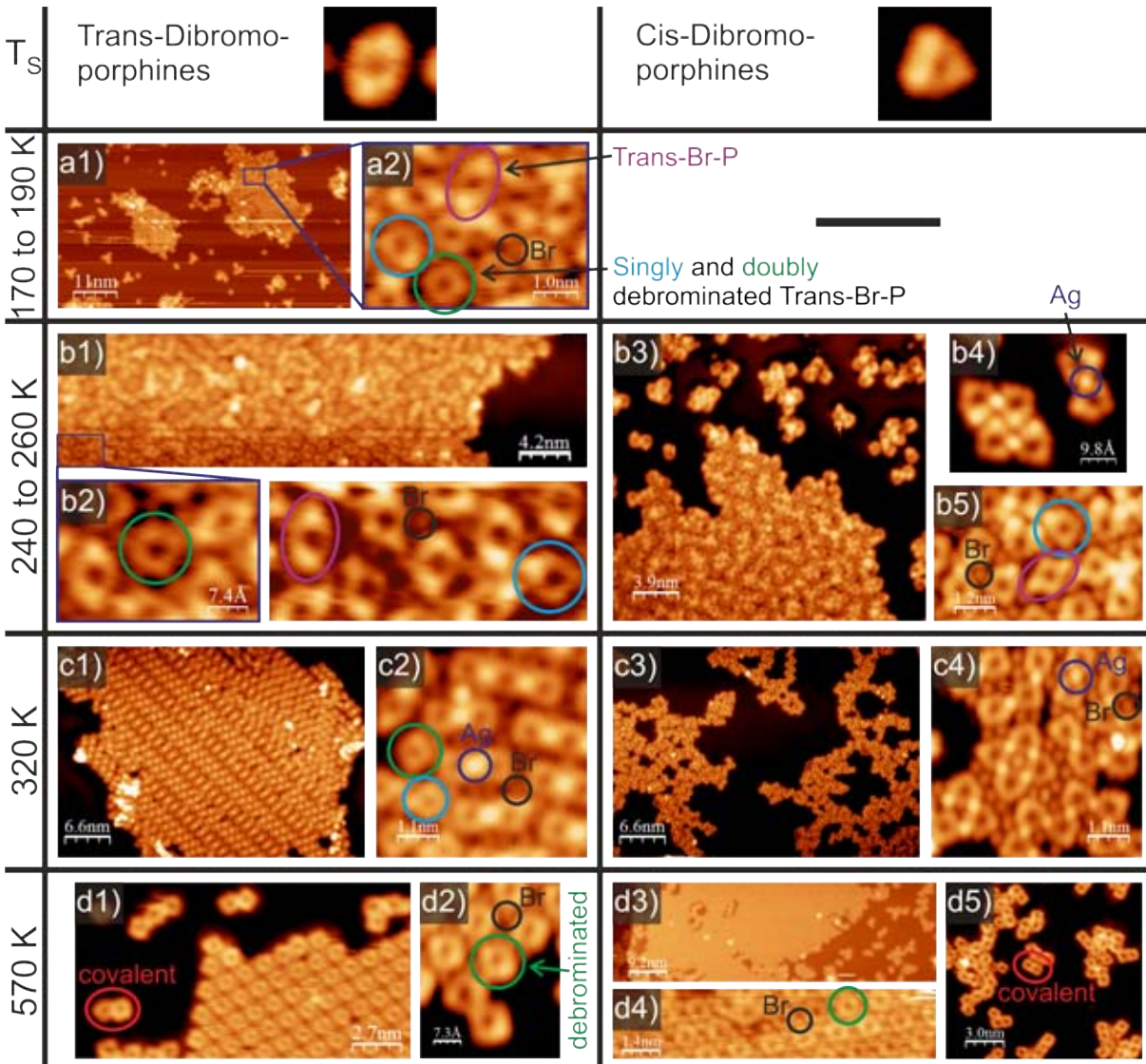
Figure 3.24: *Trans- and cis-dibromoporphines on Ag(111) deposited at different substrate temperatures T_S. For each T_S an overview and a high resolution image are shown. At lower temperatures most of the molecules are unreacted (marked by purple circle), around RT they are nearly fully debrominated and form Ag-coordinated chains and above 570 K they covalently couple (one debromination, two debrominations, Ag-coordination and covalent coupling marked by light blue, green, dark blue and red circles, respectively). The Br atoms stay on the surface until $T_S = 750$ K (marked by black circles). [a) -0.8 V, 0.08 nA; b1,2) -0.6 V, 0.08 nA; b3) -0.8 V, 0.13 nA; b4) -0.1 V, 0.2 nA; b5) -0.7 V, 0.12 nA; c1) -0.5 V, 0.2 nA; c2) -0.2 V, 0.5 nA; c3) -0.7 V, 0.13 nA; c4) -0.3 V, 0.13 nA; d1) -0.8 V, 0.08 nA; d2) -0.2 V, 0.08 nA; d3) -0.6 V, 0.15 nA; d4) -0.6 V, 0.11 nA; d5) -0.6 V, 0.15 nA]*

After annealing to or depositing at $T_S = 240$ to 260 K most of the trans-Br-P are arranged in islands and a few in smaller agglomerates of only a few molecules (see fig. 3.24b1,2). For

the trans-Br-P most of the molecules are unreacted. In contrast, the cis-Br-P start to couple at these temperatures (fig. 3.24b3-5). The molecules are arranged in extended islands and in smaller islands of several molecules. Some of the molecules, mainly within the smaller islands, are connected via a protrusion at their *meso* positions (marked by dark blue circle in fig. 3.24b4 and in fig. 3.25). The connection only appears as a protrusion at negative and small positive biases. Since the center-to-center distance is smaller than between two dibromoporphines and larger than in the covalent dimer, a coupling involving a Ag atom is assumed. In fig. 3.25 Ag-coordinated chains are depicted without (a) and with (b) Hyper-Chem models superimposed. However, within the extended islands most of the molecules are unreacted or lost only one Br atom. Moreover, most of the Ag-coordinated cis-Br-P only lost one Br atom as indicated by one remaining protrusion on the macrocycle.

While organo-metallic coordination is commonly observed on Cu, [130–133] a few examples are reported for Ag surfaces as well. [27, 123, 129, 134, 135] In contrast, for 2H-P no Ag-coordination is observed upon annealing. At a high coverage the lowest annealing temperature required to form a few dimers is 480 K where only covalent coupling is found but no Ag-coordination.
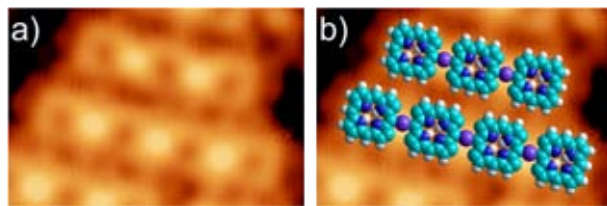

Figure 3.25: *Organo-metallic coupling of debrominated porphines with Ag atoms. STM image without (a) and with (b) structural models of Ag-coordinated chains of debrominated trans-Br-P. [3.4 × 5.2 nm^2, -0.2 V, 0.5 nA]*

Only upon annealing at higher temperatures metal-coordinated chains are formed by the trans-Br-P as well. In fig. 3.24c1,2 the surface is imaged after annealing to 320 K. Within the islands of molecules straight chains are observed where the porphines are connected via opposing *meso* positions (marked by dark blue circle in fig. 3.24c2). These chains are very limited in length, between two and five porphine units, and they are stabilized as islands by the Br atoms arranged between the chains. Furthermore, there are many molecules within the islands that are not or only partially debrominated. For the same annealing temperature (320 K) the appearance of the cis-Br-P is very different. Due to the Br atoms being positioned at neighboring *meso* positions of the molecule, no straight Ag-coordinated chains are formed but a disordered network. In contrast to the trans-Br-P, chains of more than ten porphine units are observed and all molecules are debrominated. Only a few molecules are not Ag-coordinated.

The stability of the Ag-coordinated chains is tested for the cis-Br-P by lateral manipulation. The tip is brought very close to the surface by lowering the applied voltage to 0.008 V and the tunneling current is set to 2 nA. Then, the tip positioned over a Ag-coordinated chain is moved

(indicated by arrow in fig. 3.26a) and the whole chain moves without breaking the Ag coordination (see fig. 3.26b).
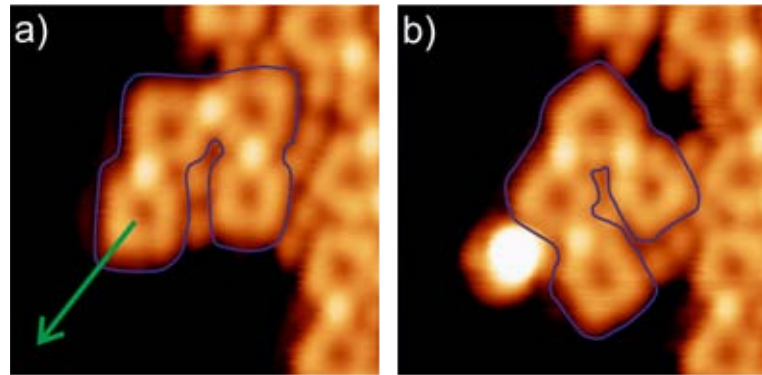
Figure 3.26: *Lateral manipulation on one molecule of a Ag-coordinated chain leads to movement of the whole chain (outline of the organo-metallic chain marked in blue). a) Before manipulation, the movement of the tip is indicated by green arrow. b) After manipulation. The additional protrusion is probably dropped by the tip. [5 × 5 nm², -0.5 V, 0.13 nA]*

An increase of the annealing time from 5 to 60 min for the trans-Br-P does not lead to longer Ag-coordinated chains, but to an increased amount of contaminants on top of the islands.

In order to convert Ag-coordinated networks into covalent networks the molecules are annealed at 570 K (see fig. 3.24d). Indeed, for both molecules covalent coupling is observed (marked by red circle), nevertheless for the trans-Br-P the majority of the molecules is either arranged in islands of debrominated and not-coordinated molecules or debrominted and singly distributed over the surface. Only a small percentage of molecules is covalently coupled in dimers or trimers. On the other hand, for the cis-Br-P a higher percentage of molecules is covalently coupled.
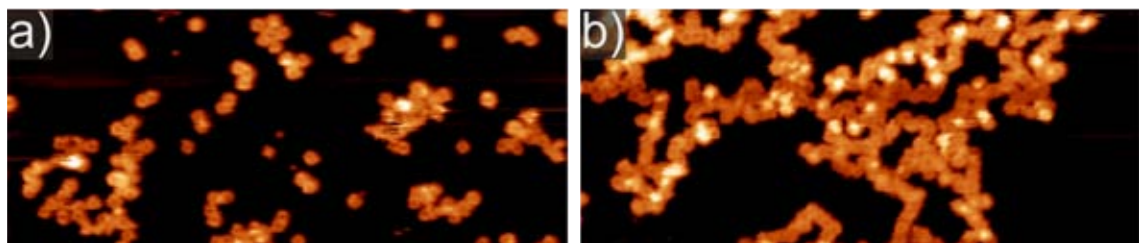
Figure 3.27: *Annealing at higher temperatures: a) STM image of trans-Br-P on Ag(111) after annealing at 620 K. The covalent structures lack order and extended length. b) Cis-Br-P on Ag(111) after annealing at 750 K: Disordered extended covalent networks. [47.6 × 20.2 nm², a) 1.2 V, 0.03 nA; b) -0.7 V, 0.1 nA]*

Since for both molecules no extended covalent chains or networks are obtained, the annealing temperature is further increased. Figure 3.27a shows trans-Br-P after annealing at 620 K. Despite the majority of the molecules being covalently coupled, no regular structures can be

observed and the chains are still rather limited in length. The presence of contaminants on the surface inhibited the resolution of binding motifs.

More extended covalent networks are observed for cis-Br-P after annealing to 750 K (fig 3.27b) and no Br atoms are resolved. The covalent structures resemble the shape of the Ag-coordinated chains and they are extended over several 100 Å. The bright spots in the center of some porphines are presumably Ag atoms incorporated into the macrocycle (see ch. 3.1.1).

As the deposition onto a heated sample results in more efficient covalent coupling for the 2H-P, cis-Br-P are deposited onto Ag(111) held at 570 K for 10 min. Very similar to the preparation of annealing the sample at this temperature for 10 min islands of single, debrominated molecules are present as well as smaller agglomerates of covalently coupled molecules (see fig. 3.28a,b). However, an increase of the deposition time onto the heated subtrate to 45 min leads to a higher surface coverage and a disordered arrangement of covalently coupled molecules, Br atoms and debrominated porphines (fig. 3.28c). Presumably, some porphines couple via Ag atoms (marked by blue circle in fig. 3.28c).
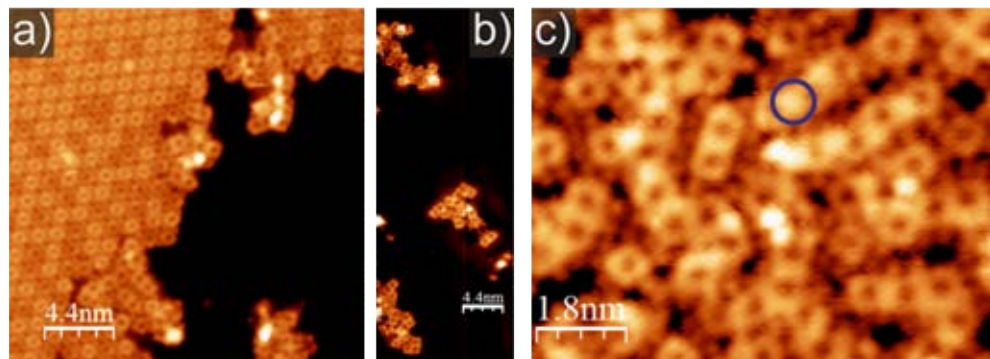
Figure 3.28: *Deposition onto the heated sample: a,b) STM images of the surface after deposition of cis-Br-P onto Ag(111) held at 570 K for 10 min. Islands of debrominated molecules and covalent coupling coexist. c) Prolongation of the deposition time to 45 min results in a high coverage of debrominated and mostly covalently coupled porphines. [a) 23.7 × 23.7 nm², -1 V, 0.1 nA; b) 15.8 × 40.6 nm², -0.7 V, 0.09 nA; c) 9.9 × 7.7 nm², -0.9 V, 0.06 nA]*

The substrate geometry seems to play a minor role as shown in fig. 3.29. Cis-Br-P are deposited onto the Ag(100) surface and annealed at 370 K. The Ag-coordinated structures resemble the ones on Ag(111) obtained by annealing at 320 K.

In order to clarify if the central hydrogen atoms are detached, voltage pulses that induce tautomerization are applied to the center of the molecules. In fig. 3.30a a voltage pulse of -1.5 V is exerted on the edge of a singly debrominated Br-P on Ag(100) (marked by green dot). Since the symmetry of the molecule is broken by the Br atom, the change in appearance from the top to the bottom panel can only be achieved by tautomerization and a small lateral movement of the molecule. The jump in the measured current is shown between the two STM images. In
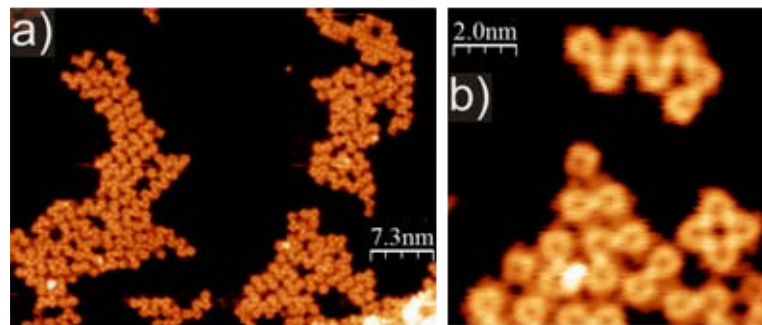
Figure 3.29: *STM images of cis-Br-P on Ag(100) after annealing at 370 K. The debrominated porphines are connected via Ag atoms, in a similar way as on Ag(111). [a) 52.6 × 39.6 nm², -0.6 V, 0.17 nA; b) 10.7 × 10.7 nm², -0.4 V, 0.17 nA]*

fig. 3.30b a voltage pulse of 2 V is exerted on the bottom debrominated monomer (marked by green dot) which causes tautomerization of both monomers in the center of the image (marked by green arrows). Finally, in fig. 3.30c dI/dV spectra in the range from -1 to 1.5 V are recorded in close proximity of the Ag-coordinated chain in the center of the image. The green arrow indicates that one of the Ag-coordinated porphines tautomerizes. Thus, the three different species - the partially reacted, the debrominated and the Ag-coordinated porphines - do not lose their inner hydrogens upon adsorption and annealing to 320 K.
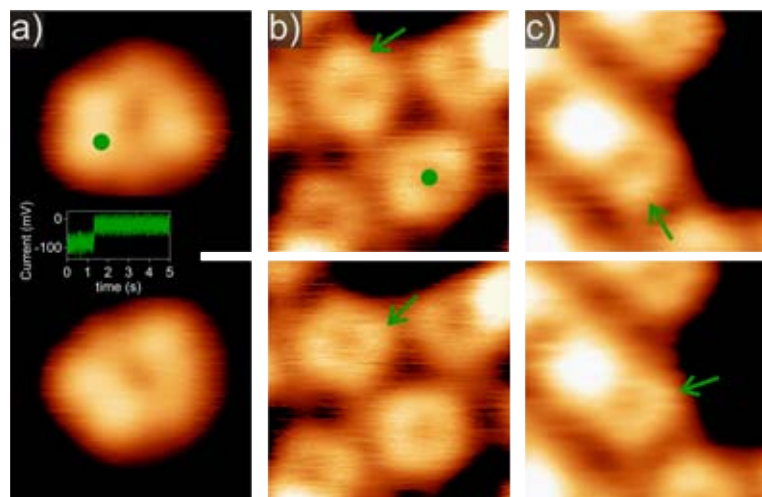
Figure 3.30: *Tautomerization of the two hydrogen atoms in the center of the macrocycle on different species. a) A switch of the inner hydrogens of a singly debrominated Br-P on Ag(100) is induced by a voltage pulse of -1.5 V at the position of the green dot. b) Two doubly debrominated porphines tautomerize after a voltage pulse of 2 V (position of inner hydrogen indicated by green arrow for upper molecule). c) The green arrow shows a switch of the hydrogen in a Ag-coordinated porphine after recording dI/dV spectra close by. [2.6 × 2.6 nm², a) -0.7 V, 0.1 nA; b) -0.2 V, 0.5 nA; c) 0.1 V, 0.3 nA]*

The above findings invoke the question of how the covalent coupling reaction takes place. The

comparison of the behavior of both molecules at the same temperatures points to a higher reactivity of the cis-Br-P, *i.e.* that these molecules are fully debrominated at a lower temperature than the trans-Br-P (namely after annealing at 320 K for the same time as for trans-Br-P) and that the cis-Br-P covalently couple more efficiently at 570 K. However, the covalent structures exhibit a considerably different shape in comparison to the Ag-coordinated chains which are straight for the trans-Br-P. This behavior is observed for other molecules that form protopolymers on Ag as well with the tentative explanation that the molecules can react in several different ways giving rise to disordered structures. [128,135] The same is true for the Br-P since at an annealing temperature of 570 K also dehydrogenation takes place increasing the number of possible coupling motifs. Thus, future experiments could aim for an intermediate annealing temperature, at which the Ag-C bonds are broken but no dehydrogenation occurs.

Furthermore, it is not clear why closely arranged debrominated porphines are observed after deposition on the sample held at 570 K for 10 min. The adsorption on the heated surface obviously leads to debromination but not necessarily to covalent coupling. After only 10 min of deposition the coverage might be too low for an efficient coupling. Although at the imaging temperature of 6 K the debrominated molecules are arranged in dense-packed islands they might be more separated at elevated temperatures and only arrange in islands during cooling. In line with this explanation is the observation that at higher coverages (deposition time of 45 min) the majority of all molecules is coupled (either covalently or via Ag atoms).

Figure 3.31 shows that the three different species - unreacted trans-Br-P, debrominated porphine and Ag-coordinated porphine - exhibit pronounced differences in the dI/dV spectra in comparison to the featureless spectrum of the 2H-P. In the occupied range no peak is observed up to -1000 mV and in the unoccupied range all three species show a broad peak with a shoulder between 500 and 1000 mV. For the brominated porphine the main peak is at slightly lower energies than for the other two species. Thus, the unreacted and the debrominated species seem to be chemically different as already assumed above.

Finally, dI/dV maps acquired on covalently coupled Br-porphine dimers exhibit the same two-lobe state below the Fermi level as the 2H-P. As shown in fig. 3.32 the two protrusions on the waist of a triply fused dimer are visible at a sample bias of -0.35 V and -0.45 V (bottom right corner of the image) confirming the formation of the same molecule as for the 2H-P.
Moreover, a similar state is observed on a triply fused trimer. In the same bias range as for the dimer two protrusions are present on the trimer (upper left part), whereas one of them exhibits a higher apparent height than the other and they are both rather elongated in comparison to the dimer. As evident in fig. 3.32c the two lobes only appear at triply fused connections but not for the third binding motif.
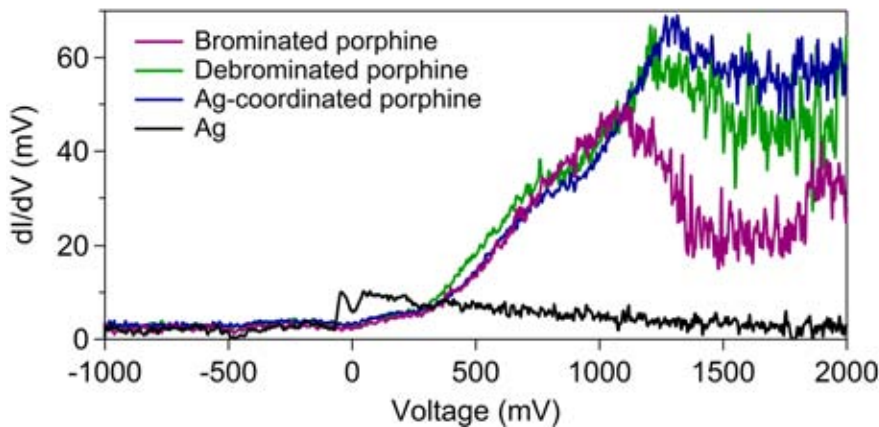
Figure 3.31: *STS on different Br-porphine species: dI/dV spectra on an unreacted trans-Br-P, a debrominated porphine and a Ag-coordinated porphine. The three species show only minor differences. [0.3 nA, 0.5 nA, 0.3 nA]*
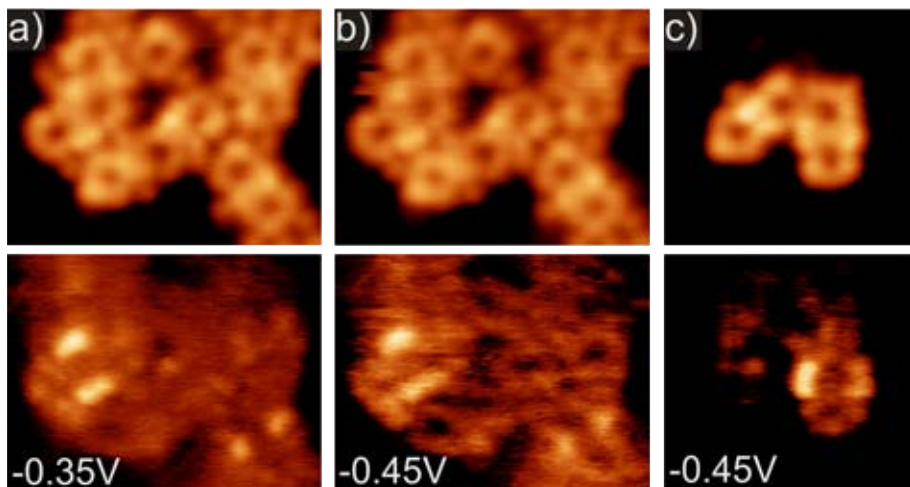
Figure 3.32: *STM topography images (top) with simultaneously recorded dI/dV map (bottom) on covalently coupled Br-porphines at -0.35 and -0.45 V. The dimer (bottom right) shows a state that is also observed on covalently coupled 2H-P and the triply-fused trimer (top left and in c) shows this two-lobed state as well. [a,b] $5.7 \times 4.3\,nm^2$; c) $4.5 \times 4.3\,nm^2$; a) -0.35 V, 0.2 nA; b) -0.45 V, 0.2 nA; c) -0.45 V, 0.2 nA]*

3.5   Summary

Porphines are promising candidates for building blocks in covalent nanostructures formed on metal surfaces under UHV conditions. The unsubstituted 2H-P is shown to undergo thermally-induced and surface-assisted dehydrogenation reactions on Ag surfaces resulting in the formation of covalent bonds. Two approaches are employed, whereas the first, which involves annealing a ML of 2H-P on Ag(111), is less efficient because the reaction is limited by the desorption of molecules. In order to counteract the desorption, in the second approach 2H-P are deposited onto a heated substrate for a deposition time that is longer than required to deposit one ML.

Employing the second approach the average oligomer length is drastically increased and nearly 100 % of all molecules are bound in oligomers (*cf.* first three rows in tab. 4). Thus, the coverage on the surface during the reaction has to be high to achieve an efficient coupling, accordingly, less coupling takes place at low surface coverages. The coupling efficiencies of the different systems discussed above are summarized in tab. 4.

For both approaches three different binding motifs are observed with the first one involving three C-C bonds and motif 2 and 3 only two C-C bonds. The triply-fused first binding motif which is also synthesized in solution [93–95] is the most abundant for all substrate temperatures investigated.

Spectroscopic measurements reveal that the LUMO is shifted below the Fermi level for the triply-fused dimer and moreover, the band gap is reduced in comparison to the monomer, a feature reported for a range of porphyrin tapes in solution. [93, 94, 96]

On a Ag surface with a different geometry (Ag(100)) the same coupling reactions are observed, however, due to a stronger molecule-substrate interaction the diffusion is reduced in comparison to the Ag(111) surface and higher temperatures are required to achieve the same amount of molecules bound in oligomers (see tab. 4). Similar to the Ag(111) surface the triple C-C bond is the preferred binding motif.

The influence of a metal center on the coupling reaction is studied by depositing Co-P onto the Ag(111) surface. The desorption is reduced in comparison to 2H-P and consequently higher substrate temperatures are required to induce the coupling reactions which yield only two different binding motifs, namely the first and the third, with a clear preference for the third one. Therefore, the presence of the metal ion in the center of the molecule changes the reactivity of the different positions at the periphery of the molecule.

For the Co-P the influence of the annealing time on the reaction is studied. It is observed that annealing at a lower temperature for a longer time leads to the same reaction outcome (percentage of nonmonomers and average oligomer length) as annealing at a higher temperature for a shorter time (see tab. 4).

Furthermore, it is shown that 2H-P oligomers can be metalated with Co, hence the shape of the oligomers can be modified since 2H-P and Co-P exhibit different preferred binding motifs.

At last, aiming for regularly shaped porphine oligomers two hydrogen atoms at *meso* positions are substituted by Br atoms. As reported for many similar cases, debromination and partial Ag-coordination takes place upon adsorption on Ag held below RT. Annealing to higher temperatures leads first to a complete Ag coordination and at 570 K covalent coupling is observed. However, the coupling is not efficient and the adsorbed Br determines the arrangement of most of the molecules. Only after annealing at 750 K all molecules are coupled and no Br atoms are observed. Despite the partial order of the Ag-coordinated chains, the covalent network shows no order.

One explanation for this behavior is that at the annealing temperature of 570 K also dehy-

Molecule	Surface	T_S (K)	Deposition/annealing time* (min)	Nonmonomers (%)
2H-P	Ag(111)	530	90	51 ± 2
2H-P	Ag(111)	570	90	80 ± 3
2H-P	Ag(111)	610	90	97 ± 3
2H-P	Ag(100)	620	40	86 ± 5
Co-P	Ag(111)	610	20	22 ± 3
Co-P	Ag(111)	610	140	82 ± 6
Co-P	Ag(111)	630	10	80 ± 5

Table 4: *Comparison of the covalent coupling reactions of 2H-P and Co-P on Ag(111) and Ag(100). The resulting percentage of nonmonomers is given for the different systems discussed above. *For 2H-P/Ag(111) the time corresponds to the deposition time onto the heated substrate, for all other cases the time refers to the annealing time.*

drogenation reactions occur, increasing the number of possible binding motifs. Thus, future experiments could try to aim for more ordered chains by annealing at a temperature at which the Br is split off but the hydrogens do not react. Another option is to employ a substrate that does not supply atoms for the formation of metal-organic chains.

Overall, the homocoupling of porphines on Ag is a cleaner approach than Ullmann coupling since no reaction byproducts remain on the surface and furthermore, the reaction is more efficient under the conditions mentioned above.

Possible future experiments comprise to study the influence of the deposition time for the coupling of 2H-P on Ag(111), the influence of the coverage on the coupling of Co-P on Ag(111), metalation of oligomers with different metals in order to study the electronic and magnetic effects (see *e.g.* [85]) and the interaction of metalated oligomers with small gas molecules. Furthermore, the conductance through oligomers could be measured by attaching one end of the oligomer at the tip and then by lifting it from the surface creating a single-molecule junction (see *e.g.* [136]).

4 Ring-closing reactions on phenyl-substituted porphyrins

Selectivity of chemical reactions is a major goal in catalysis in order to maximize the efficiency and to avoid spurious byproducts. [137–139] In industrial large scale production [140–143] as well as in biological processes [144] the most prevalent property that generates selectivity is structural symmetry of the precursors. Although this concept is widespread in homogeneous catalysis [145, 146] it still requires more understanding in heterogeneous catalysis. [138, 147, 148] In on-surface chemical reactions selectivity can be triggered by surface reactivity [117] and structure, [131] as well as by the molecular geometry. [83, 86, 149, 150] In the following, the latter parameter is shown to be decisive for the distribution of reaction products in an on-surface reaction.

The free-base tetraphenylporphyrin (2H-TPP) undergoes intramolecular cyclodehydrogenation or ring-closing reactions upon annealing on the Ag(111) surface resulting in the formation of planar porphyrin derivatives. [108, 151] The reaction is catalyzed by the substrate and four reaction products are identified by STM whereas one of the products is clearly favored over the others. Due to the observation of reaction intermediates the reaction is assumed to take place step-wise. Thus, the ground state energies of the intermediates are calculated by DFT which point to an influence of the symmetry of the core of the molecule on the reaction outcome. Indeed, two molecules with a different geometry in the core, namely Ru-TPP and Co-TPP, exhibit a more uniform distribution of the same four reaction products.

As a next step, the 5,15 Diphenylporphyrin is annealed on the Ag(111) surface. On the one hand, the two phenyl rings are expected to react with the macrocycle similar to 2H-TPP, on the other hand the hydrogenated *meso* positions are expected to dehydrogenate at elevated temperatures and covalently couple with neighboring molecules, as observed for 2H-P (see ch. 3.1.1). These two processes are observed to take place at different substrate temperatures. The two ring-closing reactions occur at lower temperatures, yielding mainly the product proposed by DFT, and these planar molecules covalently couple at higher temperatures.

4.1 Tetraphenylporphyrins on Ag(111)

Room temperature deposition of TPPs onto Ag(111) results in the formation of extended dense-packed islands of molecules. This behavior is observed for free-base TPP [107, 152] as well as for several metal-TPPs. [89, 106–108] The attractive interaction between the molecules is established by the phenyl rings which are tilted towards the surface (see fig. 4.1a). Within the islands two phenyl rings of neighboring molecules are oriented such that one phenyl ring is perpendicular to the other one. In this configuration (T-shape) the two phenyl rings interact attractively via van der Waals interaction. [107, 152] Figure 4.1b shows an island of 2H-TPP after deposition at RT ($T_{cru} = 600\,\mathrm{K}$, $t_d = 4\,\mathrm{min}$, STM image acquired by Knud Seufert) where

the outline of one molecule is marked in green.
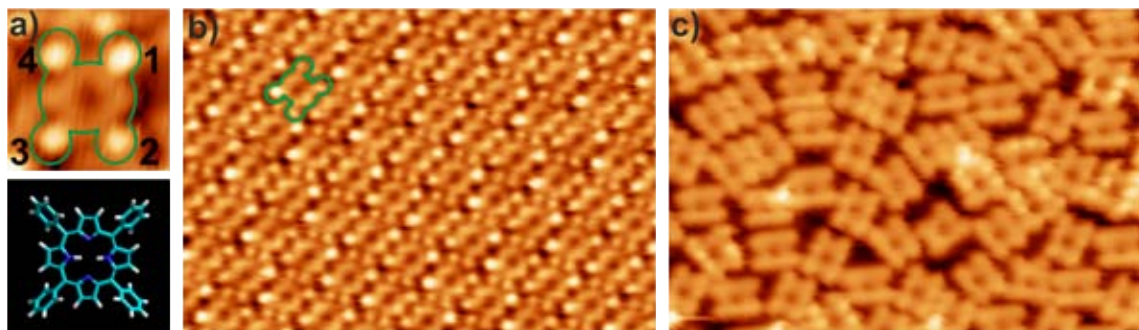
Figure 4.1: *2H-TPP on Ag(111). a) STM image and structural model. The four phenyl rings (numbered) are tilted and thus appear higher. The outline of the molecule is marked in green. b) Island formation after RT deposition. The molecules interact attractively via their tilted phenyl rings. c) Planar porphyrin derivatives after annealing at 560 K for 10 minutes. Adapted from [153]. [a) 2.1 × 2.1 nm^2, -1 V, 0.2 nA; b,c) 15.7 × 10.8 nm^2; b) -0.8 V, 0.2 nA; c) -0.3 V, 0.1 nA]*

Annealing 2H-TPP on Ag(111) between 530 and 620 K induces intramolecular dehydrogenation and ring-closing reactions as shown in refs. [108, 151]. Figure 4.1c shows the surface after annealing at 560 K for 10 min. The molecules are not ordered, exhibit a larger footprint on the surface and their apparent height is more uniform than before annealing. This conformational change was attributed to several intramolecular ring-closing reactions which result in planar porphyrin derivatives (PPD). Indeed, temperature-programmed desorption (TPD) spectra on a 2H-TPP multilayer show hydrogen evolution in the expected temperature range (TPD measurements were supervised by David A. Duncan and Francesco Allegretti). Figure 4.2 shows a broad peak in the hydrogen (H_2) spectrum (black line) with an onset temperature of 500 K which extends to above 700 K. As a comparison, the TPD spectrum with m/z (mass-to-charge ratio) 59, corresponding to the desorption of 2H-TPP (green line), exhibits a large peak at 470 K indicating the multilayer desorption and a shoulder in the large peak around 550 K where some 2H-TPP desorb during the ring-closing reactions since the PPDs have a larger footprint on the surface than 2H-TPP. The m/z 59 corresponds to 2H-TPP desorption because it is the ratio for a fragment of the unreacted 2H-TPP.

The intramolecular ring-closing reactions lead to the formation of four different PPDs (labeled as **A** to **D** in fig. 4.3, the four species observed by STM are labeled with letters and the structural models proposed by DFT (see below) are numbered). At the four phenyl rings dehydrogenation reactions take place and at the periphery of the macrocycle as well followed by the formation of a C-C bond between a phenyl ring and the macrocycle. Overall, there are sixteen possibilities how the phenyl rings can react with the macrocycle. However, there are only four different reaction products (structural models in fig. 4.3, the numbers correspond to the numbers in ref. [153]) and
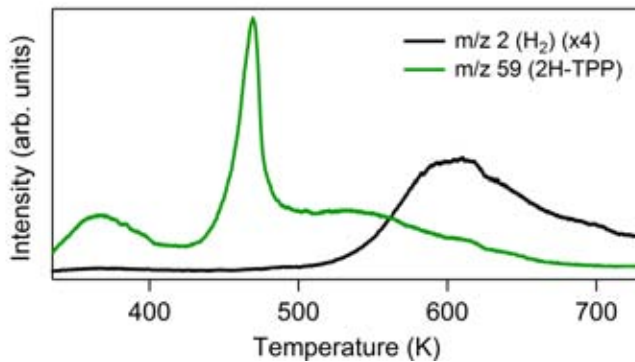
Figure 4.2: *Temperature programmed desorption spectra recorded on a multilayer of 2H-TPP on Ag(111) showing dehydrogenation (black line) and molecular desorption (green line - m/z 59, indicative of 2H-TPP desorption) at a heating rate of 0.5 Ks^{-1}. Adapted from [153].*

their tautomers. Theoretically, these four species should occur with a certain distribution corresponding to the number of equivalent reaction products, namely: Species **11**: 12.5 %, species **12**: 50 %, species **13**: 25 % and species **14**: 12.5 %. In contrast, the experimental observation of the four PPDs depicted in fig. 4.3 clearly deviates from this distribution with species **A** being clearly favored (86 %) over the other three (species **B**: 12 %, species **C** and **D**: < 3 %). The origin of this deviation is investigated below.
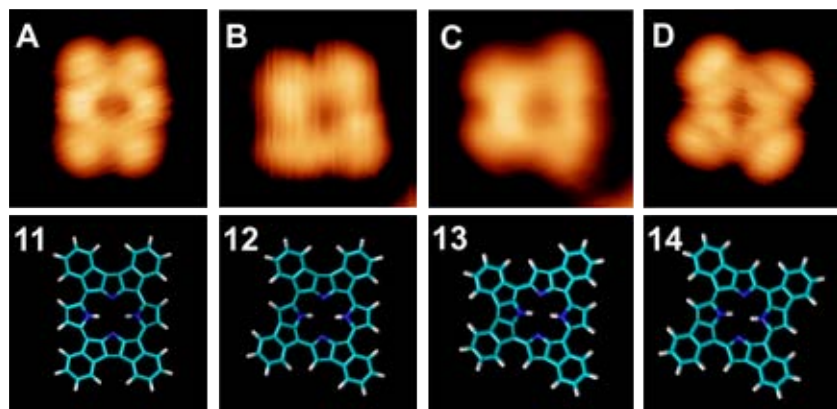
Figure 4.3: *Four planar porphyrin derivatives: STM image with tentative structural model. The molecules observed by STM are labeled by letters (**A** to **D**) and the structural models suggested by DFT are numbered (**11** to **14**, see [153]). Occurrence of the four species: **A**: 86 %, **B**: 12 %, **C**: < 3 %, **D**: < 3 %. Adapted from [153]. [2.7 × 2.7 nm^2; **A**: -0.01 V, 0.1 nA; **B**: -0.8 V, 0.2 nA; **C**: -0.8 V, 0.2 nA; **D**: -0.01 V, 0.1 nA]*

As the onset of the dehydrogenation peak in the TPD spectrum is at 500 K the sample is annealed at a slightly higher temperature, namely 520 K for 10 min. After subsequent cooling, about one fifth of the molecules is unreacted, an even smaller amount appears as PPDs and the rest of the molecules has one to three reacted phenyl rings. Figure 4.4a shows an overview

STM image with superimposed outlines of the molecules. For the unreacted molecules the four phenyl rings clearly exhibit a larger apparent height than the macrocycle because they are tilted. In fig. 4.4a some of the molecules have only three or less phenyl rings with a larger apparent height which means that some of the phenyl rings reacted with the macrocycle. Consequently, due to the observation of reaction intermediates it can be assumed that the reaction takes place step-wise. Figure 4.4b to g shows three reaction intermediates with their tentative structural models.
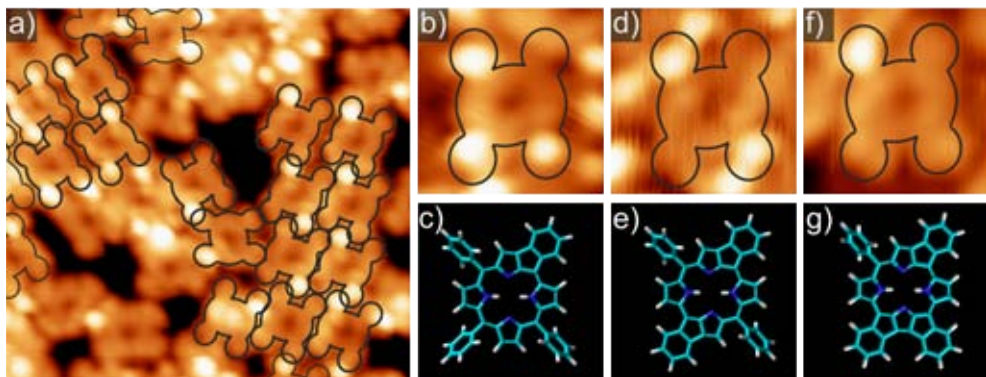

Figure 4.4: *Reaction intermediates which are partially flattened. a) STM image of 2H-TPP on Ag(111) after annealing at 520 K for 10 min. For most of the molecules one or more phenyl rings reacted with the macrocycle. The outlines of the molecules are shown in black. b) Intermediate species 1 with one flat phenyl ring with c) tentative model. d) Intermediate species 2 with two flat phenyl rings with e) tentative model. f) Intermediate species 3 with three flat phenyl rings with g) tentative model. Adapted from [153]. [a) 10 × 9.2 nm^2; b,d,f) 2.1 × 2.1 nm^2; 0.2 nA; a,d) -1 V; b,f) -0.5 V]*

The observation of reaction intermediates motivates to examine the reaction pathway by DFT calculations (carried out by Julian A. Lloyd). The comparison of ground state energies of different possible reaction intermediates gives the preferred reaction pathway. In general, the rate of a chemical reaction depends mainly on the barrier height. Since the ring-closing reactions described above involve very similar reactions - dehydrogenation and C-C bond formation - it can be assumed that the barrier height is inversely proportional to the enthalpy of reaction (Bell-Evans-Polanyi principle). [154] Consequently, the reaction which occurs with the highest probability has the highest enthalpy of reaction, *i.e.* the lowest ground state energy. The calculations are performed without a substrate because the reaction temperature is close to the desorption temperature of the molecules reducing significantly the molecule-substrate interactions during the reaction.

A detailed description of the reaction pathway is given in ref. [153]. In summary, the reaction product with minimal ground state energy in all steps of the reaction yields species **11** (see fig. 4.3). The appearance of the majority species observed by STM, species **A**, is in good agreement with the structural model of species **11**. The tautomer of **11**, and species **12** to **14** exhibit significantly higher ground state energies than **11**. For the unreacted 2H-TPP the two

tautomers are degenerate, [155] however already for the first ring-closing reaction the ground state energies of the tautomers are different. This difference increases in the course of the reaction pathway towards 0.55 eV for species **11**. Accordingly, no tautomerization is observed by STM after voltage pulses exerted on the PPDs (*cf.* [23]). With no influence from the substrate being responsible for the selectivity towards species **11** the energetic difference of the tautomers points to an influence of the symmetry of the core of the molecule. Consequently, it is expected that a change of this symmetry, *e.g.* by incorporation of a metal ion, changes the occurrence of the reaction products.

Indeed, it is shown that Ru-TPP molecules undergo the same ring-closing reactions on the Ag(111) surface upon annealing at slightly higher temperatures, namely 620 K (STM experiments supervised by Anthoula C. Papageorgiou and Joachim Reichert). [153] Furthermore, planar Co-porphyrin derivatives are observed on Ag(111) after annealing at 560 K. Four different species are observed for Ru-TPP and Co-TPP and their shape is very similar to species **A** to **D** observed for 2H-TPP molecules (see fig. 4.5 for Co-TPP).
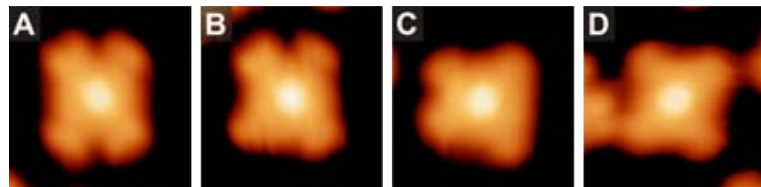
Figure 4.5: *Four planar Co-porphyrin derivatives on Ag(111) after annealing at 560 K for 10 min. They exhibit the same shape as the species **A** to **D** formed by the free-base porphyrin. [2.7 × 2.7 nm^2; -0.7 V, 0.2 nA]*

The occurrence of the four planar species is plotted in a histogram in fig. 7.7 for Ru-TPP (red), Co-TPP (yellow) and 2H-TPP (green). As anticipated above, the distribution of the four reaction products is clearly different for the two metal-porphyrins in comparison to the 2H-porphyrin. Whereas species **A** is clearly favored for the 2H-TPP, for both Ru-TPP and Co-TPP the four reaction products appear in more similar amounts. Furthermore, in ch. 4.2.1 it is shown that the 5,15 Diphenylporphyrin mainly forms the reaction intermediate proposed by the DFT calculations.

These experimental findings corroborate the assumption deduced from the DFT calculations that the symmetry of the core of the molecule influences the outcome of the ring-closing reactions. By reducing the symmetry of the core (from metal-porphyrin to 2H-TPP) the selectivity is increased.
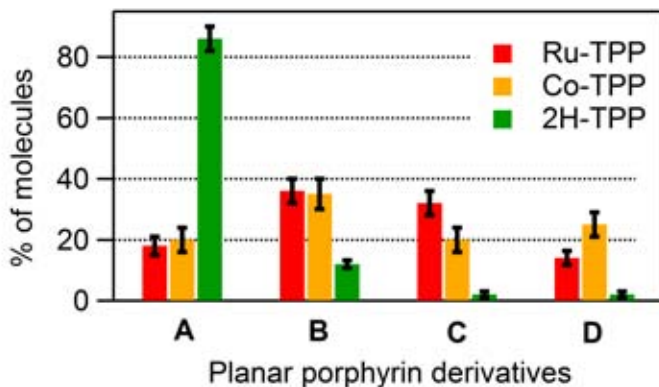
Figure 4.6: *Histogram of four planar porphyrin derivatives on Ag(111) for Ru-TPP (red), Co-TPP (yellow) and 2H-TPP (green). Only for 2H-TPP one species (namely species **A**) is clearly favored. Error bars correspond to standard deviation.*

4.2   5,15-Diphenylporphyrins on Ag and Cu surfaces

The 5,15 Diphenylporphyrins (DPP) are expected on the one hand to exhibit a similar re-activity at the hydrogenated *meso* positions as the porphine and on the other hand to become planar on the surface by heat-induced ring-closing reactions involving the two phenyl rings. In the following, the interplay of both processes is studied on Ag and Cu surfaces.

After RT deposition of DPP on Ag(111) ($T_{cru} = 560 \, \text{K}$, $t_d = 1 \, \text{min}$) the molecules are unreacted and arrange in single, double and rarely broader chains. A single DPP is depicted in fig. 4.7a with the structural model in b. The macrocycle appears with a depression in the center and two protrusions on opposing edges which mark the positions of the central hydrogen atoms. Two protrusions attached on opposing sides of the macrocycle correspond to the tilted phenyl rings. Due to the tilting the C and H atoms that are the furthest away from the surface are not positioned on the symmetry axis given by the two opposing *meso* positions but slightly offset. Therefore, the two protrusions appear closer to the β than to the *meso* positions.

In order to understand the intermolecular interactions structural models are superimposed in fig. 4.7d. Since the T-type interaction in 2H-TPP islands takes place between two phenyl rings that point in different directions perpendicular to each other, this interaction is not possible for the DPP. However, as evident in fig. 4.7d the tilted phenyl rings can interact with the planar macrocycle of a neighboring molecule. This interaction seems to be stronger for molecules in the same chain (marked by dark green circle) because mostly single chains are observed but it is also strong enough between the chains to form some double and broader chains (marked by light green circle).
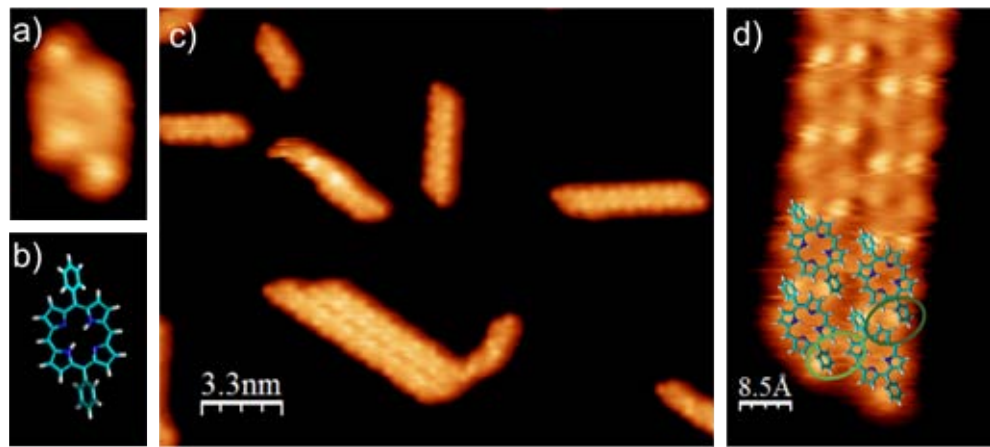
Figure 4.7: *5,15-Diphenylporphyrin on Ag(111) after RT deposition. a) High resolution STM image with b) structural model. c) Overview STM image: The molecules arrange in single or double chains. d) Double chain with structural models overlaid. The tilted phenyl rings can interact attractively with the macrocycle of a neighboring molecule. [a) $1.6 \times 2.5\,nm^2$, -0.04 V, 0.1 nA; c) $23.7 \times 18.8\,nm^2$, -0.6 V, 0.1 nA; d) $4.5 \times 7.6\,nm^2$, -0.05 V, 0.7 nA]*

4.2.1   Ring-closing reactions on Ag and Cu

Upon annealing DPP on Ag(111) the molecules undergo a conformational change and they are no longer arranged in chains but singly dispersed. After annealing at 520 K for 20 min a few molecules appear different and after annealing at 580 K for 20 min all molecules reacted. Figure 4.8a and b depict the majority and minority species, respectively, with their tentative structural models. Due to the similarity to 2H-TPP it is assumed that the same dehydrogenation and C-C bond formation reactions take place as described above (ch. 4.1), with the only difference that only the two phenyl rings react with the macrocycle. Thus, the two species observed after annealing exhibit a uniform apparent height pointing to the formation of planar molecules.

In general, four different reaction products are possible for the two ring-closing reactions, since each phenyl ring can either react with the pyrrolic (-NH) or the iminic (=N) part of the macrocycle. The structural models of these four products are depicted in fig. 4.9. For species a both phenyl rings reacted with the iminic parts and for species x both phenyl rings reacted with the pyrrolic parts. b and y are equivalent under rotation. In order to compare these structural models to the STM data it has to be considered that the unreacted molecules have two possibilities to adsorb on the surface, *i.e.* the molecule itself and its mirrored counterpart can be observed. The same is true for the reacted molecules. With the two central hydrogens marking a symmetry axis on the molecule a precise identification of the molecules in the STM images is possible by superimposing structural models. Overall, the majority of the molecules appears as species a and a smaller amount as b, whereas x is not observed (in 200 molecules). A detailed statistical analysis is given below.
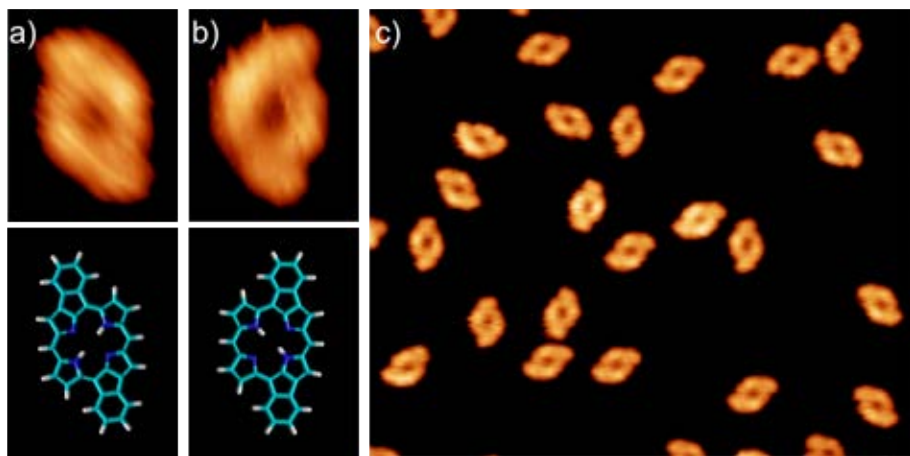
Figure 4.8: *Ring-closing reactions on DPPs on Ag(111). a) Majority and b) minority reaction product with structural models. The apparent height of the phenyl rings is significantly reduced pointing to a reaction with the macrocycle resulting in a planar molecule. c) Overview STM image after annealing at 580 K for 20 min. The molecules are not arranged in chains anymore due to the missing interaction of the tilted phenyl rings with the macrocycle. [a,b) $1.8 \times 2.3\,nm^2$; c) $19.7 \times 16.2\,nm^2$; -0.2 V, 0.15 nA]*
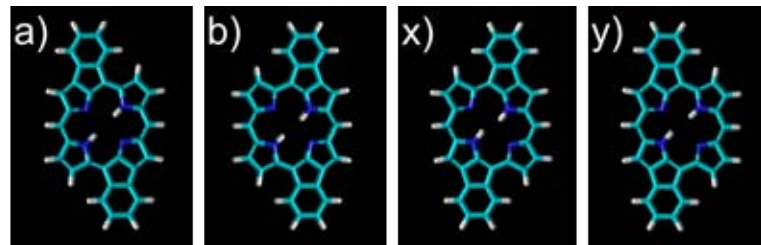
Figure 4.9: *Four possible reaction products of the two ring-closing reactions on DPP on Ag(111). a) Majority species, b) and y) are equivalent under rotation, x) is not observed. Structural models obtained by Hyper-Chem.*

The fact that species x is not observed after annealing DPP molecules is in good agreement with the DFT calculations on 2H-TPP. As shown in ref. [153] the ground state energy for a porphyrin with two phenyl rings that reacted with the macrocycle is minimal for species a. Thus, the two ring-closing reactions of DPP on Ag(111) are an additional experimental indication that the reaction pathway proposed by DFT describes the ring-closing reactions on 2H-TPP.

Annealing DPP molecules on a Ag(100) surface induces the same ring-closing reactions.

Similar to the case of the 2H-P, for the DPP a few planar species with a protrusion in the center are observed after annealing on Ag(111) and Ag(100). Figure 4.10 shows the two different planar species with a protrusion in the center on the Ag(100) surface which was annealed at 610 K for 10 min. Due to the similarity to 2H-P interacting with Ag atoms, these DPP species are also assumed to incorporate a Ag atom from the substrate in the center of the macrocycle.

However, a change of the substrate material leads to pronounced differences of the behavior upon annealing. On Cu(111) annealing a sub-ML of DPP at 520 K for 20 min results in singly
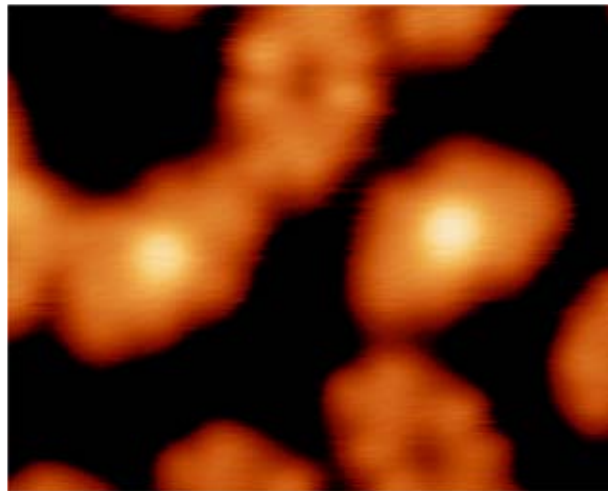
Figure 4.10: *Two different planar DPP species interacting with a Ag atom from the Ag(100) substrate which was annealed at 610 K for 10 min. [5.0 × 4.0 nm^2, -0.5 V, 0.2 nA]*

distributed planar DPP derivatives (see fig. 4.11c). High resolution STM images (fig. 4.11a,b) reveal that the molecules exhibit a uniform apparent height and their shape more resembles the planar DPP derivatives on Ag(111) than the unreacted molecules. The left molecule in fig. 4.11a,b is identified as species a and the right one as species b. At negative sample biases species a and b show a protrusion in the center that is more pronounced for species a. Whereas at positive biases the center appears similar in height to the macrocycle and the reacted phenyl rings appear higher. The protrusion in the center is attributed to a Cu atom which is incorporated into the macrocycle. Self-metalation on the Cu(111) surface was observed for 2H-P [105] and 2H-TPP. [156] For both molecules the metalation takes place at substrate temperatures around 420 K. Thus, it can be assumed that the metalation of DPP starts at a similar temperature leading to a complete metalation after annealing at 520 K. As a comparison to the appearance of the metalated DPP, Cu-P on Cu(111) is depicted in fig. 4.11 at negative (d) and positive bias (e). The Cu center appears higher at negative biases as well.

Whereas all DPP molecules are planar on Cu(111) after annealing at 520 K for 20 min, the same treatment on Ag(111) leads only to a few ring-closing reactions. Either the stronger reactivity of the Cu surface causes the higher reaction rate at this temperature or the fact that probably all molecules are metalated on Cu before the ring-closing reactions start might have an influence on the reaction. As stated in ch. 4.1 the presence of a metal atom in the center of the macrocycle instead of two hydrogen atoms has an impact on the distribution of the reaction products. Consequently, a different distribution for the reaction products a and b is expected for DPP on Ag and Cu-DPP on Cu(111) (note that a and x are equivalent for Cu-DPP). Indeed, as shown in tab. 5, the majority species is formed for roughly 90 % of the molecules on the Ag surfaces, however on Cu(111) only for 73 % of the molecules. Thus, these numbers give another hint that
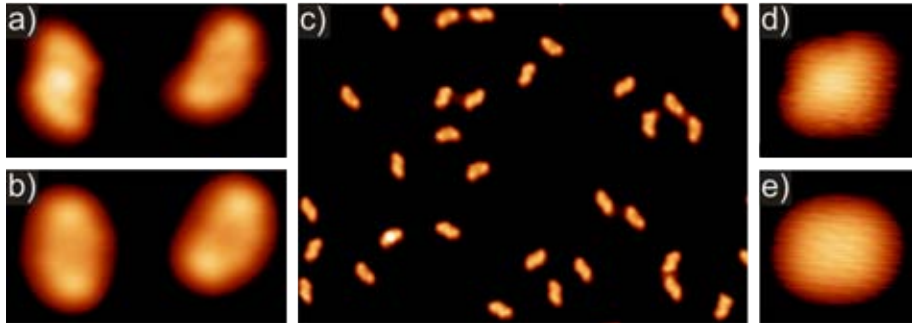
Figure 4.11: *Ring-closing reactions on DPPs on Cu(111). a) At negative sample biases the center appears higher in STM images for both planar species (left: species a, right: species b). b) At positive biases the reacted phenyl rings appear higher than the rest of the molecule. c) Overview STM image: the planar DPPs do not assemble on Cu(111). d) Cu-P formed on Cu(111) by heat-induced self-metalation of 2H-P (see [105]) at negative bias and e) at positive bias. Similarly to DPP the Cu center appears higher at negative bias. [a,b) 4.8 × 2.6 nm², c) 34.4 × 24.4 nm², d,e) 1.7 × 1.7 nm²; a) -0.7 V, 0.2 nA; b) 0.7 V, 0.2 nA; c) -0.4 V, 0.2 nA; d) -0.5 V, 0.2 nA; e) 1 V, 0.08 nA]*

the outcome of the described ring-closing reactions can be influenced by changing the geometry of the core of the molecule.

Substrate	Majority species a	Minority species b
Ag(111)	91 ± 7	9 ± 2
Ag(100)	87 ± 8	13 ± 3
Cu(111)	73 ± 6	27 ± 4

Table 5: *Ring-closing reactions of DPP on Ag and Cu: Occurrence of the two planar species (majority and minority species). Errors correspond to standard deviation.*

4.2.2   Covalent coupling on Ag and Cu

Considering that 2H-P molecules are observed to couple covalently on Ag surfaces after annealing to at least 530 K, it is expected that the two hydrogenated *meso* positions of the DPP are similarly reactive. In fact, a few coupled molecules are observed on Ag(111) and Ag(100) after annealing at 580 K and on Cu(111) as well. With this, similar structures are formed as obtained with debrominated Dibromo-diphenylporphyrins on Au(111), [157] however without any byproducts left on the surface. The amount of coupled molecules can be increased by increasing the annealing temperature. The nature of the bonds is discussed separately for the Ag and Cu surfaces in the following.

Figure 4.12 shows the Ag(111) surface after annealing a low coverage of DPP at 630 K for 20 min
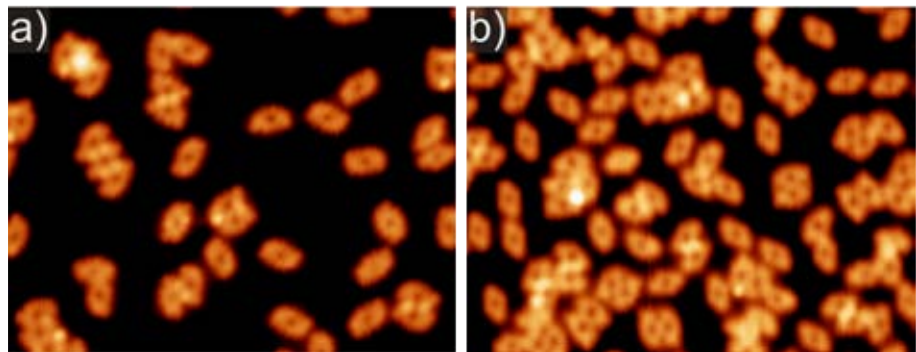
Figure 4.12: *Covalent coupling of planar DPP derivatives on a) Ag(111) after annealing at 630 K for 20 min and b) on Ag(100) after annealing at 650 K for 20 min. [21.9 × 17.0 nm², a) -0.5 V, 0.15 nA; b) 0.3 V, 0.2 nA]*

(a) and the Ag(100) surface after annealing a high coverage of DPP at 650 K for 20 min (b). The desorption is significantly smaller at these temperatures than for 2H-P on Ag(111), hence annealing after the deposition of molecules is sufficient to achieve considerable coupling between the molecules. On both surfaces monomers and oligomers are present after annealing, exhibiting no long-range order. In order to identify the nature of the bonds, structural models are superimposed with the STM images (fig. 4.13). As for the 2H-P coupling, some hydrogen atoms of neighboring molecules overlap, leaving no space for metal-coordination or van der Waals interaction. Thus, it is assumed that the molecules couple covalently.

The superposition of structural models with STM images of oligomers reveals a variety of binding motifs between the DPP molecules. Not all motifs can be identified and some appear only rarely. The five most abundant motifs are depicted in fig. 4.13. Unexpectedly, the molecules do not preferentially couple via their *meso* positions but in many cases β positions are involved and also the planar phenyl rings react with macrocycles of neighboring molecules. The single $\beta - \beta$ bond which is not observed for 2H-P coupling is the most abundant motif on Ag(111) (see fig. 4.13a). Motif 1 ($\beta - \beta, meso - meso, \beta - \beta$) and motif 2 ($meso - \beta, \beta - meso$) occur significantly less often. Additionally, two motifs involving the coupling between a planar phenyl ring and the macrocycle of another molecule are observed. The different positions of the planar phenyl rings that can form bonds are numbered as indicated in fig. 4.13a, thus the single bond in fig. 4.13e is referred to as $phenyl2 - \beta$ and the double bond in fig. 4.13f as $phenyl2 - \beta, phenyl3 - meso$.

For both surfaces, Ag(111) and Ag(100), 73 motifs are determined each and their occurrence is compared in tab. 6. Whereas on Ag(111) (after annealing at 630 K for 20 min) the preferred binding motif is the single $\beta - \beta$ bond, on Ag(100) (after annealing at 650 K for 20 min) several motifs appear in roughly similar amounts. It cannot be excluded that the temperature plays an important role for the distribution of the binding motifs since there is a difference of 20 K in the annealing temperature of both samples. However, at a lower annealing temperature, namely 610 K, no preference for a certain motif is found on Ag(100) either. Furthermore, the coverage
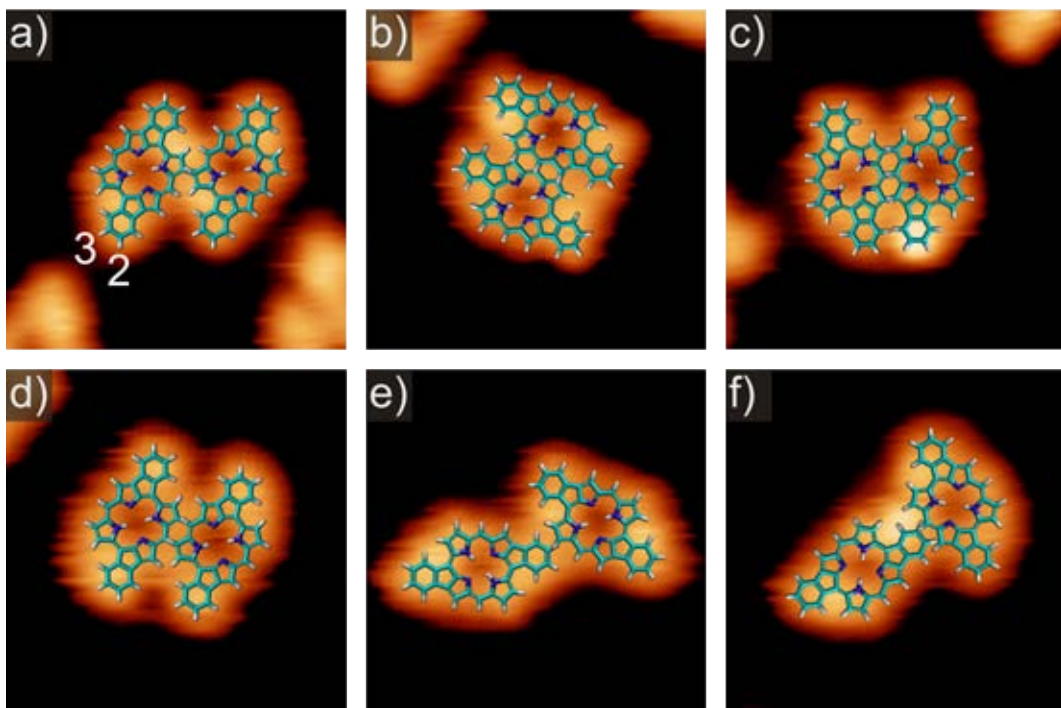
Figure 4.13: *Covalent binding motifs of DPP on Ag. a) $\beta - \beta$, b,c) $\beta - \beta$, meso$-$meso, $\beta - \beta$, d) meso$-\beta$, $\beta -$ meso, e) phenyl2 $- \beta$, f) phenyl2 $- \beta$, phenyl3 $-$ meso. [3.6 $\times$ 3.6 nm^2, 0.5 V, 0.15 nA]*

during the reaction might play a role since it is different on both samples and most importantly, the surface geometry and thus the adsorption site of the molecules is different on both surfaces.

Binding motif	Anneal at 630 K on Ag(111)	Anneal at 650 K on Ag(100)
$\beta - \beta$	37	9
$\beta - \beta$, meso $-$ meso, $\beta - \beta$ (motif 1)	16	18
meso $- \beta$, $\beta -$ meso (motif 3)	9	12
phenyl2 $- \beta$	6	11
phenyl2 $- \beta$, phenyl3 $-$ meso	5	23

Table 6: *Occurrence of different binding motifs of DPP on Ag(111) and Ag(100) in numbers of counted motifs (in total 73 for each substrate). Motifs are determined by superimposing structural models.*

Another observation during the identification of the binding motifs is that for the motifs $\beta - \beta$ and $meso - \beta, \beta - meso$ (2. motif) only molecules of the same orientation couple, *i.e.* in these motifs the molecules only couple to other molecules that adsorbed in the same way on the surface but not with their mirrored counterparts. For the other motifs also different molecules couple. The minority species appears in nearly all binding motifs, either bound to another minority species or to a majority species.

In contrast, the situation is very different on the Cu(111) surface. Firstly, the surface itself is more reactive and for many organic molecules organo-metallic coupling is observed at elevated temperatures. Secondly, the DPPs on Cu are metalated with Cu atoms from the substrate at the annealing temperatures required for covalent coupling. Thus, considering the altered occurrence of binding motifs for the metal-porphines (Co-P) in comparison to the 2H-porphine, a different reactivity of the periphery is expected for the planar Cu-DPP as well.

As shown in fig. 4.14 some Cu-DPP couple upon annealing at 570 K for 20 min. The percentage of coupled molecules is increased by annealing at a higher temperature, namely at 620 K (see fig. 4.14). The nature of the bonds and its motifs are again determined by superimposing structural models with the STM images (fig. 4.15).
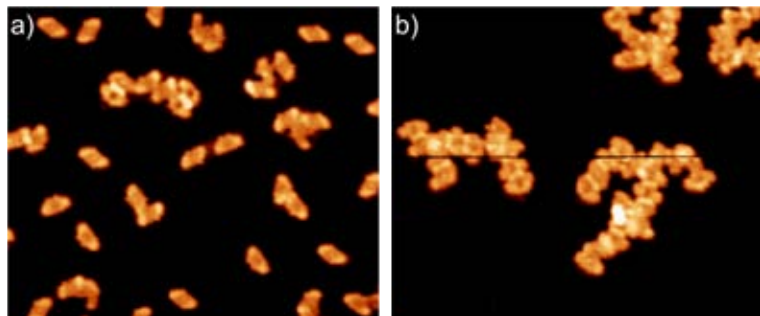
Figure 4.14: *Coupling of DPP molecules on Cu(111) after a) annealing at 570 K for 20 min and b) at 620 K for 20 min. [23.7 × 20.0 nm^2; a) -0.6 V, 0.2 nA; b) -0.8 V, 0.15 nA]*

The distances between the outer hydrogen atoms of neighboring models in fig. 4.15 point to the occurrence of Cu-coordination between molecules in some cases and covalent coupling in other cases. In fig. 4.15a the hydrogen atoms of the two neighboring molecules do not overlap and two protrusions with a greater apparent height than the molecule are present between the molecules. Since the formation of Cu-mediated bonds is frequently observed on Cu surfaces, a coupling via two Cu atoms is assumed. In contrast, in fig. 4.15b three Cu atoms are arranged between the molecule on the left and the central one.

However, the models of the central and the right molecule in fig. 4.15b overlap pointing to the formation of a covalent bond. Most of the observed covalent coupling motifs involve a single bond, either between two β positions (fig. 4.15c) or between a planar phenyl ring and a β position (fig. 4.15b,d,e). Thus, the coupling is indeed different from the Ag surface where also covalent motifs involving two or three C-C bonds are observed. In total, covalent and Cu-coordinated coupling occur in approximately similar amounts at this temperature (570 K).
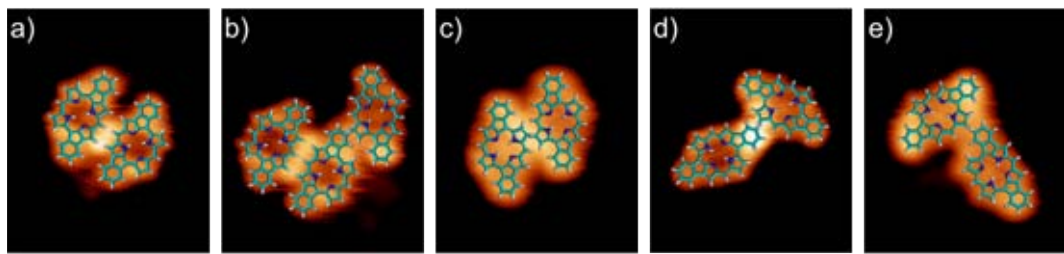
Figure 4.15: *Coupling of DPP on Cu(111) upon annealing at 570 K for 20 min: STM images of oligomers with superimposed structural models. a) Cu-coordination involving two Cu atoms, b) Cu-coordination involving three Cu atoms and covalent coupling (phenyl3 − β), c) covalent coupling (β − β), d,e) less obvious if Cu-coordination or covalent coupling. Some molecules seem to be metal-free again, e.g. in a, and some DPPs are clearly metalated with Cu, e.g. in c. [3.7 × 4.4 nm^2; a,b,d) 0.1 V, 0.1 nA; c) -0.2 V, 0.12 nA; e) -0.6 V, 0.2 nA]*

4.2.3   Electronic structure

The electronic states close to the Fermi level on planar DPPs are probed by dI/dV mapping. In fig. 4.16 two monomers and two dimers are shown on the Ag(100) surface.
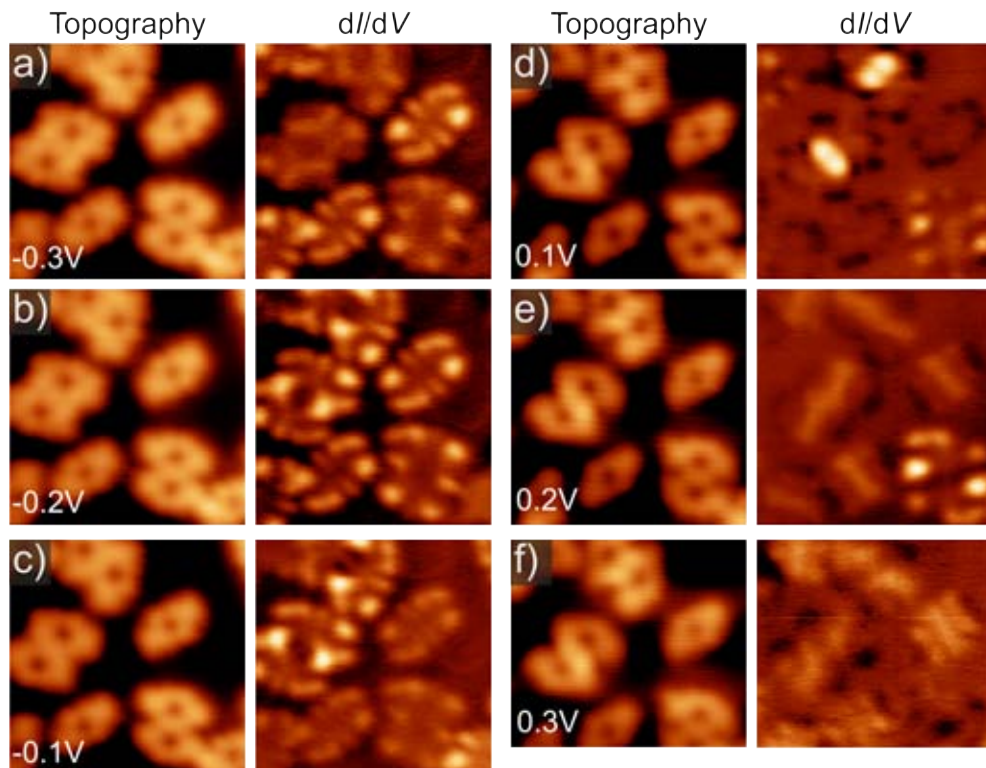
Figure 4.16: *STM topography image (left) and dI/dV map (right) on DPP on Ag(100). The dimer in the top left is singly-fused and the one in the bottom right is triply-fused. Different sample biases: a) -0.3 V, b) -0.2 V, c) -0.1 V, d) 0.1 V, e) 0.2 V, f) 0.3 V. [a-e) 5.9 × 5.9 nm^2, f) 5.3 × 5.9 nm^2; 0.2 nA]*

The dimer in the top left of the STM image is singly-fused and the one in the bottom right

is triply-fused. At -0.3 and -0.2 V the monomers exhibit a clear state that is located on the edges of the molecule with two circular protrusions and two elongated ones. Slightly closer to the Fermi level, the singly-fused dimer shows a state which is the superposition of the state on the monomer for the two molecules of the dimer. The fact that the monomers appear dim at -0.1 V whereas the singly-fused dimer shows a pronounced state, indicates that the occupied state observed on the monomer and the dimer is shifted closer to the Fermi level for the dimer. The triply-fused dimer shows a state at -0.2 V which is slightly different from the other dimer and the monomers since it only involves circular protrusions.

At positive sample biases both dimers exhibit a state on the waist of the molecule, at 0.1 V for the singly-fused dimer and at 0.2 V for the triply-fused dimer.

4.3   Summary

In summary, the symmetry of the core of a porphyrin molecule is shown to be decisive for the outcome of an on-surface chemical reaction. Upon annealing on the Ag(111) surface 2H-TPP molecules undergo several ring-closing reactions which result in planar molecules. The dehydrogenation reactions during the ring-closing are monitored by recording the hydrogen evolution temperature-dependent (TPD). All four possible reaction products are resolved by STM whereas one product is clearly favored over the others.

Since reaction intermediates are observed at lower temperatures it is concluded that the reaction takes place step-wise. The ground state energies of several reaction intermediates are calculated by DFT suggesting the minimal energy reaction pathway. Within this pathway the selectivity towards the final product is determined by the symmetry of the core of the molecule. In order to test this hypothesis, two molecules with a higher symmetry in the core are annealed on the same surface, namely Ru-TPP and Co-TPP (four-fold symmetric). For both metal-TPPs the reaction is less selective, *i.e.* the distribution of the four reaction products is more uniform than for the 2H-TPP. Consequently, these experimental results support the conclusion of the DFT calculations that a decrease of the symmetry of the core of the molecule (from metal-TPP to 2H-TPP) increases the selectivity of the reaction.

In contrast, for the DPP molecules three different processes occur upon annealing: First, the two phenyl rings react with the macrocycle in a similar way as the 2H-TPP, on both Ag and Cu surfaces. Second, in a similar temperature range the molecules self-metalate on Cu with atoms from the substrate, as it is observed for 2H-P and 2H-TPP. [105, 158] At last, the planar DPP derivatives couple covalently at elevated annealing temperatures, comparable to the covalent coupling of 2H-P on Ag (see ch. 3.1.1). On the Cu surface, both Cu coordinated and covalent bonds between planar DPPs coexist. On Ag however, more binding motifs than for 2H-P on Ag are observed and the occurrence of the binding motifs is also changed. Furthermore, more pronounced differences between the coupling on the Ag(111) and Ag(100) surfaces are observed

than for 2H-P.

In order to further substantiate the proposed mechanism of the symmetry of the molecule being decisive for the reaction outcome, more extensive DFT calculations including metal-TPPs need to be carried out or more experimental data on different metal-TPPs needs to be acquired. For the DPP molecules, non-contact atomic force microscopy (AFM) measurements could help to reveal the topographic structure of the differently coupled molecules, since Hyper-Chem calculations suggest substantial bending for some of the covalent motifs.

5   Adsorption and coupling of iron-phthalocyanine on Cu(111)

Similar to porphyrins, phthalocyanines adsorbed on metal surfaces are studied intensively with the goal to realize electronic and optoelectronic devices based on (metal-)organic molecules. [22, 40, 159] Due to their versatile properties phthalocyanines are employed in *e.g.* gas sensors, [160] solar cells, [161] and field effect transistors. [162] The ability to incorporate different metal ions in their macrocycle makes phthalocyanines promising candidates for spin-dependent electronics as well. [32, 33]

For the application in devices it is necessary to understand the interaction of the molecules with the underlying substrate, as *e.g.* the conductance through a molecule and its magnetic properties can vary with the adsorption site. [163, 164]

Upon adsorption of several metal-phthalocyanines (MPc) on different metal surfaces a change of the symmetry of the molecule is observed in STM images. In gas phase MPcs exhibit a four-fold symmetry, which is preserved on the surface for different systems as CoPc/Cu(100) [125] and Fe-,Co-,Ni-,CuPc/Ag(100). [165] However, for other systems the symmetry of the molecules is reduced to two-fold in the STM images with one molecular axis appearing higher than the other one, *e.g.* for CoPc and FePc/Cu(111), [125, 126, 163] FePc/Cu(100), [166] CuPc/Cu(111) [125, 167] and SnPc/Ag(111). [168] The origin of the symmetry reduction is still not fully understood and was attributed to either being a geometric distortion of the molecules on the surface, [126, 166] an electronic effect caused by the interaction of the molecule with the surface [163, 169] or a combination of both. [125]

Here, the system FePc/Cu(111) is studied with complementary methods pointing to an electronic effect caused by an asymmetric charge transfer and probably a slight geometric contribution due to bending of the molecule.

In the second part, a polymerization reaction of FePc/Cu(111) which was first observed by Manandhar *et al.* [170] is described. STM and XPS data point to a partial decomposition of the molecules upon annealing.

5.1   Symmetry reduction

Room temperature deposition of small amounts of FePc onto the Cu(111) surface results in a sub-ML of isolated molecules ($T_{cru} = 680\,\mathrm{K}$, $t_d = 30\,\mathrm{min}$). The coverage-dependent arrangement and island formation of FePc on Cu(111) is discussed in ref. [171] and here only coverages below $0.4\,\mathrm{ML}$ are regarded. The appearance of FePc in STM images is cross-shaped with a protrusion in the center induced by the Fe ion (fig. 5.1a with structural model in b).

The adsorption site of FePc on the Cu(111) lattice can be determined by adsorbing CO on the surface (dose in-situ for $1\,\mathrm{min}$, p: $1.0 \cdot 10^{-7}\,\mathrm{mbar}$). With CO always occupying on-top positions
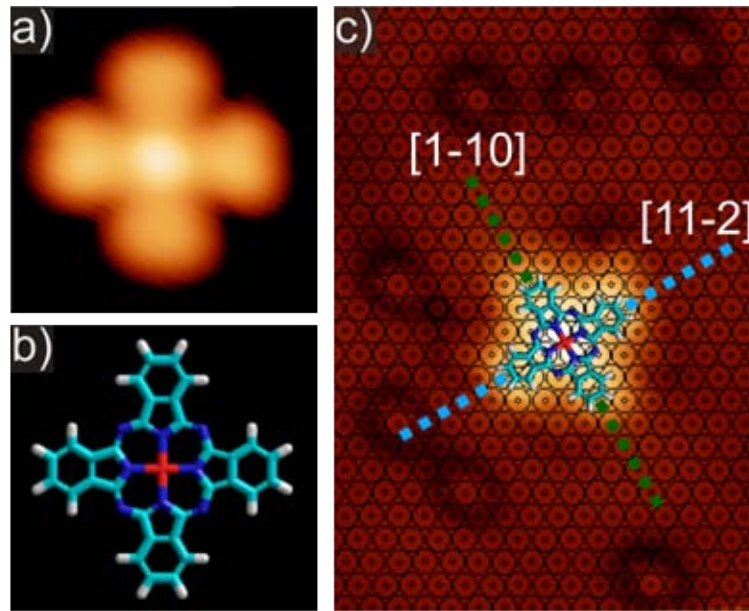
Figure 5.1: *Room temperature deposition of FePc on Cu(111). a) High resolution STM image with b) structural model. The Fe center is labeled in red. c) Determination of the adsorption site: a hexagonal lattice is fitted to the positions of co-adsorbed CO molecules revealing that the FePc molecule is aligned with one of the dense-packed directions of the crystal. The two axes of the molecule are marked in blue and green. [a) 1.9 × 1.9 nm^2, c) 4.6 × 6.5 nm^2; a) 0.05 V, 0.11 nA; c) -0.2 V, 0.5 nA]*

on the lattice at low coverage the exact adsorption site of FePc can be identified (see ref. [29]). In fig. 5.1c a hexagonal lattice representing the Cu(111) surface is superimposed with the STM image in such a way that all CO molecules are located on top sites. The superposition of the structural model of an FePc molecule reveals that it occupies a bridge site with one molecular axis (main axis) aligned with one of the three dense-packed directions of the crystal and the other axis being perpendicular to the crystal direction (secondary axis). In fig. 5.1c the main axis is marked in green and the secondary axis in blue.

The symmetry reduction introduced above is visualized in line profiles across the two molecular axes. At positive biases around 0.75 V (fig. 5.2a) there is a difference in apparent height between the two isoindole units on the main axis and on the secondary axis. Along the secondary axis the isoindole units appear with a higher apparent height than along the main axis. At negative biases this effect is less pronounced (fig. 5.2b).

However, the bias-dependent symmetry reduction is resolved across the whole molecule in constant height dI/dV maps. Since the tip height is not adjusted during the measurement as for constant current maps the resolution is higher and the imaging of the LDOS is more accurate for constant height maps. [163, 172] In fig. 5.3 the tunneling current is depicted in the top panels and its derivative in the bottom panels showing a molecule that slightly deviates from the dense-packed crystal direction (by 4°). Upon RT deposition the molecules exhibit three different
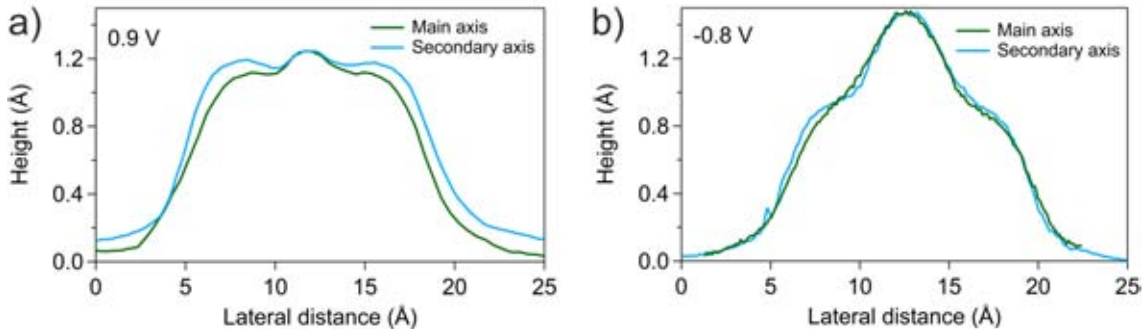
Figure 5.2: *Apparent height across both molecular axes (marked in fig. 5.1c) measured at a) -0.8 V and b) 0.9 V. The difference in apparent height between both axes depends on the voltage. [0.1 nA]*

orientations and are all aligned with one of the three crystal directions (within the accuracy of $\pm 2°$, see also [125]). Though, upon annealing to 590 K some molecules deviate up to $\pm 8°$ from these directions still exhibiting the two-fold symmetry. The annealing experiments are discussed in detail below.
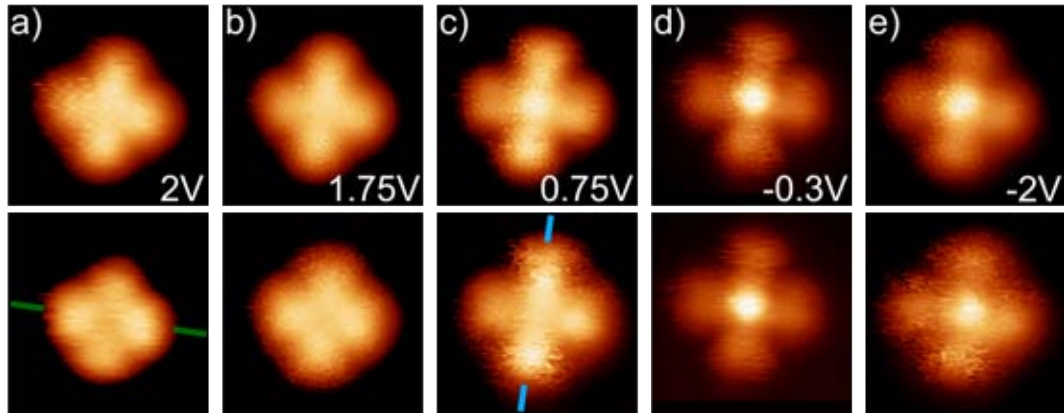
Figure 5.3: *Bias-dependent imaging of FePc on Cu(111) revealing the two-fold-symmetry of the molecule: Constant height dI/dV maps at a) 2 V, b) 1.75 V, c) 0.75 V, d) -0.3 V, e) -2 V. [2.3 × 2.3 nm^2, a,b) 0.1 nA, c-e) 0.2 nA]*

The bias-dependent imaging of the two-fold symmetry of the molecules shows that the isoindole units on the main axis appear brighter at high positive biases (2 V) and at lower positive biases (around 0.75 V) the other two (along the secondary axis) appear brighter. At negative biases the center appears very bright and the macrocycle is approximately uniform in apparent height. Since the molecule itself is four-fold symmetric, the symmetry reduction is induced by the interaction with the substrate. Snezhkova *et al.* report that the XP spectra exhibit a core level shift upon the adsorption of FePc on the Cu(111) surface in comparison to the case of FePc on graphite, where the interaction with the substrate is weaker. [30] This core level shift is

attributed to an asymmetric charge transfer from the substrate to the molecule. Therefore, a bias-dependent imaging of the symmetry reduction is observed in the STM images. Furthermore, the STM data also point to a small geometric contribution. Due to the charge transfer it is likely that the molecule is slightly bent on the surface.

In conclusion, the symmetry reduction upon adsorption is mainly induced by an electronic effect, the asymmetric charge transfer. Based on preliminary DFT calculations a minute geometric contribution can not be excluded. [30]

5.2   Polymerization reactions

Due to its similarity to porphyrins it is expected that dehydrogenation and coupling reactions of FePc molecules can be induced on the Cu(111) surface. Indeed, annealing a sub-ML of FePc at 590 K leads to the formation of oligomers. The desorption rate at this temperature is small, therefore post-annealing is sufficient to induce coupling. Not all molecules are coupled after an annealing duration of 10 min, however as mentioned above for some single molecules their orientation towards the dense-packed directions of the Cu(111) surface is slightly changed and deviates up to $\pm 8°$.
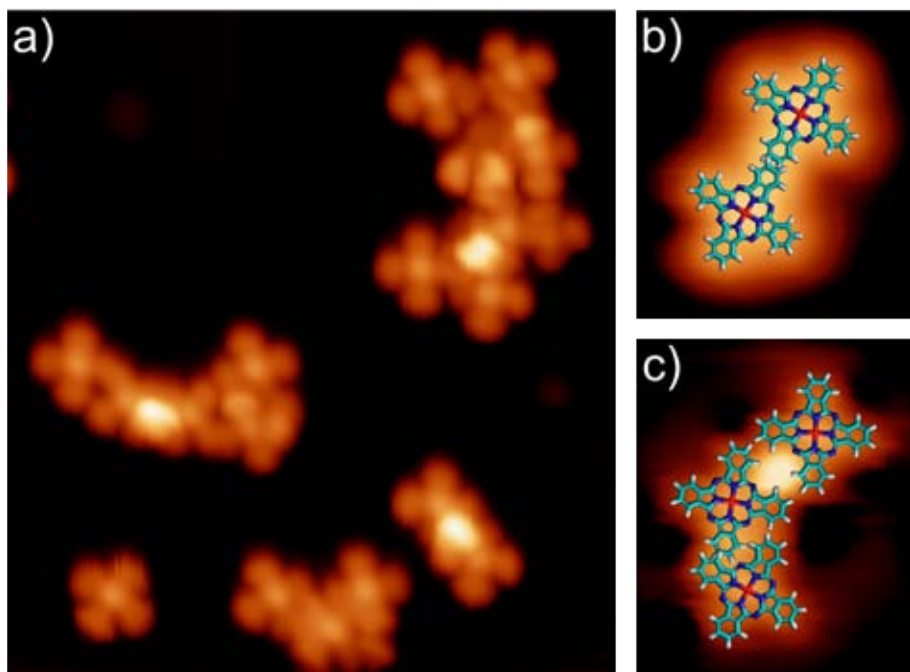
Figure 5.4: *Polymerization of FePc upon annealing at 590 K. a) Overview STM image. b,c) Oligomers with structural models superimposed. Since several hydrogen atoms overlap it is assumed that the molecules dehydrogenate and partially couple. [a) 13.1 × 14.3 nm², b) 4.0 × 3.6 nm², c) 4.4 × 3.6 nm², a) -0.8 V, 0.1 nA, b) 0.5 V, 0.1 nA, c) -0.25 V, 0.1 nA]*

The FePc oligomers are limited in length (up to approximately 20 units) and show no long-range order (see fig. 5.4a). The superposition of structural models indicates that the molecules within the oligomers partially dehydrogenate at the periphery since the structural models overlap (fig. 5.4b,c). In some cases (fig. 5.4b) covalent coupling can be assumed, however, for many other cases it is not clear how the molecules are coupled (fig. 5.4c).

In XPS measurements a shift of the N 1s and C 1s peaks is observed upon annealing. [173] Since a dehydrogenation and coupling of only the isoindole units would not significantly shift the binding energies of the nitrogen atoms, it is assumed that some molecules are fragmented. This assumption is in good agreement with the STM data where in some cases the structural models of intact molecules do not fit the units in the oligomers.

5.3   Summary

The origin of the symmetry reduction of FePc/Cu(111) obvious in STM images is investigated with complementary techniques. The STM data reveal a small geometric contribution and a more pronounced electronic effect. XPS data show a clear electronic contribution caused by an asymmetric charge transfer from the substrate to the molecule. With this approach the symmetry reduction is explained for this system and this method is also applicable to similar systems.

Upon annealing FePc on Cu(111) polymerization reactions occur. From the STM images it is clear that some molecules overlap, thus they dehydrogenate and partially couple covalently. However, XPS and also STM data point to a partial fragmentation of the molecules.

Compared to similar systems described above, the annealing temperature (590 K) is relatively low for a substantial part of the molecules being decomposed. Porphines and DPPs are observed to covalently couple upon annealing, but their macrocycles remain mostly intact up to 630 and 650 K, respectively (see ch. 3 and 4.2).

6 Interaction of metalloporphyrins with diatomic gas molecules

The adsorption and binding of small ligands to surface-supported functional molecules is studied in a variety of fields due to their diverse impact. The reversible binding of gases can lead to altered optical or electronic properties of the molecules anchored on the surface enabling their application in gas sensors. [14, 15, 174, 175] Furthermore, the magnetic properties of adsorbates can be tuned. [176] It is known that porphyrins and phthalocyanines adsorbed on metal surfaces can incorporate a metal ion in their macrocycle. [89, 106–108, 171] If this metal ion has a magnetic moment the ligation of CO, [177, 178] O_2 [179] or NO [178, 180] can change its spin state. This control of magnetic properties on the molecular scale (magnetochemistry) is of great importance for molecular spintronics. [176] Finally, adsorbed molecules are well-defined active sites and their potential to heterogeneously catalyze chemical reactions is explored for a wide range of different systems, [181, 182] where the underlying substrate strongly influences the reactivity of the adsorbates. [36, 183, 184]

Motivated by the relevance in many biological systems, [11] the interaction of porphyrins containing an Fe center with molecular oxygen is studied. In hemoglobin Fe-porphyrins reversibly bind oxygen and CO_2; under high oxygen pressure in the lungs the Fe centers cooperatively bind oxygen and it is released *e.g.* to the protein myoglobin in muscle tissue. Hemoglobin can also bind CO which is favored over O_2 binding by a factor of 200 and that is why CO is very toxic for humans. [185] However, as mentioned above, the binding affinity of metal centers in porphyrins highly depends on their chemical environment. [36, 184] Another example for this finding is the adsorption geometry of CO on Fe-TPP molecules on a Ag(111) surface. Seufert *et al.* reported the ligation of two CO molecules per Fe-TPP that each bridge a bond of the Fe ion with the macrocycle. [35] Here, the ligation of O_2 on Fe-TPP is studied under similar conditions in order to determine the adsorption geometry and the difference in binding affinity of the Fe center to both gas molecules.

In the second part, another surface-induced change in reactivity of a metal center in a porphyrin is reported. Recently, it was found that Ru-TPP, which is observed to cleave O_2 in solution, [186] is not reactive to oxygen if adsorbed on a Ag(111) surface. [36] Thus, the interaction of the molecule with the surface significantly reduces the reactivity towards O_2. On the other hand, Ti-TPP is expected to be less reactive than Ru-TPP. [36, 187] However, immobilized on the Ag(111) surface Ti-TPP is observed to cleave molecular oxygen and Oxo-Ti-TPP is formed. The topographic contrast and the spectroscopic differences between Ti-TPP and the oxidized species will be described.

6.1   Metalation of 2H-TPP with Iron

The metal center in Fe-porphyrins is very sensitive towards oxidation which is why the compound is difficult to handle under ambient conditions. Therefore, free-base porphyrins are metalated with Fe in a clean environment (UHV). Buchner *et al.* showed that the incorporation of an Fe ion into the macrocycle of 2H-TPP molecules can be achieved by either exposing a porphyrin layer to Fe or by deposition of Fe prior to the evaporation of the molecules. [107] The resulting Fe-TPP molecules are characterized in detail in refs. [89, 107, 188].
In the following, the metalation of 2H-TPP with Fe is described for both the Ag(111) surface and for a boron nitride (BN) layer grown on Cu(111).

6.1.1   Metalation on the Ag(111) surface

In order to metalate 2H-TPP molecules with Fe on the Ag(111) surface, 2H-TPP are deposited for approximately $3\,\mathrm{min}$ ($T_{cru} = 600\,\mathrm{K}$, $T_S = 300\,\mathrm{K}$) which results in a submonolayer coverage of dense-packed islands of molecules. Subsequently, Fe is evaporated from an electron beam evaporator (see ch. 2.1.4) and the sample is annealed at $370\,\mathrm{K}$ for $5\,\mathrm{min}$. The percentage of metalated molecules can be varied by either changing the amount of 2H-TPP on the surface or the evaporation time of Fe.
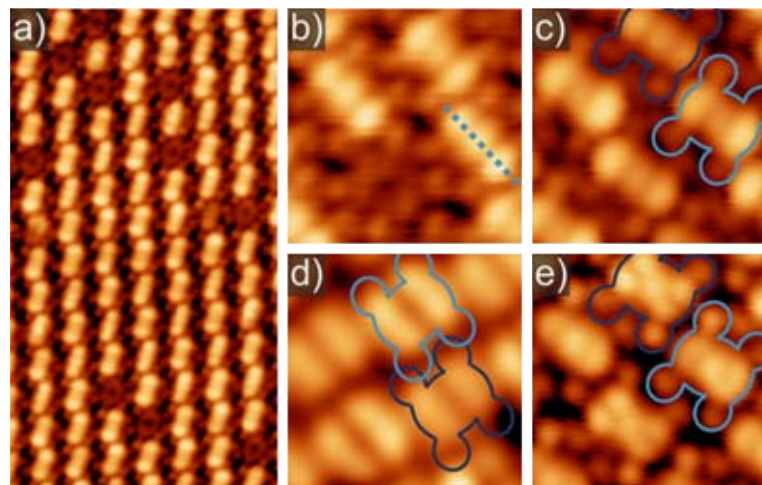
Figure 6.1: *Metalation of 2H-TPP with Fe on Ag(111). a) Overview STM image with a metalation of more than 50%. b-e) Bias-dependent appearance of Fe-TPP (with one 2H-TPP in b). b) -1 V, c) -0.1 V, d) 1.5 V, e) 0.1 V. In b) the main molecular axis is marked by the dotted line. The light and dark blue outlines mark two different Fe-TPP species. [a) 10.3 × 18.3 nm², b-e) 3.4 × 3.4 nm²; a) -0.82 V, 0.1 nA; b) 0.08 nA, c-e) 0.1 nA]*

Figure 6.1a shows a dense-packed island of 2H-TPP and Fe-TPP which is arranged as described in ch. 4.1. At negative sample biases the Fe-TPP appears with three protrusions on the macrocycle, two of which are attributed to the α-pyrrole rings and the central one is induced by the

Fe ion. The axis given by the three protrusions is referred to as the main axis of the molecule (marked by dotted line in fig. 6.1b). Around the macrocycle there are four protrusions marking the phenyl rings. As depicted in fig. 6.1b,c, there are slightly different appearances of Fe-TPP at negative biases. The species marked with a light blue outline exhibits broader and higher protrusions on the two α-pyrrole rings than the dimmer species marked with the dark blue outline. At positive biases close to the Fermi level (up to 0.5 V) the bright blue species shows the same three protrusions with the central one being the highest, whereas for the dark blue species there are two protrusions on the higher pyrrole rings each and one in the center (fig. 6.1e). This appearance changes into two elongated protrusions over the whole molecule at higher positive biases (fig. 6.1d). At these biases the dark blue species appears slightly darker than the bright blue one.

Since the bright and dark blue species only mark the extreme cases and there are several molecules that are intermediates between both species, their occurrence might be due to different adsorption sites on the underlying lattice of the Ag(111) crystal, as the molecules are not commensurate with the substrate. [90] This incommensurability results in a moiré structure of molecules with slightly different appearances.

6.1.2   Metalation on a boron nitride layer

The metalation of 2H-TPP adsorbed on an insulating BN film grown on the Cu(111) surface is observed to be similarly straight-forward as on Ag(111). Firstly, the metal-free 2H-TPP is deposited onto a BN film (growth conditions described in ch. 2.1.4) which results in the formation of dense-packed islands. The molecules arrange in the same way as on Ag(111) with the same lattice constant. In fig. 6.2b an island of 2H-TPP on BN is depicted where the moiré caused by the underlying BN is visible. The lattice mismatch between the BN layer and the Cu(111) surface induces an electronically corrugated interface. Therefore, the molecules within one island are positioned on electronically different adsorption sites leading to different energetic positions of the HOMO and LUMO (see also [189]). Thus, the moiré pattern is visible on the molecular islands if occupied or unoccupied states of the molecules are probed.

As shown in fig. 6.2b the LUMO of 2H-TPP appears as four elongated lobes with a depression in the center (outline of one molecule is marked in green). At small sample biases (within the band gap of the molecule) it appears darker and only the topography is imaged (*e.g.* in fig. 6.2c with green outline). The HOMO was not resolved stably. The energetic positions of the HOMO and LUMO are determined via STS. In fig. 6.3b two main peaks are visible in the spectrum acquired on a 2H-TPP, with the onset of the HOMO around -1.8 V and the onset of the LUMO around 1.5 V. As mentioned above, these values can shift up to several 100 mV depending on the lateral position of the respective molecule on the BN moiré. The average band gap, determined from measurements on several molecules, amounts to 3.4 ± 0.1 V. This value is very similar to the electronic band gap of 2H-TPP on graphene of 3.3 V, however, it is significantly larger than on a
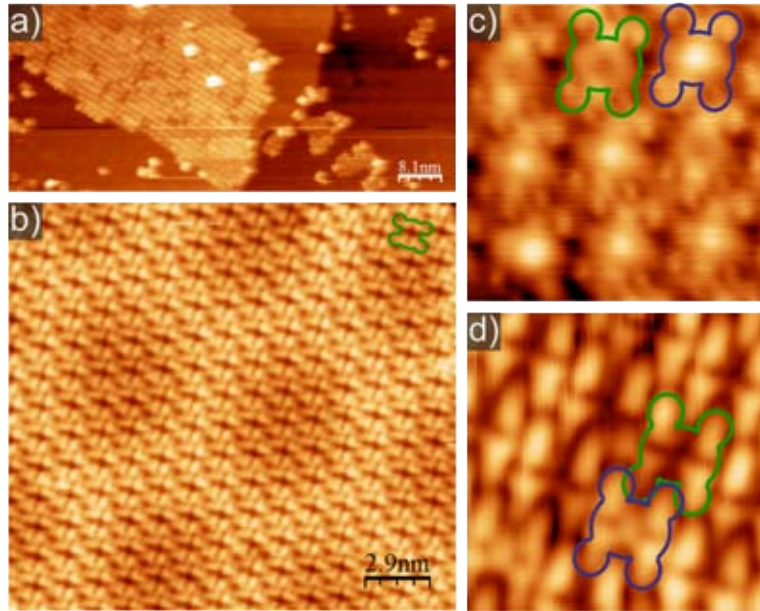
Figure 6.2: *Metalation of 2H-TPP on BN on Cu(111) with Fe. a) STM image of a dense-packed island of 2H-TPP and a few Fe-TPP. b) 2H-TPP island with the moiré of the underlying BN visible. The outline of the LUMO of one 2H-TPP is marked in green. c) 2H-TPP and Fe-TPP (outline in blue) imaged in the band gap. d) LUMO of 2H-TPP and Fe-TPP. [a) 87.5 × 36.9 nm², b) 21.2 × 19.2 nm², c,d) 4.6 × 4.6 nm²; a) 1.4 V, 0.08 nA; b) 2.5 V, 0.06 nA; c) -1.5 V, 0.06 nA; d) 1.7 V, 0.03 nA]*

Au(111) substrate (2.4 V). [190] Gas phase calculations yield an electronic band gap of 4.39 and 4.71 V for 2H-TPP. [191, 192] Due to the strong interaction of molecules with metal substrates their band gaps are reduced upon adsorption. Therefore, the interaction with an insulating layer as BN or graphene seems to be smaller (see also ch. 7.3).

The spectrum on the bare BN film (fig. 6.3a) shows the expected field emission resonances. [71]

In a next step, iron is deposited onto the sample from a filament in the OMBE ($I = 4.4$ A, $V = 2.8$ V, $T_S = 330$ K, $t_d = 10$ min). In large-scale images no difference to the 2H-TPP sample is apparent (see fig. 6.2a). However, in high-resolution images it is obvious that the center of the molecule appears as a protrusion for some of the molecules which is attributed to an Fe ion incorporated into the macrocycle. At negative biases, within the band gap of the molecules, 2H-TPP and Fe-TPP molecules can be clearly distinguished (fig. 6.2c). The LUMO of Fe-TPP is very similar to the one of 2H-TPP except for the additional protrusion in the center of the Fe-TPP and its lower onset voltage (similar to another porphyrin metalated with Co [193]). The energetic shift of the electronic states depending on the position on the moiré is also observed for the Fe-TPP (fig. 6.3c).

In fig. 6.4 the energetic shift of the LUMO between neighboring molecules is illustrated. At 1 V sample bias nearly all molecules appear dark and only two Fe-TPP molecules on the left exhibit
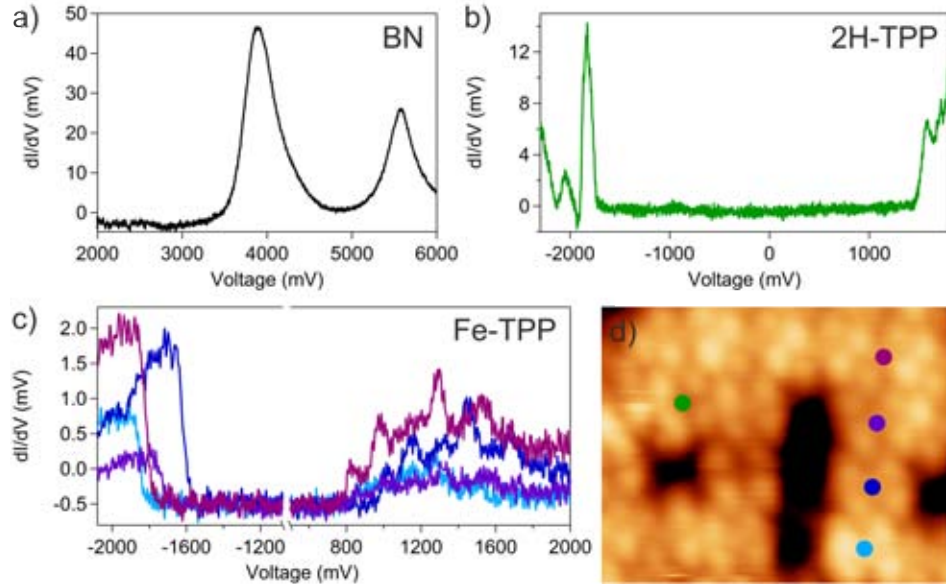
Figure 6.3: *Scanning tunneling spectroscopy on 2H-TPP and Fe-TPP on BN: dI/dV spectra on a) BN on Cu(111) showing the field emission resonances, b) 2H-TPP on BN and c) Fe-TPP on BN. For both 2H-TPP and Fe-TPP the onset of the occupied and unoccupied states varies with the adsorption site. d) STM image showing the positions where the spectra are recorded (marked by colored circles). The dark areas are 2H-TPP molecules with a smaller apparent height. [7.5 × 5.9 nm^2; 1.7 V; 0.04 nA]*
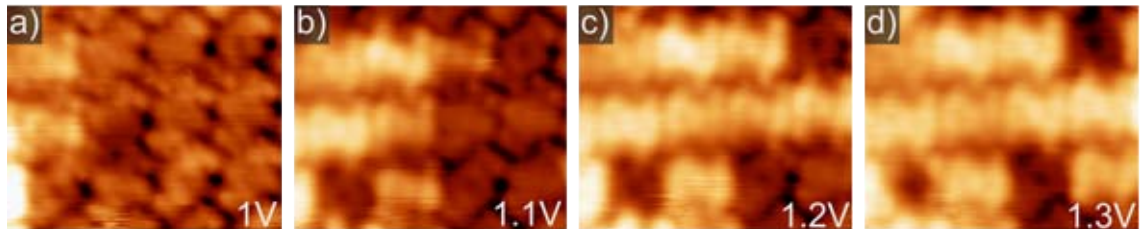
Figure 6.4: *Fe-TPP and 2H-TPP on BN on Cu(111). Onset of the LUMO of the Fe-TPP molecules at different biases depending on the adsorption site. [6.1 × 5.0 nm^2; 0.03 nA; a) 1 V, b) 1.1 V, c) 1.2 V, d) 1.3 V]*

the shape of the LUMO. With increasing sample bias more molecules appear with a greater apparent height and at 1.3 V only the 2H-TPP molecules appear dark since their LUMO lies at a higher energy.

In analogy to the Co case, [193] these data show a successful metalation of 2H-TPP on BN. Importantly, this is the first demonstration of an in-situ Fe metalation of tetrapyrroles on a non-metallic substrate.

6.2   Interaction of Fe-TPP on Ag(111) with CO and O_2

As described in refs. [35, 194] the exposure of Co-TPP and Fe-TPP on a Ag(111) surface to CO, if the sample is cooled to approximately $10\,K$, results in a specific binding of CO on the TPP. In contrast to similar systems as *e.g.* metal-phthalocyanines (Pc) a new adsorption geometry was found. For different surface-anchored metal-Pcs a single CO molecule can bind to the metal center with its axis perpendicular to the surface, [177, 178] whereas for Co-TPP and Fe-TPP the ligation of two CO molecules per TPP is observed. In the STM images the decorated Fe-TPP appears cross-like with two additional protrusions on the axis perpendicular to the main axis (secondary axis). The configuration depicted in fig. 6.5a is assigned to the ligation of two CO molecules that bridge the bond between the iminic nitrogen atoms to the Fe ion. The two CO-related protrusions on the molecule in fig. 6.5b appear noisy and are attributed to only one CO molecule switching between the two possible binding sites. Since the switching rate is higher than the scanning speed of the STM the two protrusions are imaged noisy.
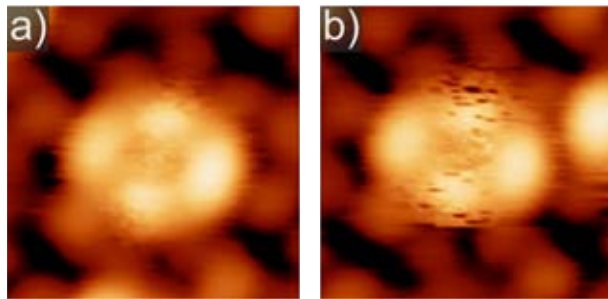
Figure 6.5: a) $(CO)_2$/Fe-TPP and b) CO/Fe-TPP on Ag(111). [$2.2 \times 2.2\,nm^2$; -0.5 V, 0.1 nA]

Additionally, a minority Fe-TPP species is observed after the dosage of CO. In fig. 6.6a an island of 2H-TPP and Fe-TPP is shown with one $(CO)_2$/Fe-TPP (marked by green circle) and several molecules with a bright protrusion in the center and a significantly smaller apparent height of the macrocycle than the majority Fe-TPP (marked by gray circle). These molecules are modified Fe-TPP molecules as shown in fig. 6.6b where some of them turn into Fe-TPP or CO-decorated Fe-TPP during scanning with the STM tip. The appearance of the center of these molecules depends on the tip termination and can either be a protrusion (in fig. 6.6c) or it can be of the same apparent height as the macrocycle (in fig. 6.6d). The images in fig. 6.6c and d were acquired on the same area with the only difference that the tip termination changed between both images. Figures 6.6e and f show the same location on the surface as well, where a minority Fe-TPP species changes to an Fe-TPP between the acquisition of the images.

As this minority species only appears after dosing CO and as shown in fig. 6.6 it can turn into a Fe-TPP or CO-decorated Fe-TPP and the other way around, it is tentatively assigned to a
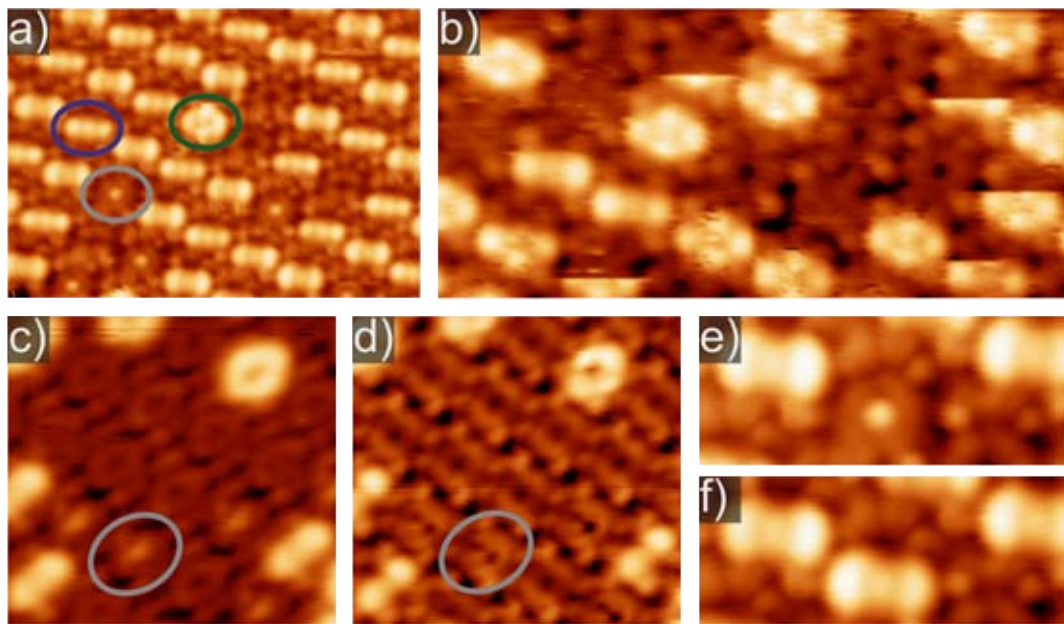
Figure 6.6: *Minority species after CO dosage onto Fe-TPP on Ag(111). a) Overview STM image with (CO)$_2$/Fe-TPP (green circle), Fe-TPP (blue circle) and minority species (gray circle). b) (CO)$_2$/Fe-TPP and Fe-TPP turn into minority species during scanning. c,d) Same area scanned with different tip termination. In c) the minority species appear with a protrusion in the center and in d) with a depression. e,f) The minority species molecule (e) turns into an Fe-TPP (f). [a) 11.2 × 7.9 nm^2; b) 10.1 × 4.6 nm^2; c,d) 5.2 × 4.9 nm^2; e,f) 4.3 × 1.7 nm^2; a,e,f) -0.3 V, 0.09 nA, b) -0.4 V, 0.1 nA, c,d) -0.3 V, 0.07 nA]*

reversible attachment of a ligand.

In order to study the interaction of Fe-TPP on Ag(111) with the biologically relevant molecule O$_2$, it is dosed via a leak valve onto the sample held between 10 to 20 K (p: $1.0 \cdot 10^{-7}$ mbar, $t = 30$ s). Because of the low sticking probability of CO on Fe-TPP at elevated temperatures, [35] O$_2$ is dosed under cold conditions as well. This leads to a decoration of nearly all Fe-TPP molecules on the surface (see fig. 6.7a). The decorated molecules appear very similar to CO-ligated Fe-TPP (cross shape). Also similar to the adsorption of CO is the fact that the O$_2$ molecules are easily moved by the STM tip. In fig. 6.7b abrupt changes in neighboring scan lines indicate a modified appearance of the molecules during scanning.

Due to the similar geometry to (CO)$_2$/Fe-TPP, also for O$_2$ on Fe-TPP it is assumed that two gas molecules bind to the macrocycle bridging the bond between the iminic nitrogen atom and the Fe ion. Moreover, the switching configuration described above (only one gas molecule adsorbed) is observed for O$_2$ on Fe-TPP as well (fig. 6.7d). To sum up, both gas molecules adsorb in similar geometries (one or two gas molecules per Fe-TPP) on Fe-TPP/Ag(111).

Importantly, in the STM data it can be distinguished if the Fe-TPP is decorated with either CO or O$_2$. In the case of O$_2$ on Fe-TPP four additional protrusions are present on the secondary axis of the molecule (fig. 6.7c) which are imaged as only two protrusions with broader tips (fig. 6.7a).
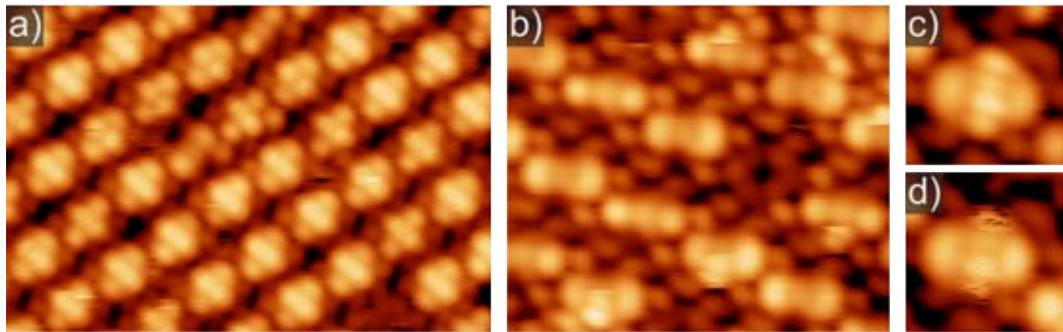
Figure 6.7: *Molecular oxygen (O_2) on Fe-TPP on Ag(111). a) Nearly all Fe-TPP molecules are decorated after dosing O_2 for 30 s at $1 \cdot 10^{-7}$ mbar. The molecules appear very similar to $(CO)_2$/Fe-TPP (cross-shape). b) Scanning over the decorated molecules with the STM tip induces detachment and movement of the gas molecules. c) Stable configuration of Fe-TPP decorated with O_2 and d) labile configuration (imaged noisy). [a) 10.8 × 7.4 nm^2; b) 5.9 × 5.1 nm^2; c,d) 1.8 × 1.8 nm^2; a) -0.4 V, 0.06 nA, b) -0.8 V, 0.1 nA, c) -0.4 V, 0.05 nA, d) -0.4 V, 0.07 nA]*

In contrast, for CO on Fe-TPP only two protrusions appear on the secondary axis (fig. 6.5). A more quantitative discrimination between CO and O_2 adsorbed on Fe-TPP is the distance between the additional protrusions on the secondary axis. For $(O_2)_2$/Fe-TPP the separation of the two inner and the two outer protrusions is measured each for several molecules and compared to the separation of the two protrusions on $(CO)_2$/Fe-TPP in fig. 6.8. With these two protrusions being significantly closer to each other than the outer ones of the $(O_2)_2$/Fe-TPP it can be differentiated which gas molecules are ligated to an Fe-TPP.
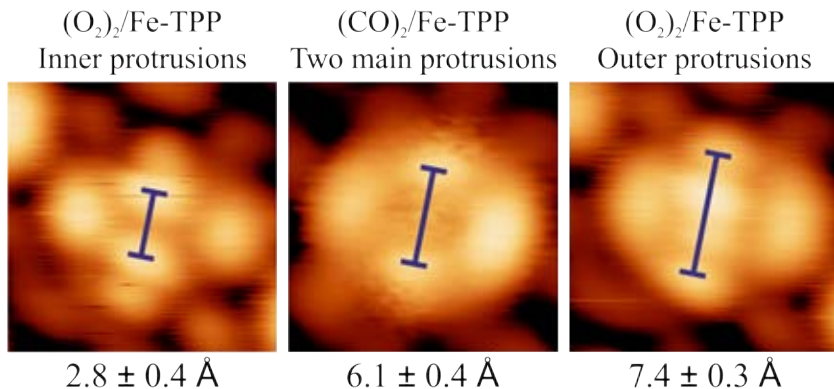
Figure 6.8: *Distance between additional protrusions on Fe-TPP attributed to the adsorption of CO and O_2. For $(O_2)_2$/Fe-TPP four additional protrusions appear and for $(CO)_2$/Fe-TPP only two. Their spacings (marked by blue line) are significantly different from each other so that it can be distinguished in the STM images with which gas molecules the Fe-TPP interacts. [1.5 × 1.5 nm^2; -0.5 V; 0.05 nA, 0.1 nA, 0.05 nA]*

As described above, the Fe-TPP appears in slightly different configurations, referred to as bright and dark species. The difference between these two is still visible with two oxygen molecules ligated to the Fe-TPP. For the bright Fe-TPP species the two protrusions at the center of the

molecule are very close (on the left in fig. 6.9a), whereas for the dark Fe-TPP species they are clearly separated (on the right in fig. 6.9a). The height profile over the secondary axis of both molecules reveals the slight differences between the bright and the dark Fe-TPP species. The shape of the protrusions on the dark Fe-TPP species (dark red line) is symmetric towards the center and all four protrusions appear slightly lower than for the bright Fe-TPP which shows asymmetric peak heights towards the center (bright red line).
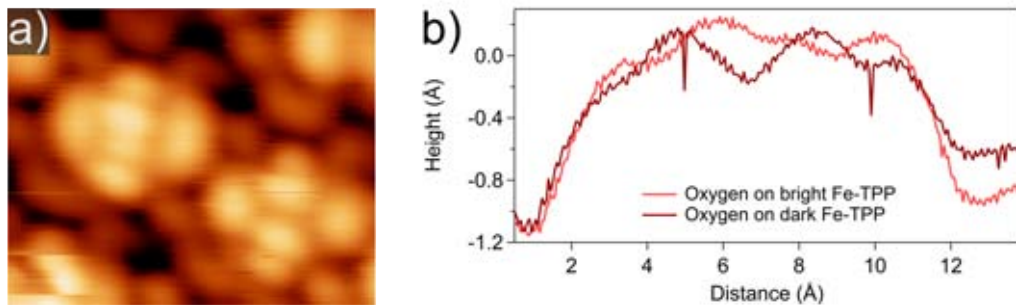
Figure 6.9: *Two different appearances of oxygen on Fe-TPP: a) Oxygen adsorbed on the bright (left) and dark (right) Fe-TPP species. b) Height profiles along the axis perpendicular to the main axis of the molecules on both Fe-TPP species decorated with oxygen. The bright species appears asymmetric in height in the center. [2.9 × 2.4 nm^2; -0.5 V, 0.05 nA]*

The STM images shown in fig. 6.10 were acquired after dosing O$_2$ and CO onto the cold sample. $(CO)_2$/Fe-TPP is marked by a green circle in fig. 6.10a and the two different $(O_2)_2$/Fe-TPP species by a light and a dark red circle each. During scanning over the surface with the STM tip the gas molecules are moved and they can also be exchanged between molecules. In fig. 6.10b and c several $(O_2)_2$/Fe-TPP and one CO-decorated Fe-TPP are depicted. Their appearance only changes marginally when the bias voltage is reversed.

In conclusion, O$_2$ adsorbs in a similar way as CO on Fe-TPP/Ag(111) and by their appearance in STM images $(O_2)_2$/Fe-TPP and $(CO)_2$/Fe-TPP can be differentiated.

The binding of CO and O$_2$ to Fe-TPP adsorbed on a Ag(111) surface is very different from the situation in the protein hemoglobin which reversibly binds oxygen in our body. The four Fe-porphyrin centers in hemoglobin only bind one gas molecule each. [185, 195, 196] Furthermore, in hemoglobin the binding of CO is favored by a factor of 200 over the binding of O$_2$. [185] However, the affinity of Fe-TPP adsorbed on Ag(111) towards the binding of either CO or O$_2$ is very similar. The amount of dosed gas molecules and subsequently ligated porphyrins was similar in both cases. Moreover, temperature-programmed desorption experiments show that both, CO and O$_2$, desorb from Fe-TPP at a temperature of 30 K [197] pointing to a very small but similar binding energy.

In hemoglobin the Fe center of the porphyrin binds to the four nitrogen atoms of the macrocycle,
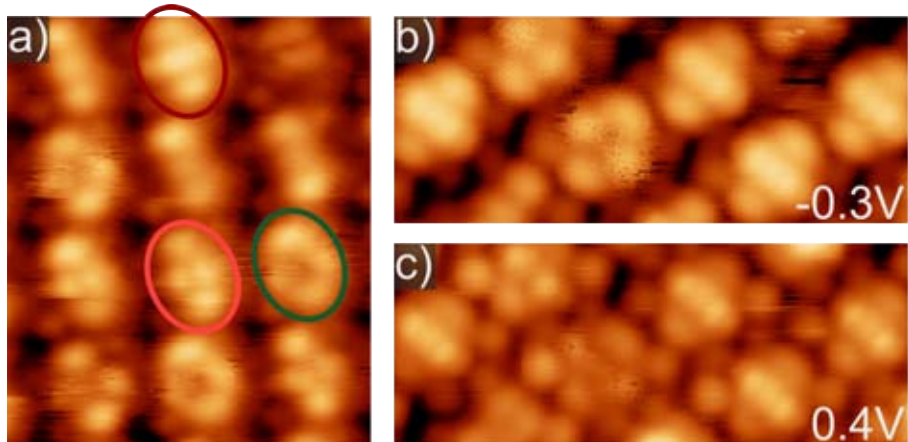
Figure 6.10: *Dosing CO and O_2 on Fe-TPP on Ag(111) yields $(CO)_2$/Fe-TPP (green circle), and O_2 adsorbed on the bright (marked by light red circle) and the dark (marked by dark red circle) Fe-TPP species. The decorated molecules exhibit similar appearances at negative (b) and positive (c) sample biases. [a) $4.6 \times 5.4\,nm^2$; b) $5.9 \times 2.4\,nm^2$; a) -0.7 V, 0.01 nA, b) -0.3 V, 0.04 nA, c) 0.4 V, 0.04 nA]*

to a histidine residue below the plane of the macrocycle and to the oxygen above. On the Ag(111) surface, the interaction of the Fe with the surface differs from the interaction with the histidine, probably lowering the binding energy of oxygen. Due to the observation of strong interactions and charge transfer between metal centers in porphyrins and the underlying metal surfaces, [107, 184, 198] it is likely that the Fe center interacts stronger with the Ag substrate than with the histidine in hemoglobin changing the reactivity towards adsorbates. Moreover, in the protein the oxygen molecule is substantially stabilized by hydrogen bonds to other ligands above the macrocycle which is not the case on the surface. [185] Therefore, the binding energy of O_2 to the Fe center in the porphyrin molecule is reduced in the model system on the surface in comparison to hemoglobin.

In order to reduce the strong interaction of the Fe center with the substrate such that the Fe-oxygen bond becomes stronger, a less reactive surface could be employed, as *e.g.* an insulating BN film on top of a metal surface. Preliminary experiments point to a very weak interaction of Fe-TPP/BN/Cu(111) with molecular oxygen, however, only a few molecules could be resolved. Therefore, the results need to be confirmed for a larger number of molecules.

6.3   Interaction of Ti-TPP on Ag(111) with O_2

Another approach to increase the interaction of O_2 with a surface-anchored metalloporphyrin is to change the metal center. In the following, Ti will be addressed instead of Fe.

The oxidation of Ti-TPP immobilized on the Ag(111) surface is believed to be of great importance for photocatalysis. In 1972 is was found that TiO_2 can photocatalytically split water, [199] however the efficiency is very low because only a small fraction of the sunlight is absorbed and a

thermodynamically favored backwards reaction produces water again. This backwards reaction is predicted to be suppressed for the compound Oxo-Ti-porphyrin. [200] Indeed, Morawski *et al.* observed that microcrystalline TiO-TPP can split water. [201] Therefore, TiO-TPP molecules are prepared and characterized under controlled conditions in UHV in order to gain a fundamental understanding of the system for its future applications.

6.3.1   Metalation of 2H-TPP with Titanium

As described above, the metalation of 2H-TPP molecules on the Ag(111) surface is straightforward for many different metals. [89,106–108] Here, a submonolayer of 2H-TPP ($T_{cru} = 600$ K, $T_S = 310$ K, $t_d = 5$ - 7 min) is metalated with Ti by the deposition of 0.02 nm of Ti from a ribbon evaporator (monitored by a quartz microbalance) followed by annealing at 500 K for 10 min in order to facilitate the metalation. This procedure results in islands of molecules with different contrast (fig. 6.11a) and a few partially flattened 2H-TPP (*cf.* ch. 4.1). Approximately 62 % of the molecules appear with a protrusion in the center instead of a depression and two additional protrusions on the α-pyrrole rings. This shape is very similar to the appearance of other metalated porphyrins as Co-TPP and Fe-TPP on Ag(111) (see *e.g.* ch. 6.1.1).
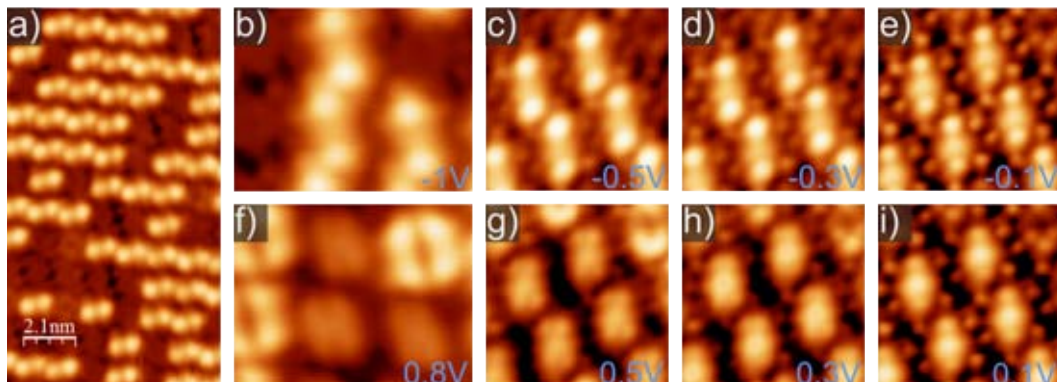
Figure 6.11: *Metalation of 2H-TPP with Ti on Ag(111). a) Dense-packed island of molecules: Ti-TPP appears with three bright lobes and 2H-TPP appears darker. b) to i) Bias-dependent appearance of Ti-TPP. b) -1 V, c) -0.5 V, d) -0.3 V, e) -0.1 V, f) 0.8 V, g) 0.5 V, h) 0.3 V, i) 0.1 V. [a) 9.0 × 15.8 nm^2; b,f) 3.8 × 2.9 nm^2; c-e,g-i) 3.5 × 3.5 nm^2; a,b,f) 0.11 nA, c-e,g-i) 0.2 nA]*

In figure 6.11b-i Ti-TPP molecules are depicted at different sample biases. At -1 to -0.3 V the two protrusions on the pyrrole rings appear brighter than the central protrusion which is related to the HOMO being located on these two pyrrole rings (see below). Close to the Fermi level the three protrusions appear with a similar apparent height. The shape of the LUMO (at 0.3 to 0.5 V) is very similar to the shape of Fe-TPP close to the Fermi level, namely a protrusion in the center and two lobes on each of the α-pyrroles. At higher positive biases Ti-TPP appears with a smaller apparent height than 2H-TPP and exhibits only two elongated lobes (fig. 6.11f).
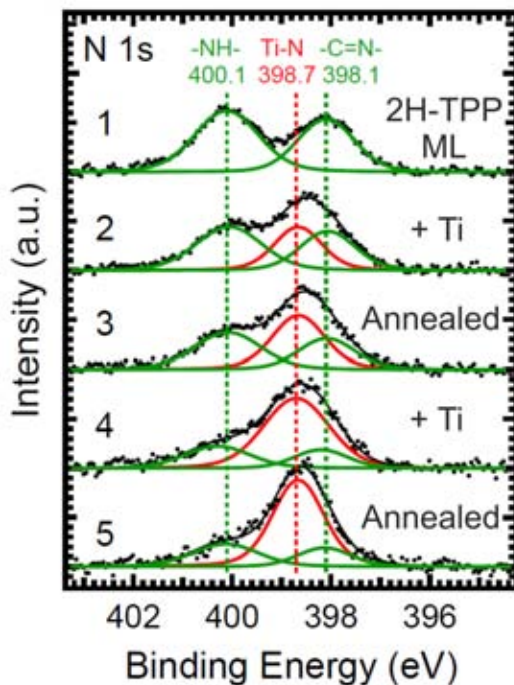
Figure 6.12: *N 1s XP spectra on an increasing amount of 2H-TPP metalated with Ti on Ag(111) (including fits): 1) 2H-TPP ML, 2) 20 % of the Ti saturation coverage (sat. cov.) evaporated onto the 2H-TPP ML at RT, 3) subsequent annealing to 400 K, 4) additional 26 % of the Ti sat. cov. evaporated at RT, 5) annealing to 500 K. Adapted from [202]*

The chemical change of the 2H-TPP molecules is studied as well via XPS (under the supervision of David A. Duncan, see ref. [202]). In the case of only 2H-TPP on the surface the N 1s spectrum shows two peaks (fig. 6.12 top spectrum), one corresponding to the iminic and the other one to the pyrrolic nitrogen atoms. With an increasing amount of Ti evaporated onto the surface and annealing steps another nitrogen-related peak appears which is dominant after the deposition of enough Ti to metalate half a monolayer of 2H-TPP (fig. 6.12 bottom spectrum). Thus, the four nitrogen atoms are chemically equivalent because of the incorporation of the Ti ion into the macrocycle.

The electronic structure of Ti-TPP on Ag(111) is probed via STS. As depicted in fig. 6.13a the HOMO is located around -0.25 V and it is more pronounced on the α-pyrrole rings than on the Ti ion. This finding is in good agreement with the shape of the HOMO on Ti-TPP shown in the dI/dV map recorded at -0.3 V (fig. 6.13b). Very similar to Co-TPP and Fe-TPP the HOMO is located on the two α-pyrrole rings.

The first peak in the unoccupied range is around 0.23 V which is reflected in the STM images by the appearance of two lobes on each α-pyrrole ring.

In conclusion, with the combination of the different techniques it is shown that 2H-TPP molecules can be metalated with Ti on the Ag(111) surface.
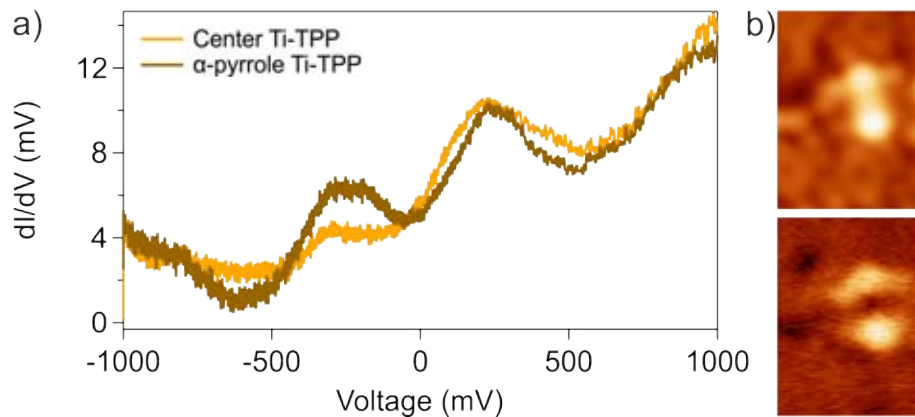
Figure 6.13: *Scanning tunneling spectroscopy on Ti-TPP on Ag(111). a) Two spectra recorded on the center of the molecule and on the α-pyrrole, respectively. The HOMO at -0.25 V is more pronounced on the α-pyrrole and the LUMO is located around 0.23 V. b) Topography image and dI/dV map at -0.3 V: The HOMO consists of two lobes on the α-pyrroles. [b) 2.7 × 3.8 nm^2; 0.15 nA]*

6.3.2   Oxidation of Ti-porphyrins

In order to monitor the oxidation of Ti-TPP on Ag(111), XPS and NEXAFS were recorded after dosing O$_2$ onto the sample held at RT. [202] The peak in the Ti 2p XP spectrum is shifted towards a higher binding energy which points to a change of the oxidation state of the Ti from 2+ to 3+ and thus to an oxidation. Since the N 1s peak remains unchanged it can be assumed that the oxidized Ti is still incorporated in the macrocycle. Furthermore, the oxygen K edge NEXAFS indicates that the Ti-O bond is perpendicular to the surface, *i.e.* that the oxygen either points away from the surface or it is below the Ti and points towards the surface. Annealing experiments indicated that the Ti-O bond is stable up to 725 K.

In the STM experiments the preparation chamber is backfilled with O$_2$ to a pressure of $1 \cdot 10^{-7}$ mbar for 16 min while the sample is kept at RT. After subsequent cooling several different species are observed. Nearly 50 % of all molecules are identified as 2H-TPP and only a small amount of approximately 6 % appears as Ti-TPP. As the metalation efficiency is known from the previous experiments, it is expected that at least 50 % of the molecules are metalated. Thus, all other molecules than 2H-TPP are assigned to Ti-TPP interacting with oxygen.

As depicted in fig. 6.14 three main different species are observed apart from Ti-TPP, 2H-TPP and a few additional minority species that could not be identified. All three species shown in fig. 6.14 appear very similar to 2H-TPP except for the center of the molecules. The majority species (fig. 6.14a) exhibits a slit in the center of the molecule at negative sample biases and at positive biases it appears as two elongated lobes where the 2H-TPP shows four lobes. The second species depicted in fig. 6.14b has the same apparent height in the center of the molecule as on the macrocycle at negative biases and the third species has a protrusion in the center (fig. 6.14c). At positive biases these two species appear with four lobes on the macrocycle that
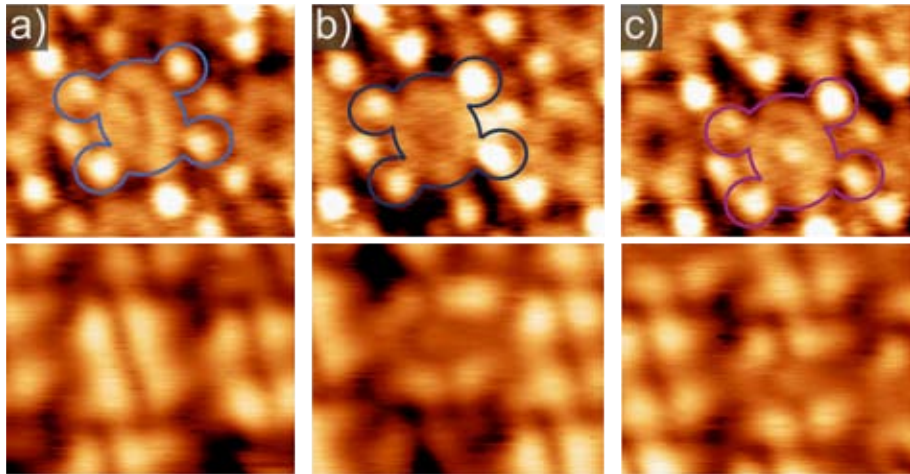
Figure 6.14: *Three Ti-TPP species observed after dosing O_2 imaged at negative (top) and positive (bottom) sample biases. a) Majority species with a slit in the center of the macrocycle (outline marked in blue). b) Minority species with the center at the same apparent height as the macrocycle (outline marked in dark blue). c) Minority species with a protrusion in the center (outline marked in violet). [$3.1 \times 2.5\,nm^2$; top panels: -0.3 V, bottom panels: 1 V; 0.12 nA]*

are very similar to the LUMO of 2H-TPP and with a protrusion in the center which is brighter for the third species.

Based on the XPS and NEXFAS measurements, [202] it is deduced that the molecular oxygen is cleaved on the surface and that only one oxygen atom binds to the Ti ion in the molecules. Thus, oxotitanium-TPP (TiO-TPP) is formed and the occurrence of only one TiO-TPP species is expected. However, approximately 30 % of the molecules appear as the first TiO-TPP species, referred to as blue TiO-TPP (marked in fig. 6.14a), only 4 % as the dark blue TiO-TPP (fig. 6.14b) and 8 % as the violet TiO-TPP (fig. 6.14c). The identification of all different species is based on STM images acquired at positive and negative biases at the same spot on the surface using the same tip. The corresponding statistics are given in tab. 7.

Molecule	Occurrence
2H-TPP	$46 \pm 4\,\%$
Ti-TPP	$6 \pm 1\,\%$
Blue TiO-TPP	$30 \pm 3\,\%$
Dark blue TiO-TPP	$4 \pm 1\,\%$
Violet TiO-TPP	$8 \pm 2\,\%$
Other	$7 \pm 1\,\%$

Table 7: *Occurrence of different species after dosing O_2 onto 2H-TPP and Ti-TPP on Ag(111).*

In contrast to the interaction of Fe-TPP with CO and O_2, no tip-induced movement of adsorbates is observed for the TiO-TPP. Nevertheless, some of the molecules can undergo tip-induced

changes in appearance. Figure 6.15a to c shows the same area on the surface and between the acquisition of the images ST spectra were recorded in the bias range of -1 to 1.2 V. Firstly, the 2H-TPP molecule marked by the green circle in fig. 6.15a tautomerizes during STS and the other tautomer is depicted in fig. 6.15b. Secondly, the circled blue TiO-TPP turns into a dark blue TiO-TPP in fig. 6.15b and back into a blue one (fig. 6.15c) after a voltage pulse of -2 V in close proximity.
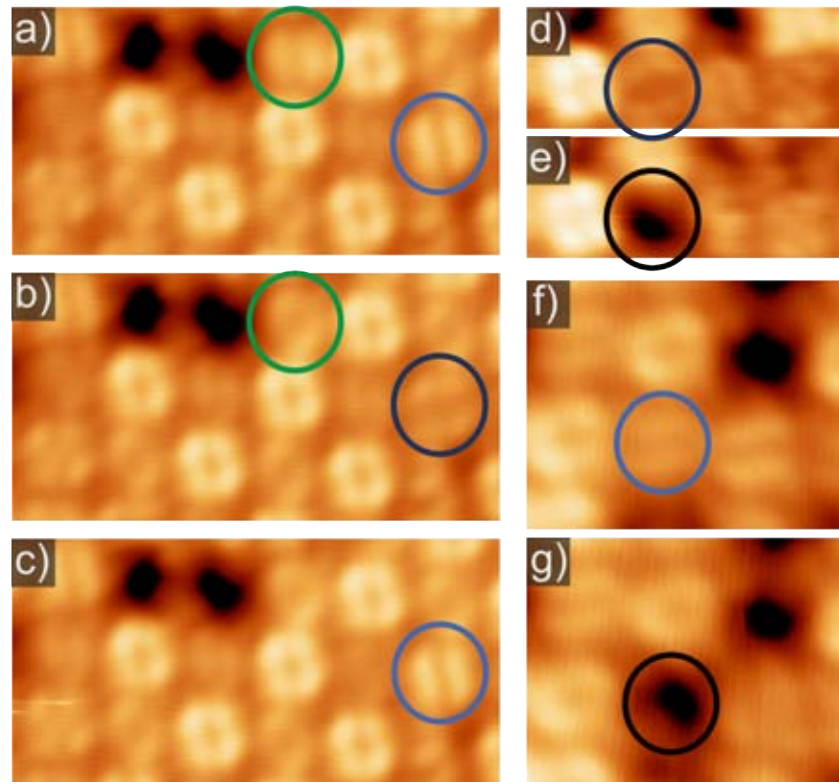
Figure 6.15: *Tip-induced change of appearance of different TiO-TPP species. a) to b) 2H-TPP (green) tautomerizes and the blue TiO-TPP turns into a dark blue TiO-TPP. b) to c) The dark blue TiO-TPP turns back into a blue TiO-TPP. The tautomerization occurs during STS on the 2H-TPP and the switching of the TiO-TPPs takes place during STS on other molecules close by. d) to e) A dark blue TiO-TPP turns into a dark species during STS in close proximity. f) to g) A blue TiO-TPP turns into a dark species during STS on the molecule. [a-c) 9.3 × 4.8 nm^2; d,e) 5.4 × 2.1 nm^2; f,g) 3.8 × 4.9 nm^2; a-c,f,g) 0.6 V, d,e) 0.7 V; a) 0.2 nA, b,c) 0.25 nA, d,e) 0.3 nA, f,g) 0.15 nA]*

Furthermore, both the dark blue (fig. 6.15d,e) and the blue TiO-TPP (fig. 6.15f,g) can turn into a dark species with a significantly lower apparent height at different biases. Only at negative biases the four phenyl rings are visible and a protrusion in the center. Between fig. 6.15d,e a ST spectrum between -0.2 to 2 V is recorded and several spectra from -1 to 1.2 V between fig. 6.15f,g. The transformation into the dark species was only once observed to be reversible, but mostly during scanning and especially during STS measurements the amount of dark species increases. At biases above ± 2 V several molecules change at the same time. Thus, the dark species might

be chemically changed or decomposed by the tip.

In summary, the following tip-induced transformations are observed:

Blue TiO-TPP $\rightarrow$ Dark blue TiO-TPP

Dark blue TiO-TPP $\rightarrow$ Blue TiO-TPP

Blue TiO-TPP $\rightarrow$ Dark species

Dark blue TiO-TPP $\rightarrow$ Dark species
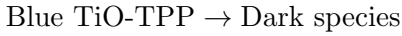
Consequently, the statistics in tab. 7 have to be treated carefully because tip-induced changes cannot be excluded in the STM images. Moreover, the blue and the dark blue TiO-TPP seem to be the same species in two different conformations whereas the violet TiO-TPP is not affected by the tip.

In order to clarify the nature of the different species and to probe the electronic structure of the different species STS are recorded. The spectra on Ti-TPP and 2H-TPP are plotted as a comparison in fig. 6.16a. The blue TiO-TPP shows a peak in the unoccupied range around 0.6 V and a step at 0.1 V, whereas the dark blue and violet TiO-TPP only show the step at 0.1 V and a broad increase towards higher voltages. The overall shape of the ST spectrum is very similar for 2H-TPP and the blue TiO-TPP. Moreover, the energetic position of the LUMO varies for both molecules in a similar range. In fig. 6.16b for both molecules two spectra are plotted for molecules on different adsorption sites. The peak shape is similar in all cases but their energetic position is shifted. The only difference is that the 2H-TPP tautomerizes at higher biases as *e.g.* in the light green spectrum in fig. 6.16b (at 0.8 V).
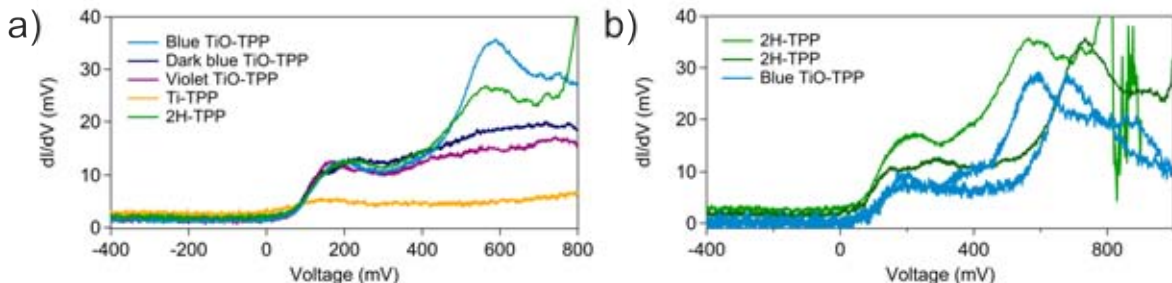
Figure 6.16: *Scanning tunneling spectroscopy on TiO-TPP, Ti-TPP and 2H-TPP on Ag(111). a) The spectra of the blue TiO-TPP and 2H-TPP are very similar, as well as the ones of the dark blue and violet TiO-TPP. All TiO-TPP species are spectroscopically different from Ti-TPP. b) The energetic position of the LUMO depends on the adsorption site for 2H-TPP and the blue TiO-TPP. For each of them two spectra are plotted in order to indicate their possible variations.*

The fact that the spectra of the dark blue and the violet TiO-TPP have the same shape and that their appearance in the STM images is very similar as well points to only minor differences between the two species which might be explained by different adsorption sites. Taking into

account that the tip can induce the reversible transformation from a blue to a dark blue TiO-TPP, all the species might be attributed to TiO-TPP, present in at least three configurations on the surface.

As described above, the spectra on the blue TiO-TPP are very similar to the ones on 2H-TPP but show pronounced differences in comparison to Ti-TPP. This finding can be explained by an altered interaction of the Ti ion with the macrocycle upon oxidation (as observed for NO/Fe-TPP [194]). Since it is not clear if the oxygen atom is above or below the plane of the macrocycle, it is possible that the Ti ion is lifted or lowered from its former position.

6.4 Summary

To conclude, it is shown that the ligation of small gas molecules to metal-porphyrins on a support is strongly influenced by the interaction of the metal ion to the substrate. In the first part, the on-surface metalation of 2H-TPP with Fe on both the Ag(111) surface and an insulating BN layer grown on Cu(111) is described. On the Ag(111) surface, where the interaction of the Fe ion to the substrate is strong in comparison to the BN layer, CO and O_2 can only be ligated to the adsorbed molecules if the sample is cooled to $20\,\mathrm{K}$ or lower. In the case of CO on Fe-TPP/Ag(111) two CO molecules can be adsorbed and they each bridge a bond of the Fe ion to the macrocycle. [35] In a second possible configuration a single CO molecule switches between these two adsorption sites. Due to the similar appearance in STM images it is assumed that O_2 ligates to Fe-TPP/Ag(111) in a similar way as CO. Nevertheless, the structure of the additional protrusions on the Fe-TPP is slightly different for both gases so that they can be distinguished in the STM images.

Temperature-programmed desorption experiments show that both CO and O_2 desorb from Fe-TPP/Ag(111) at $30\,\mathrm{K}$. [197] This low affinity towards the two gas molecules can be explained by a strong interaction of the Fe ion with the substrate (covalent character [184]). Moreover, in hemoglobin it is observed that the position of the Fe ion relative to the plane of the macrocycle (above or below) influences the affinity to the gas molecules as well. [185] Therefore, future experiments could be carried out on a surface with a reduced interaction with the Fe ion as *e.g.* a BN layer grown on Cu(111).

In the second part, 2H-TPP molecules are metalated with Ti on the Ag(111) surface. Subsequent exposure to O_2 leads to the formation of oxo-Ti-TPP which is monitored by XPS and NEXAFS. In the STM observations three new species are identified after oxidation. However, two of them seem to be only different configurations of the same species since they could be reversibly switched by voltage pulses from the tip. Furthermore, the third species is spectroscopically and topographically very similar to one of the two configurations. Thus, the three species might be different configurations of only one TiO-TPP species. For all three of them the tunneling spectra more resemble the ones of 2H-TPP than of Ti-TPP pointing to a change of

the interaction of the Ti ion with the macrocycle upon oxidation.

These findings that Ti-TPP on Ag(111) is oxidized at relatively low exposures to O_2 and that the Ti-O bond is stable up to $725\,K$ fits nicely into a trend in reactivity across the periodic system. Ru-TPP was observed to be unreactive towards O_2 [36] and the Mn-O bond in oxidized Mn-TPP molecules is only stable up to $445\,K$. [203] Hence, Ti being located at an even smaller group number in the periodic system is the most reactive of the three elements. With the observation of this trend future catalysts can be developed with tailored reactivity.

Moreover, the formation of TiO-TPP in this controlled environment enables further investigations on the photocatalytic activity of this system.

7 Intermolecular interactions at the model interface of an organic solar cell

Organic solar cells comprise a variety of advantages in comparison to inorganic photovoltaics because they can be produced at lower cost, with less weight and they exhibit high absorption coefficients. [204] Some organic solar cells are transparent in parts of the visible range of the sunlight enabling *e.g.* an incorporation in windows. [205] One common type of organic solar cell consists of a solution-based bimolecular heterojunction which enables facile processing and the properties of the device can be tuned by employing different molecules. [206, 207]

Here, a model system for a bimolecular organic solar cell is investigated with the molecules B,O-chelated azadipyrromethene (BO-ADPM) and C_{60} forming the heterojunction. In the device C_{60} acts as the electron acceptor and it was shown that C_{60} supports a rapid charge separation, [208] whereas the BO-ADPM molecules exhibit a high absorption coefficient and thus are responsible for the absorption of the incident light and act as the donor in the junction. [72] The absorption of photons leads to the formation of a bound electron-hole pair (exciton) which diffuses to the interface. The drop in potential between both materials causes the dissociation of the exciton and thus the electron is located in the acceptor layer and the hole in the donor layer. Subsequently, both charge carriers are transported separately to the metal contacts. [204, 206]

Hence, at the interface important processes that influence the efficiency of the device take place. In order to optimize the performance of the solar cell it is required to understand which parameters influence its efficiency. Recent studies show that the geometry and the arrangement of the two different molecules at the interface have impact on the exciton dissociation [209] and on the overall efficiency. [210–213] Therefore, in the following a model system of a device which was studied by Leblebici *et al.* [72] is investigated in a controlled and solvent-free environment. The interface of the device is simplified in such a way that one layer of the acceptor (C_{60}) and of the donor (BO-ADPM) molecules are deposited onto a Ag(111) surface acting as the back contact. With the STM tip the junction is contacted from the top. In this configuration the interaction of both molecules at the interface is investigated and the electronic band gap is measured.

7.1 BO-ADPM on Ag(111)

At first, the donor molecule BO-ADPM is studied on the Ag(111) surface in order to compare its appearance and electronic structure to the adsorption on a layer of C_{60}. BO-ADPM exhibits a non-planar conformation in the gas phase. The structural model obtained by Hyper-Chem (AM1 method) shows that for an isolated species the two oxy-phenyl moieties are bent away from each other resulting in an opening angle of approximately 50° (top view in fig. 7.1a and side

view in fig. 7.1b). The two phenyl rings are slightly tilted. Upon deposition onto the Ag(111) surface ($T_{cru} = 490\,\mathrm{K}$, $T_S = 300\,\mathrm{K}$ and $t_d = 23\,\mathrm{min}$) the non-planarity is preserved. As apparent in fig. 7.1c one part of the molecule appears significantly higher than the other parts in the STM image and it is thus assigned to the upwards-bent oxy-phenyl. Since this contrast is present at different biases a geometric effect rather than an electronic one can be assumed.
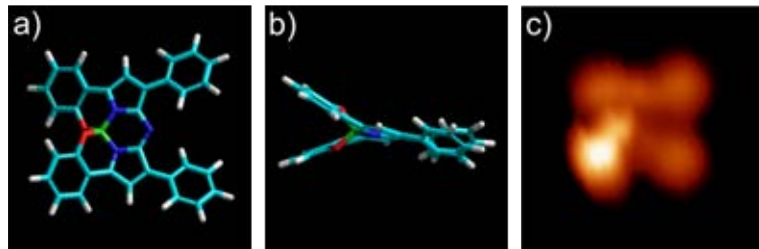
Figure 7.1: *Structural model of BO-ADPM: a) top view and b) side view. N, B and O are indicated in blue, green and red, respectively. c) The bending of the two oxy-phenyl rings is preserved on the Ag(111) surface since one of them appears with a clearly greater apparent height in the STM images. [2.7 × 2.7 nm², 0.5 V, 0.2 nA]*

In a sub-ML coverage the molecules arrange in dimers, trimers and tetramers on the Ag(111) surface (fig. 7.2a). Monomers are observed only rarely. In a dimer the two molecules are stacked in such a way that the upwards pointing oxy-phenyl of one molecule overlaps with the downwards-pointing oxy-phenyl of the other molecule resulting in two protrusions in the center of the dimer (fig. 7.2b). Similarly, a trimer exhibits three protrusions in the center (fig. 7.2c) and a tetramer four (fig. 7.2d).
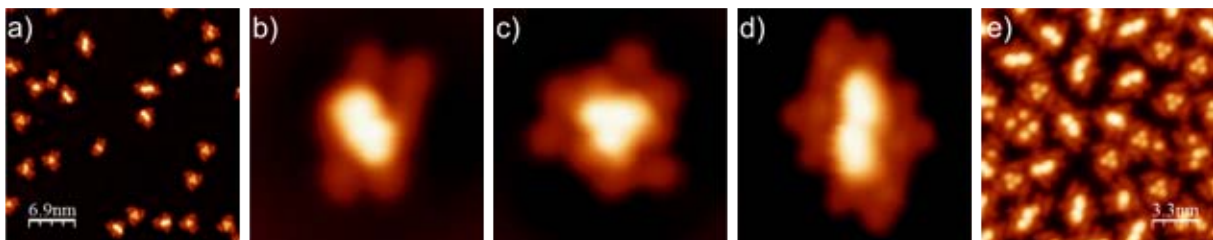
Figure 7.2: *BO-ADPM on Ag(111): a) The molecules arrange as dimers, trimers and tetramers. High resolution images of b) dimer, c) trimer, d) tetramer. e) Higher coverage. [a) 37.3 × 37.3 nm², b,c) 4.0 × 4.0 nm², d) 4.9 × 4.9 nm², e) 17.8 × 17.8 nm²; a,d) -0.4 V, 0.2 nA, b,c) -0.1 V, 0.2 nA, e) -0.3 V, 0.1 nA]*

At a higher coverage the molecules do not assemble in regular islands but still as dimers, trimers and tetramers (fig. 7.2e).

In fig. 7.3 the $\mathrm{d}I/\mathrm{d}V$ spectra are depicted for a BO-ADPM monomer, dimer and trimer. All spectra are acquired on the bright part of the molecules since the other parts only show a featureless increase of the $\mathrm{d}I/\mathrm{d}V$ signal in the unoccupied range. The spectrum on the bare Ag(111) surface is plotted for comparison. All three species exhibit an occupied state around

-0.4 V which is attributed to the HOMO. Furthermore, only the trimer shows a state in the unoccupied range around 0.8 V.
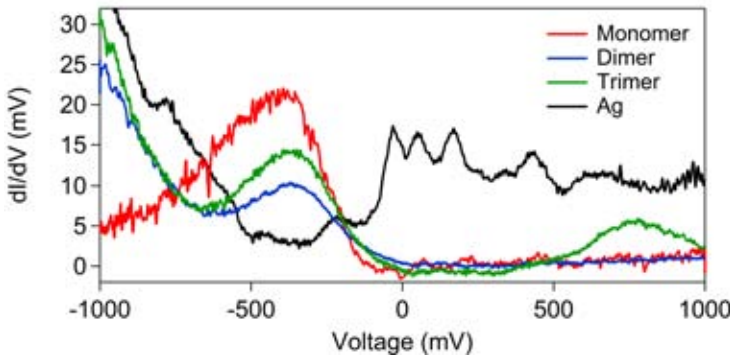
Figure 7.3: *Scanning tunneling spectroscopy on BO-ADPM on Ag(111). The spectra on the different molecules (monomer, dimer and trimer) are recorded on one of the upwards-pointing oxy-phenyl rings.*

7.2 Interaction of BO-ADPM and C$_{60}$

In order to mimic the interface of the bimolecular solar cell, it is required to deposit the donor and the acceptor molecule on top of each other. At first, C$_{60}$ is deposited onto a sub-ML of BO-ADPM ($T_{cru} = 690$ K, $T_S = 320$ K and $t_d = 8$ min) which results in a phase separation of both molecules (fig. 7.4a). C$_{60}$ forms dense-packed islands on the Ag(111) surface (see [214]) and the BO-ADPM molecules are arranged as described above (ch. 7.1) and a few decorate the borders of the C$_{60}$ islands. Annealing the surface to 490 K does not induce any changes. Therefore, in a second approach C$_{60}$ is deposited onto the pristine Ag(111) surface and BO-ADPM is added at sample temperatures between 130 to 150 K. Thus, the BO-ADPM molecules are less mobile and some adsorb on top of the C$_{60}$ islands. If a ML of C$_{60}$ is predeposited the BO-ADPM cannot be imaged stably on top. However, also in the sub-ML case the BO-ADPM on top of C$_{60}$ islands is easily moved by the STM tip during scanning (see fig. 7.4b). Since the phase separation of both molecules seems to be preferred on the Ag(111) surface, at higher temperatures the BO-ADPM has enough energy to move from the C$_{60}$ islands to the metal.

In fig. 7.4c one BO-ADPM molecule on C$_{60}$ is imaged stably. In this case the shape of the molecule is recognizable, however most of the BO-ADPMs are arranged in small agglomerates on C$_{60}$ where it is not clear how the single molecules are arranged (*e.g.* in fig. 7.4b). For the C$_{60}$ molecules the LUMO is imaged in fig. 7.4b,c which appears as three lobes (see [214]).

In a third approach a higher coverage of BO-ADPM is deposited onto the Ag(111) surface (t_d
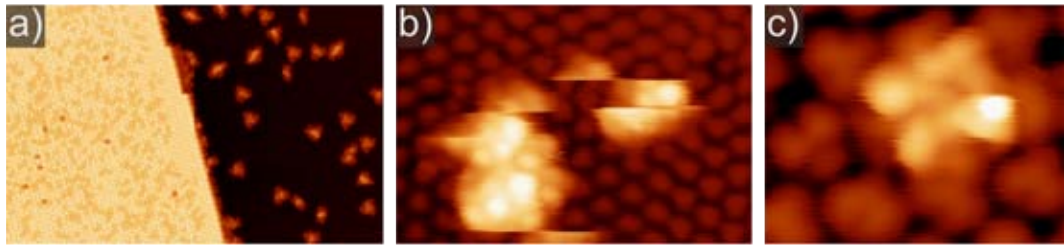
Figure 7.4: *Interaction of BO-ADPM and C_{60} on Ag(111). a) Phase separation of BO-ADPM (left) and C_{60} (right) at sub-ML coverage. b) BO-ADPM adsorbed on a C_{60} island is easily moved by the STM tip. c) BO-ADPM monomer on a C_{60} island, deposited at 150 K. [a) $69.2 \times 43.9\,nm^2$, b) $11.9 \times 8.0\,nm^2$, c) $3.6 \times 2.8\,nm^2$; a) 1.4 V, 0.2 nA, b) 1.4 V, 0.04 nA, c) 0.7 V, 0.08 nA]*

$= 45\,\text{min}$) and C_{60} is deposited on top ($T_S = 200\,\text{K}$, $t_d = 42\,\text{min}$). From the STM images it is not clear whether C_{60} is on top of the BO-ADPM molecules or directly on the Ag. Therefore, lateral manipulation experiments are carried out with the STM tip. By dragging a C_{60} molecule at the edge of an island (0.1 V, 5 nA) it can be moved away from it revealing the surface below its former position (fig. 7.5a to b). When several C_{60} molecules were moved the bare Ag surface is revealed (fig. 7.5c). Consequently, the C_{60} molecules seem to preferentially adsorb directly on the Ag.

Scanning tunneling spectra on C_{60} molecules within the islands and on single ones point to an adsorption on the metal as well. The spectra shown in fig. 7.5d look very similar to spectra acquired on C_{60}/Ag(111) (*cf.* [215]). Thus, the phase separation of the two molecules seems to be preferred also at a higher coverage.
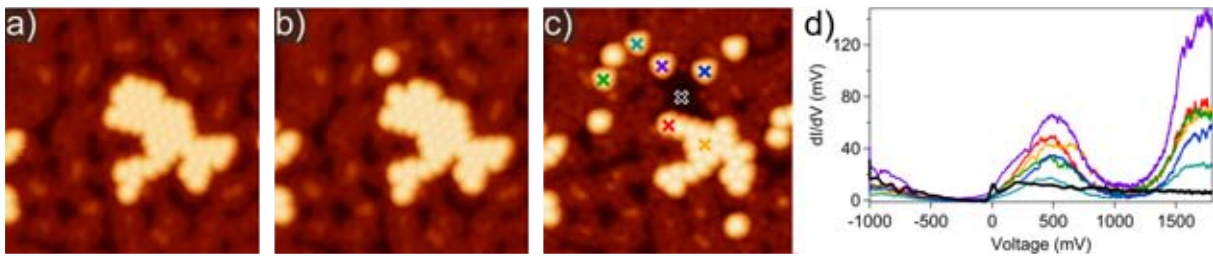
Figure 7.5: *Lateral manipulation of C_{60} deposited onto BO-ADPM. It is not clear if the C_{60} molecules sit on top of BO-ADPM or on the bare metal. a) to b) One C_{60} molecule is moved away from the island with the STM tip (0.1 V, 5 nA). c) Several C_{60} molecules were moved by the tip. d) STS on different C_{60} molecules shows no difference to spectra on C_{60}/Ag(111). [$21.3 \times 22.1\,nm^2$; 0.7 V, 0.1 nA]*

7.3 Measurement of the electronic band gap

An important property of a bimolecular solar cell is the band alignment of both materials at the interface. The energy offset E_{DA} of the HOMO of the donor (BO-ADPM) and the LUMO of the acceptor (C_{60}) influences the efficiency of the power conversion process. [72,210] In the model system this energy offset can be measured by recording the dI/dV spectrum on BO-ADPM/C_{60}/Ag(111). The energetic separation of the highest occupied state and the lowest unoccupied state (electronic band gap) corresponds to the energy offset E_{DA}.

The tunneling spectra are recorded on BO-ADPM agglomerates on C_{60}/Ag(111) after deposition at 130 to 150 K because this is the most stable configuration. The spectra acquired on BO-ADPM/C_{60}/Ag(111) differ significantly from the ones on the bare metal and also from C_{60}/Ag(111). The HOMO and LUMO are mostly measured separately in order to obtain a better signal-to-noise ratio for both peaks. The HOMO is located around -1.7 V and the LUMO around 1 V. Both states, HOMO and LUMO, vary by several 100 mV depending on the adsorption site of the BO-ADPM, thus several spectra are plotted for both states in fig. 7.6.
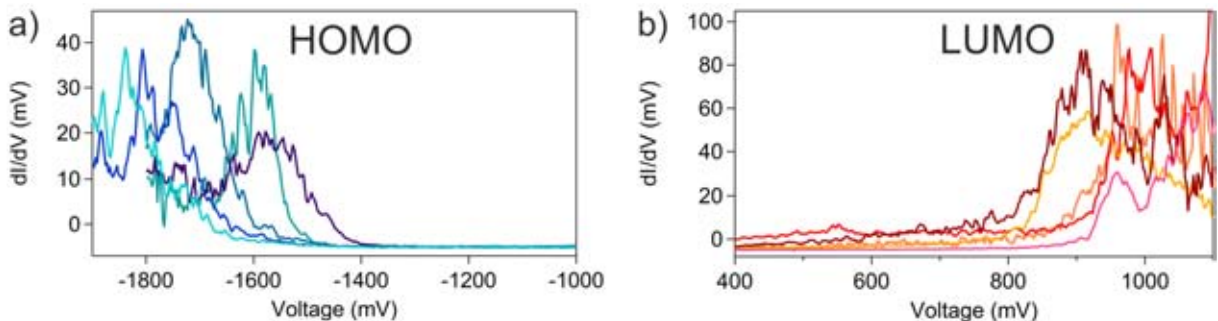
Figure 7.6: *Measurement of the electronic band gap of BO-ADPM/C_{60}/Ag(111). Scanning tunneling spectra in the occupied (a) and unoccupied (b) range for different molecules. For most of the molecules the HOMO and LUMO are measured separately. Both states vary in a range of approximately 300 mV.*

Due to the large variation of the peak position of HOMO and LUMO several spectra were analyzed and average values are obtained. The HOMO is measured 39 times and is on average positioned at -1.69 ± 0.09 V. The average LUMO amounts to 0.97 ± 0.07 V (measured 35 times). All values are plotted in histograms in fig. 7.7. These values give an average band gap of 2.7 ± 0.2 V. As described in ch. 6.1.2 molecules adsorbed on a metal surface strongly interact with it and in most cases the electronic states are shifted closer to each other. In accordance, the spectra on BO-ADPM/C_{60} show a larger band gap than BO-ADPM/Ag(111).

In comparison to the solution-based devices the band gap measured here is slightly larger than estimated for this system in ref. [72]. Hence, a higher conversion efficiency is expected than reported in [72]. However, the observation that a phase separation of the two molecules is pre-
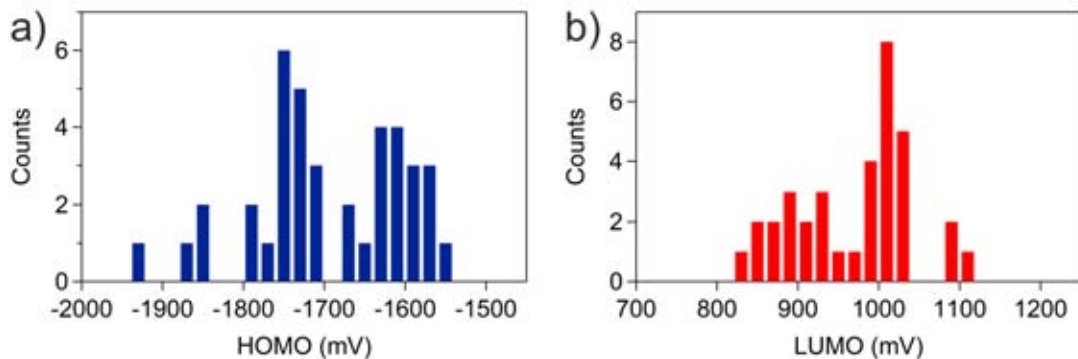
Figure 7.7: *Histograms of the measurement of HOMO (a) and LUMO (b) of BO-ADPM/C_{60}/Ag(111). The HOMO and LUMO could only be measured 39 and 35 times, respectively, because the molecules are easily moved by the STM tip.*

ferred implies a reduced overlap of the orbitals of the different molecules at the interface which can lower the charge transfer efficiency and thus the efficiency of the whole device.

7.4   Summary

In conclusion, a model system for an organic solar cell is investigated revealing a phase separation between the donor and acceptor molecules which is likely to lower the efficiency of the charge transfer and thus the power conversion efficiency of the solar cell.

On the Ag(111) surface the non-planar donor molecule BO-ADPM arranges in dimers, trimers and tetramers with only a few monomers. The tunneling spectra show broad features derived from molecular electronic states interacting with the metal surface.

In order to mimic the interface of the solar cell both molecules are co-deposited onto the Ag(111) surface. However, only the deposition at temperatures below 150 K results in the adsorption of BO-ADPM on C_{60}/Ag(111). At higher temperatures both molecules separate from each other. When adsorbed on a layer of C_{60} the BO-ADPM shows sharper peaks in the tunneling spectra and they are further separated. By acquiring the energetic position of the HOMO and LUMO of several molecules and agglomerates of molecules on C_{60} an average electronic band gap of 2.7 ± 0.2 V is determined.

Although the model system employed here is very simplified since the fabrication is very different from the device described in ref. [72] it points to an inefficient charge transfer at the interface due to the phase separation of the two molecules. In order to study a system more similar to the device structure the BO-ADPM film could be spin-cast or drop-cast onto the sample before transferring it into the UHV environment.

8 Conclusion and perspectives

The structural and electronic properties of versatile molecules are investigated on clean metal surfaces as a well-defined laboratory system. For the first time homocoupling of porphine molecules on a Ag support is reported. The covalent coupling results in an altered electronic structure of the oligomers, *i.e.* a reduced electronic band gap. In contrast, TPP molecules are observed to undergo intramolecular ring-closing reactions. Moreover, the interaction of metallo-porphyrins with gas ligands is studied as well as the interaction of a metallo-phthalocyanine with the underlying substrate. In the end, the intermolecular interactions in a model system of a solar cell device are investigated.

In detail, porphine molecules adsorbed on Ag surfaces are observed to couple covalently when heated on the surface. For free-base porphines two approaches are employed. In the first one the molecules are annealed after the deposition of one ML onto the surface. Since this approach is limited by the considerable desorption rate of 2H-P at the temperature required to induce the dehydrogenation and coupling reactions, the second approach counteracts the desorption by the continuous deposition of molecules while the surface is heated. With this, covalent oligomers consisting of up to 90 units are formed. Similar to porphine tapes synthesized in solution, here a reduction of the band gap is measured for the triply-fused dimer, representing the most abundant binding motif.

Covalent homocoupling is also observed for Co-porphines. Due to the low desorption rate annealing a sub-ML is sufficient to induce the coupling. In contrast to 2H-P, Co-P exhibits a different preferred binding motif. Furthermore, 2H-P oligomers can be metalated with Co which enables to influence the shape of the Co-P-oligomers. In order to achieve a more directed growth of the oligomers, the porphines are substituted with Br atoms at two *meso* positions. At RT deposition Ag-coordinated chains are formed, whereas at higher annealing temperatures the molecules covalently couple, but less efficiently than for 2H-P and the Br as a byproduct remains on the surface. Consequently, the homocoupling of unsubstituted 2H-P is a clean approach to form covalent nanostructures on Ag surfaces with coupling motifs that had only been realized in solution before.

Blocking the four reactive *meso* positions of 2H-P by the attachment of phenyl moieties affords 2H-TPP. For this molecule intramolecular ring-closing reactions are observed on the Ag(111) surface. Upon annealing the phenyl rings react with the macrocycle in such a way that four different planar porphyrin derivatives are formed, whereas one product is clearly favored over the others. DFT calculations point to an influence of the symmetry of the molecular core on the reaction outcome. Indeed, annealing experiments with Ru-TPP and Co-TPP, molecules with a four-fold symmetric core opposed to the two-fold symmetric core of 2H-TPP, yield a more uniform distribution of the reaction products. Thus, by decreasing the symmetry of the core from four-fold (Ru-TPP and Co-TPP) to two-fold (2H-TPP) the selectivity of the reaction outcome

is increased.

If only two *meso* positions of a porphyrin are blocked by phenyl moieties, as for the DPP molecule, two processes occur upon annealing. At moderate annealing temperatures, the phenyl rings react with the macrocycle in a similar way as for 2H-TPP. These planar DPP derivatives covalently couple at elevated annealing temperatures, similar to 2H-P. However, more binding motifs than for 2H-P are observed.

The interaction between the substrate and the adsorbed molecule is studied for a related molecule, the Fe-phthalocyanine. Upon adsorption on the Cu(111) surface FePcs show a two-fold symmetry in STM images despite their four-fold symmetric gas phase configuration. This symmetry reduction is attributed to an asymmetric charge transfer from the substrate to the molecule which probably also causes a bending of the molecule. Thus, the main contribution is found to be an electronic effect and in the STM images a small geometric contribution is observed as well.

Another outcome of the interaction between substrate and molecules is its impact on the reactivity of the molecules. For two different metallo-porphyrins a profound change of the affinity of the metal center towards gas molecules is observed upon adsorption on the Ag(111) surface. Fe-TPP molecules can ligate CO or oxygen molecules with either one or two gas molecules per Fe-TPP. The two gases exhibit a similar geometry when adsorbed on the porphyrin, however, in STM images they can be differentiated. In contrast to the binding ability in the protein hemoglobin, the Ag sample has to be cooled to $20\,\mathrm{K}$ or lower to achieve a sufficient sticking coefficient of CO and oxygen. Due to the strong interaction of the Fe ion with the substrate its binding affinity to the gases is reduced. Consequently, the different chemical environments of the protein and the metal surface significantly influence the binding affinity of Fe-porphyrin to CO and molecular oxygen. On the other hand, Ti-TPP adsorbed on the Ag(111) surface is oxidized at RT upon exposure to molecular oxygen. Three Oxo-Ti-TPP species are identified by STM which represent different configurations of the same species. With this, Ti-TPP fits into a trend across the periodic system from the unreactive Ru-porphyrin over Mn-porphyrin to Ti-porphyrin as the most reactive molecule.

At last, the interfacial interaction of two different molecules is studied. On the Ag(111) surface a model system of a bimolecular organic solar cell is realized with C_{60} as the acceptor and BO-ADPM as the donor. When co-deposited onto the surface the two molecular species separate from each other. Only for low deposition temperatures the molecules are immobilized so that BO-ADPM on top of a C_{60} island can be imaged and the electronic band gap is measured. Thus, the phase separation of the two molecules at the interface is likely to lower the efficiency of the device due to an inefficient charge transfer.

Future experiments could aim to optimize the growth protocols for covalent nanostructures. The goal is to form extended and regular-shaped structures consisting of functional molecules. The

clean coupling of porphyrins on Ag surfaces described in this work shows that porphyrins are promising candidates for the on-surface bottom-up formation of covalent structures. In order to achieve a more directed growth of the porphyrin oligomers the parameters that influence the outcome of the reactions need to be investigated further. In detail, the influence of the coverage of molecules, the molecular flux and the reaction duration could be studied. Moreover, the suitability of different substrates could be tested. The physical and chemical properties of the nanostructures can further be tuned by the employment of various substituents at the macro-cycle and metal ions in the core of the molecule.

Furthermore, AFM measurements with a functionalized tip could help to identify reaction products as *e.g.* the planar porphyrin derivatives, different oligomers or the partially decomposed FePcs.

Additionally, in future experiments the ligation of gaseous molecules to biologically relevant molecules as Fe-porphyrins could be studied on different substrates in order to test the influence of the chemical environment of the porphyrin on the binding affinity. By employing different metal centers, the reactivity towards oxygen can be tuned.

Finally, it could be studied how the magnetic properties of metallo-porphyrins change upon the formation of covalent oligomers and upon the ligation of small gas molecules.

List of publications

K. Diller, F. Klappenberger, F. Allegretti, A. C. Papageorgiou, S. Fischer, A. Wiengarten, S. Joshi, K. Seufert, D. Écija, W. Auwärter, and J. V. Barth. "Investigating the molecule-substrate interaction of prototypic tetrapyrrole compounds: Adsorption and self-metalation of porphine on Cu(111)." *J. Chem. Phys.*, vol. 138, pp. 154710-1–154710-9, 2013.

A. C. Papageorgiou, S. Fischer, S. C. Oh, Ö. Saglam, J. Reichert, A. Wiengarten, K. Seufert, S. Vijayaraghavan, D. Écija, W. Auwärter, F. Allegretti, R. G. Acres, K. C. Prince, K. Diller, F. Klappenberger and J. V. Barth. "Self-Terminating Protocol for an Interfacial Complexation Reaction *in Vacuo* by Metal-Organic Chemical Vapor Deposition." *ACS Nano*, vol. 7, pp. 4520–4526, 2013.

A. Wiengarten, K. Seufert, W. Auwärter, D. Écija, K. Diller, F. Allegretti, F. Bischoff, S. Fischer, D. A. Duncan, A. C. Papageorgiou, F. Klappenberger, R. G. Acres, T. H. Ngo and J. V. Barth. "Surface-assisted Dehydrogenative Homocoupling of Porphine Molecules." *J. Am. Chem. Soc.*, vol. 136, pp. 9346–9354, 2014.

D. A. Duncan, P. S. Deimel, A. Wiengarten, R. Han, R. G. Acres, W. Auwärter, P. Feulner, A. C. Papageorgiou, F. Allegretti, and J. V. Barth. "Immobilised molecular catalysts and the role of the supporting metal substrate." *Chem. Commun.*, vol. 51, pp. 9483–9486, 2015.

A. Wiengarten, J. A. Lloyd, K. Seufert, J. Reichert, W. Auwärter, R. Han, D. A. Duncan, F. Allegretti, S. Fischer, S. C. Oh, Ö. Saglam, L. Jiang, S. Vijayaraghavan, D. Écija, A. C. Papageorgiou and J. V. Barth. "Surface-Assisted Cyclodehydrogenation; Break the Symmetry, Enhance the Selectivity." *accepted by Chem. Eur. J.*

O. Snezhkova, J. Lüder, A. Wiengarten, S. R. Burema, F. Bischoff, Y. He, J. Rusz, J. Knudsen, M.-L. Bocquet, K. Seufert, J. V. Barth, W. Auwärter, B. Brena, and J. Schnadt. "On the Nature of the Bias-Dependent Symmetry Reduction of Iron Phthalocyanine on Cu(111)." *accepted by Phys. Rev. B*

References

[1] I. Langmuir, "The adsorption of gases on plane surfaces of glass, mica and platinum.," *J. Am. Chem. Soc.*, vol. 40, pp. 1361–1403, 1918.

[2] *The official website of the Nobel Prize*, http://www.nobelprize.org/nobel_prizes/physics/laureates/1921/.

[3] C. Davisson and L. Germer, "Diffraction of electrons by a nickel crystal," *Phys. Rev.*, vol. 30, pp. 705–740, 1927.

[4] A. Zangwill, *Physics at Surfaces.* Cambridge University Press, 1988.

[5] G. Binnig, H. Rohrer, C. Gerber, and E. Weibel, "Surface studies by scanning tunneling microscopy," *Phys. Rev. Lett.*, vol. 49, pp. 57–61, 1982.

[6] G. Binnig, C. F. Quate, and C. Gerber, "Atomic force microscope," *Phys. Rev. Lett.*, vol. 56, pp. 930–933, 1986.

[7] H. Lüth, *Surfaces and Interfaces of Solids.* Springer-Verlag, 1993.

[8] K. Oura, V. Lifshits, A. Saranin, A. Zotov, and M. Katayama, *Surface Science - An Introduction.* Springer, 2010.

[9] R. Feynman, "There's plenty of room at the bottom [data storage]," *J. Microelectromech. S.*, vol. 1, pp. 60–66, 1992.

[10] W. Auwärter, D. Écija, F. Klappenberger, and J. V. Barth, "Porphyrins at interfaces," *Nat. Chem.*, vol. 7, pp. 105–120, 2015.

[11] J. T. Groves, "The bioinorganic chemistry of iron in oxygenases and supramolecular assemblies," *P. Natl. Acad. Sci.*, vol. 100, pp. 3569–3574, 2003.

[12] W. Kühlbrandt, D. N. Wang, and Y. Fujiyoshi, "Atomic model of plant light-harvesting complex by electron crystallography," *Nature*, vol. 367, pp. 614–621, 1994.

[13] C. D. Natale, D. Salimbeni, R. Paolesse, A. Macagnano, and A. D'Amico, "Porphyrins-based opto-electronic nose for volatile compounds detection," *Sensor. Actuat. B-Chem.*, vol. 65, pp. 220–226, 2000.

[14] N. A. Rakow and K. S. Suslick, "A colorimetric sensor array for odour visualization," *Nature*, vol. 406, pp. 710–713, 2000.

[15] A.-M. Andringa, M.-J. Spijkman, E. C. Smits, S. G. Mathijssen, P. A. van Hal, S. Setayesh, N. P. Willard, O. V. Borshchev, S. A. Ponomarenko, P. W. Blom, and D. M. de Leeuw,

"Gas sensing with self-assembled monolayer field-effect transistors," *Org. Electron.*, vol. 11, pp. 895–898, 2010.

[16] M. R. Wasielewski, "Photoinduced electron transfer in supramolecular systems for artificial photosynthesis," *Chem. Rev.*, vol. 92, pp. 435–461, 1992.

[17] A. Yella, H.-W. Lee, H. N. Tsao, C. Yi, A. K. Chandiran, M. Nazeeruddin, E. W.-G. Diau, C.-Y. Yeh, S. M. Zakeeruddin, and M. Grätzel, "Porphyrin-sensitized solar cells with cobalt (II/III)-based redox electrolyte exceed 12 percent efficiency," *Science*, vol. 334, pp. 629–634, 2011.

[18] B. Li, J. Li, Y. Fu, and Z. Bo, "Porphyrins with four monodisperse oligofluorene arms as efficient red light-emitting materials," *J. Am. Chem. Soc.*, vol. 126, pp. 3430–3431, 2004.

[19] T. J. Dougherty, C. J. Gomer, B. W. Henderson, G. Jori, D. Kessel, M. Korbelik, J. Moan, and Q. Peng, "Photodynamic therapy," *J. Natl. Cancer I.*, vol. 90, pp. 889–905, 1998.

[20] B. Meunier, "Metalloporphyrins as versatile catalysts for oxidation reactions and oxidative DNA cleavage," *Chem. Rev.*, vol. 92, pp. 1411–1456, 1992.

[21] S. Yoshimoto, A. Tada, K. Suto, R. Narita, and K. Itaya, "Adlayer structure and electrochemical reduction of O2 on self-organized arrays of cobalt and copper tetraphenyl porphines on a Au(111) surface," *Langmuir*, vol. 19, pp. 672–677, 2003.

[22] C. Joachim, J. K. Gimzewski, and A. Aviram, "Electronics using hybrid-molecular and mono-molecular devices," *Nature*, vol. 408, pp. 541–548, 2000.

[23] W. Auwärter, K. Seufert, F. Bischoff, D. Écija, S. Vijayaraghavan, S. Joshi, F. Klappenberger, N. Samudrala, and J. V. Barth, "A surface-anchored molecular four-level conductance switch based on single proton transfer," *Nat. Nanotechnol.*, vol. 7, pp. 41–46, 2012.

[24] N. R. Champness, "Surface chemistry: Making the right connections," *Nat. Chem.*, vol. 4, pp. 149–150, 2012.

[25] G. Franc and A. Gourdon, "Covalent networks through on-surface chemistry in ultra-high vacuum: state-of-the-art and recent developments," *Phys. Chem. Chem. Phys.*, vol. 13, pp. 14283–14292, 2011.

[26] J. Méndez, M. F. López, and J. A. Martín-Gago, "On-surface synthesis of cyclic organic molecules," *Chem. Soc. Rev.*, vol. 40, pp. 4578–4590, 2011.

[27] M. Bieri, S. Blankenburg, M. Kivala, C. A. Pignedoli, P. Ruffieux, K. Müllen, and R. Fasel, "Surface-supported 2D heterotriangulene polymers," *Chem. Commun.*, vol. 47, pp. 10239–10241, 2011.

[28] J. Björk and F. Hanke, "Towards design rules for covalent nanostructures on metal surfaces," *Chem. Europ. J.*, vol. 20, pp. 928–934, 2014.

[29] W. Auwärter, F. Klappenberger, A. Weber-Bargioni, A. Schiffrin, T. Strunskus, C. Wöll, Y. Pennec, A. Riemann, and J. V. Barth, "Conformational adaptation and selective adatom capturing of tetrapyridyl-porphyrin molecules on a copper (111) surface," *J. Am. Chem. Soc.*, vol. 129, pp. 11279–11285, 2007.

[30] O. Snezhkova, J. Lüder, A. Wiengarten, S. R. Burema, F. Bischoff, Y. He, J. Rusz, J. Knudsen, M.-L. Bocquet, K. Seufert, J. V. Barth, W. Auwärter, B. Brena, and J. Schnadt, "On the nature of the bias-dependent symmetry reduction of iron phthalocyanine on Cu(111)," *accepted by Phys. Rev. B.*

[31] A. Weber-Bargioni, W. Auwärter, F. Klappenberger, J. Reichert, S. Lefrançois, T. Strunskus, C. Wöll, A. Schiffrin, Y. Pennec, and J. V. Barth, "Visualizing the frontier orbitals of a conformationally adapted metalloporphyrin," *Chem. Phys. Chem.*, vol. 9, pp. 89–94, 2008.

[32] A. Scheybal, T. Ramsvik, R. Bertschinger, M. Putero, F. Nolting, and T. Jung, "Induced magnetic ordering in a molecular monolayer," *Chem. Phys. Lett.*, vol. 411, pp. 214–220, 2005.

[33] H. Wende, M. Bernien, J. Luo, C. Sorg, N. Ponpandian, J. Kurde, J. Miguel, M. Piantek, X. Xu, P. Eckhold, W. Kuch, K. Baberschke, P. M. Panchmatia, B. Sanyal, P. M. Oppeneer, and O. Eriksson, "Substrate-induced magnetic ordering and switching of iron porphyrin molecules," *Nat. Mater.*, vol. 6, pp. 516–520, 2007.

[34] F. Sedona, M. Di Marino, D. Forrer, A. Vittadini, M. Casarin, A. Cossaro, L. Floreano, A. Verdini, and M. Sambi, "Tuning the catalytic activity of Ag(110)-supported Fe phthalocyanine in the oxygen reduction reaction," *Nat. Mater.*, vol. 11, pp. 970–977, 2012.

[35] K. Seufert, M.-L. Bocquet, W. Auwärter, A. Weber-Bargioni, J. Reichert, N. Lorente, and J. V. Barth, "Cis-dicarbonyl binding at cobalt and iron porphyrins with saddle-shape conformation," *Nat. Chem.*, vol. 3, pp. 114–119, 2011.

[36] D. A. Duncan, P. S. Deimel, A. Wiengarten, R. Han, R. G. Acres, W. Auwärter, P. Feulner, A. C. Papageorgiou, F. Allegretti, and J. V. Barth, "Immobilised molecular catalysts and the role of the supporting metal substrate," *Chem. Commun.*, vol. 51, pp. 9483–9486, 2015.

[37] G. Binnig, H. Rohrer, C. Gerber, and E. Weibel, "Tunneling through a controllable vacuum gap," *Appl. Phys. Lett.*, vol. 40, pp. 178–180, 1982.

[38] G. Binnig, H. Rohrer, C. Gerber, and E. Weibel, "7 x 7 reconstruction on Si(111) resolved in real space," *Phys. Rev. Lett.*, vol. 50, pp. 120–123, 1983.

[39] *The official website of the Nobel Prize*, http://www.nobelprize.org/nobel_prizes/physics/laureates/1986/.

[40] J. V. Barth, "Molecular architectonic on metal surfaces," *Annu. Rev. Phys. Chem.*, vol. 58, pp. 375–407, 2007.

[41] J. Repp, G. Meyer, S. M. Stojković, A. Gourdon, and C. Joachim, "Molecules on insulating films: Scanning-tunneling microscopy imaging of individual molecular orbitals," *Phys. Rev. Lett.*, vol. 94, pp. 026803–1–026803–4, 2005.

[42] R. Wiesendanger, H.-J. Güntherodt, G. Güntherodt, R. J. Gambino, and R. Ruf, "Observation of vacuum tunneling of spin-polarized electrons with the scanning tunneling microscope," *Phys. Rev. Lett.*, vol. 65, pp. 247–250, 1990.

[43] J. Bardeen, "Tunnelling from a many-particle point of view," *Phys. Rev. Lett.*, vol. 6, pp. 57–59, 1961.

[44] J. Tersoff and D. R. Hamann, "Theory and application for the scanning tunneling microscope," *Phys. Rev. Lett.*, vol. 50, pp. 1998–2001, 1983.

[45] J. Tersoff and D. R. Hamann, "Theory of the scanning tunneling microscope," *Phys. Rev. B*, vol. 31, pp. 805–813, 1985.

[46] R. Wiesendanger and H. Güntherodt, eds., *Scanning Tunneling Microscopy III.* Springer Verlag, 1993.

[47] C. J. Chen, *Introduction to Scanning Tunneling Microscopy.* Oxford Science Publications, 2008.

[48] A. Selloni, P. Carnevali, E. Tosatti, and C. D. Chen, "Voltage-dependent scanning-tunneling microscopy of a crystal surface: Graphite," *Phys. Rev. B*, vol. 31, pp. 2602–2605, 1985.

[49] G. Binnig, K. H. Frank, H. Fuchs, N. Garcia, B. Reihl, H. Rohrer, F. Salvan, and A. R. Williams, "Tunneling spectroscopy and inverse photoemission: Image and field states," *Phys. Rev. Lett.*, vol. 55, pp. 991–994, 1985.

[50] R. J. Hamers, R. M. Tromp, and J. E. Demuth, "Surface electronic structure of Si (111)-(7 x 7) resolved in real space," *Phys. Rev. Lett.*, vol. 56, pp. 1972–1975, 1986.

[51] J. A. Stroscio, R. M. Feenstra, and A. P. Fein, "Electronic structure of the Si(111) 2 x 1 surface by scanning-tunneling microscopy," *Phys. Rev. Lett.*, vol. 57, pp. 2579–2582, 1986.

[52] M. Valden, X. Lai, and D. W. Goodman, "Onset of catalytic activity of gold clusters on titania with the appearance of nonmetallic properties," *Science*, vol. 281, pp. 1647–1650, 1998.

[53] R. Hamers and D. Padowitz, *Scanning Probe Microscopy and Spectroscopy*. Wiley-VCH, 2001.

[54] R. Feenstra, J. A. Stroscio, and A. Fein, "Tunneling spectroscopy of the Si(111) 2 x 1 surface," *Surf. Sci.*, vol. 181, pp. 295–306, 1987.

[55] C. Bai, *Scanning Tunneling Microscopy and its Application*. Springer, 1995.

[56] R. Wiesendanger and H. Güntherodt, eds., *Scanning Tunneling Microscopy I*. Springer Verlag, 1992.

[57] A. Bryant, D. P. E. Smith, and C. F. Quate, "Imaging in real time with the tunneling microscope," *Appl. Phys. Lett.*, vol. 48, pp. 832–834, 1986.

[58] G. Meyer, "A simple low-temperature ultrahigh-vacuum scanning tunneling microscope capable of atomic manipulation," *Rev. Sci. Instrum.*, vol. 67, pp. 2960–2965, 1996.

[59] S. Zöphel, *Der Aufbau eines Tieftemperatur-Rastertunnelmikroskops und Strukturuntersuchungen auf vicinalen Kupferoberflächen*. PhD thesis, Freie Universität Berlin, 2000.

[60] *CreaTec Fischer & Co. GmbH*, Industriestr. 9, 74391 Erligheim, www.createc.de.

[61] H. Ibach, *Physics of Surfaces and Interfaces*. Springer, 2006.

[62] K. Seufert, *Nanochemistry with porphyrins - a 2D perspective*. PhD thesis, Technical University of Munich, 2011.

[63] *Pfeiffer Vacuum GmbH*, Berliner Strasse 43, 35614 Asslar, http://www.pfeiffer-vacuum.com/.

[64] *Oerlikon Leybold Vacuum GmbH*, Bonner Str. 498, 50968 Köln, www.oerlikon.com/leyboldvacuum/de.

[65] *SI Scientific Instruments GmbH*, Römerstr. 67, 82205 Gilching bei München, www.si-gmbh.de.

[66] K. Besocke, "An easily operable scanning tunneling microscope," *Surf. Sci.*, vol. 181, pp. 145–153, 1987.

[67] S. D. Kevan and R. H. Gaylord, "High-resolution photoemission study of the electronic structure of the noble-metal (111) surfaces," *Phys. Rev. B*, vol. 36, pp. 5809–5818, 1987.

[68] M. F. Crommie, C. P. Lutz, and D. M. Eigler, "Imaging standing waves in a two-dimensional electron gas," *Nature*, vol. 363, pp. 524–527, 1993.

[69] S. Zöphel, "How to assemble a metal sample holder (manual for the createc LT-STM).,"

[70] W. Auwärter, T. Kreutz, T. Greber, and J. Osterwalder, "XPD and STM investigation of hexagonal boron nitride on Ni(111)," *Surf. Sci.*, vol. 429, pp. 229–236, 1999.

[71] S. Joshi, D. Écija, R. Koitz, M. Iannuzzi, A. P. Seitsonen, J. Hutter, H. Sachdev, S. Vijayaraghavan, F. Bischoff, K. Seufert, J. V. Barth, and W. Auwärter, "Boron nitride on Cu(111): An electronically corrugated monolayer," *Nano Lett.*, vol. 12, pp. 5821–5828, 2012.

[72] S. Y. Leblebici, L. Catane, D. E. Barclay, T. Olson, T. L. Chen, and B. Ma, "Near-infrared azadipyrromethenes as electron donor for efficient planar heterojunction organic solar cells," *Appl. Mater. Interfaces*, vol. 3, pp. 4469–4474, 2011.

[73] J. Stöhr, *NEXAFS Spectroscopy*. Springer Verlag, 1992.

[74] G. Hähner, "Near edge X-ray absorption fine structure spectroscopy as a tool to probe electronic and structural properties of thin organic films and liquids," *Chem. Soc. Rev.*, vol. 35, pp. 1244–1255, 2006.

[75] J. Haase, "SEXAFS und NEXAFS. Röntgen-Absorptionsspektroskopie an Adsorbat-bedeckten Oberflächen," *Chemie in unserer Zeit*, vol. 26, pp. 219–231, 1992.

[76] S. Hüfner, *Photoelectron Spectroscopy, Principles and Applications*. Springer, 2003.

[77] H. Hertz, "Über einen Einfluss des ultravioletten Lichtes auf die elektrische Entladung," *Ann. Physik*, vol. 31, p. 983, 1887.

[78] P. Feulner and D. Menzel, "Simple ways to improve flash desorption measurements from single crystal surfaces," *J. Vac. Sci. Technol.*, vol. 17, pp. 662–663, 1980.

[79] *HyperChem(TM)*, Hypercube. Inc., 1115 NW 4th Street, Gainesville, Florida 32601, USA.

[80] K. Hermann and L. G. M. Pettersson *StoBe software V. 3.0*, deMon developers group, 2007, http://www.fhi-berlin.mpg.de/KHsoftware/StoBe/.

[81] J. P. Perdew, K. Burke, and M. Ernzerhof, "Generalized gradient approximation made simple," *Phys. Rev. Lett.*, vol. 77, pp. 3865–3868, 1996.

[82] B. Hammer, L. B. Hansen, and J. K. Norskov, "Improved adsorption energetics within density-functional theory using revised Perdew-Burke-Ernzerhof functionals," *Phys. Rev. B*, vol. 59, pp. 7413–7421, 1999.

[83] J. Cai, P. Ruffieux, R. Jaafar, M. Bieri, T. Braun, S. Blankenburg, M. Muoth, A. P. Seitsonen, M. Saleh, X. Feng, K. Müllen, and R. Fasel, "Atomically precise bottom-up fabrication of graphene nanoribbons," *Nature*, vol. 466, pp. 470–473, 2010.

[84] J. D. Zimmerman, V. V. Diev, K. Hanson, R. R. Lunt, E. K. Yu, M. E. Thompson, and S. R. Forrest, "Porphyrin-tape/C60 organic photodetectors with 6.5% external quantum efficiency in the near infrared," *Adv. Mater.*, vol. 22, pp. 2780–2783, 2010.

[85] J. D. Biggs, Y. Zhang, D. Healion, and S. Mukamel, "Watching energy transfer in metalloporphyrin heterodimers using stimulated X-ray Raman spectroscopy," *P. Natl. Acad. Sci.*, vol. 110, pp. 15597–15601, 2013.

[86] L. Grill, M. Dyer, L. Lafferentz, M. Persson, M. V. Peters, and S. Hecht, "Nanoarchitectures by covalent assembly of molecular building blocks," *Nat. Nanotechnol.*, vol. 2, pp. 687–691, Nov. 2007.

[87] T. Lin, X. S. Shang, J. Adisoejoso, P. N. Liu, and N. Lin, "Steering on-surface polymerization with metal-directed template," *J. Am. Chem. Soc.*, vol. 135, pp. 3576–3582, 2013.

[88] T. A. Jung, R. R. Schlittler, and J. K. Gimzewski, "Conformational identification of individual adsorbed molecules with the STM," *Nature*, vol. 386, pp. 696–698, 1997.

[89] W. Auwärter, A. Weber-Bargioni, S. Brink, A. Riemann, A. Schiffrin, M. Ruben, and J. V. Barth, "Controlled metalation of self-assembled porphyrin nanoarrays in two dimensions," *Chem. Phys. Chem.*, vol. 8, pp. 250–254, 2007.

[90] W. Auwärter, K. Seufert, F. Klappenberger, J. Reichert, A. Weber-Bargioni, A. Verdini, D. Cvetko, M. Dell´Angela, L. Floreano, A. Cossaro, G. Bavdek, A. Morgante, A. P. Seitsonen, and J. V. Barth, "Site-specific electronic and geometric interface structure of Co-tetraphenyl-porphyrin layers on Ag(111)," *Phys. Rev. B*, vol. 81, pp. 245403–1 – 245403–14, 2010.

[91] S. Mohnani and D. Bonifazi, "Supramolecular architectures of porphyrins on surfaces: The structural evolution from 1D to 2D to 3D to devices," *Coord. Chem. Rev.*, vol. 254, pp. 2342–2362, 2010.

[92] A. Osuka and H. Shimidzu, "Meso, meso-linked porphyrin arrays," *Angew. Chem. Int. Ed.*, vol. 36, pp. 135–137, 1997.

[93] A. Tsuda and A. Osuka, "Fully conjugated porphyrin tapes with electronic absorption bands that reach into infrared," *Science*, vol. 293, pp. 79–82, 2001.

[94] H. S. Cho, D. H. Jeong, S. Cho, D. Kim, Y. Matsuzaki, K. Tanaka, A. Tsuda, and A. Osuka, "Photophysical properties of porphyrin tapes," *J. Am. Chem. Soc.*, vol. 124, pp. 14642–14654, 2002.

[95] A. A. Ryan and M. O. Senge, "Synthesis and functionalization of triply fused porphyrin dimers," *Europ. J. Org. Chem.*, vol. 2013, pp. 3700–3711, 2013.

[96] D. F. Perepichka and M. R. Bryce, "Molecules with exceptionally small HOMO-LUMO gaps," *Angew. Chem. Int. Ed.*, vol. 44, pp. 5370–5373, 2005.

[97] D. Y. Kim, T. K. Ahn, J. H. Kwon, D. Kim, T. Ikeue, N. Aratani, A. Osuka, M. Shigeiwa, and S. Maeda, "Large two-photon absorption (TPA) cross-section of directly linked fused diporphyrins," *J. Phys. Chem. A*, vol. 109, pp. 2996–2999, 2005.

[98] E. Y. Li and N. Marzari, "Conductance switching and many-valued logic in porphyrin assemblies," *J. Phys. Chem. Lett.*, vol. 4, pp. 3039–3044, 2013.

[99] N. Hauptmann, C. Hamann, H. Tang, and R. Berndt, "Soft-landing electrospray deposition of the ruthenium dye N3 on Au(111)," *J. Phys. Chem. C*, vol. 117, pp. 9734–9738, 2013.

[100] M. Pauly, M. Sroka, J. Reiss, G. Rinke, A. Albarghash, R. Vogelgesang, H. Hahne, B. Kuster, J. Sesterhenn, K. Kern, and S. Rauschenbach, "A hydrodynamically optimized nano-electrospray ionization source and vacuum interface," *Analyst*, vol. 139, pp. 1856–1867, 2014.

[101] M. I. Veld, P. Iavicoli, S. Haq, D. B. Amabilino, and R. Raval, "Unique intermolecular reaction of simple porphyrins at a metal surface gives covalent nanostructures," *Chem. Commun.*, pp. 1536–1538, 2008.

[102] L. Lafferentz, V. Eberhardt, C. Dri, C. Africh, G. Comelli, F. Esch, S. Hecht, and L. Grill, "Controlling on-surface polymerization by hierarchical and substrate-directed growth," *Nat. Chem.*, vol. 4, pp. 215–220, 2012.

[103] M. S. Dyer, A. Robin, S. Haq, R. Raval, M. Persson, and J. Klimes, "Understanding the interaction of the porphyrin macrocycle to reactive metal substrates: Structure, bonding, and adatom capture," *ACS Nano*, vol. 5, pp. 1831–1838, 2011.

[104] F. Bischoff, K. Seufert, W. Auwärter, S. Joshi, S. Vijayaraghavan, D. Écija, K. Diller, A. C. Papageorgiou, S. Fischer, F. Allegretti, D. A. Duncan, F. Klappenberger, F. Blobner, R. Han, and J. V. Barth, "How surface bonding and repulsive interactions cause phase transformations: Ordering of a prototype macrocyclic compound on Ag(111)," *ACS Nano*, vol. 7, pp. 3139–3149, 2013.

[105] K. Diller, F. Klappenberger, F. Allegretti, A. C. Papageorgiou, S. Fischer, A. Wiengarten, S. Joshi, K. Seufert, D. Écija, W. Auwärter, and J. V. Barth, "Investigating the molecule-substrate interaction of prototypic tetrapyrrole compounds: Adsorption and self-metalation of porphine on Cu(111)," *J. Chem. Phys.*, vol. 138, pp. 154710–1–154710–9, 2013.

[106] J. M. Gottfried, K. Flechtner, A. Kretschmann, T. Lukasczyk, and H.-P. Steinrück, "Direct synthesis of a metalloporphyrin complex on a surface," *J. Am. Chem. Soc.*, vol. 128, pp. 5644–5645, 2006.

[107] F. Buchner, K. Flechtner, Y. Bai, E. Zillner, I. Kellner, H.-P. Steinrück, H. Marbach, and J. M. Gottfried, "Coordination of iron atoms by tetraphenylporphyrin monolayers and multilayers on Ag(111) and formation of iron-tetraphenylporphyrin," *J. Phys. Chem. C*, vol. 112, pp. 15458–15465, 2008.

[108] A. C. Papageorgiou, S. Fischer, S. C. Oh, O. Saglam, J. Reichert, A. Wiengarten, K. Seufert, S. Vijayaraghavan, D. Écija, W. Auwärter, F. Allegretti, R. G. Acres, K. C. Prince, K. Diller, F. Klappenberger, and J. V. Barth, "Self-terminating protocol for an interfacial complexation reaction in vacuo by metal-organic chemical vapor deposition," *ACS Nano*, vol. 7, pp. 4520–4526, 2013.

[109] M. Lackinger and W. M. Heckl, "A STM perspective on covalent intermolecular coupling reactions on surfaces," *J. Phys. D: Appl. Phys.*, vol. 44, p. 464011, 2011.

[110] J. Eichhorn, D. Nieckarz, O. Ochs, D. Samanta, M. Schmittel, P. J. Szabelski, and M. Lackinger, "On-surface Ullmann coupling: The influence of kinetic reaction parameters on the morphology and quality of covalent networks," *ACS Nano*, vol. 8, pp. 7880–7889, 2014.

[111] A. Wiengarten, K. Seufert, W. Auwärter, D. Écija, K. Diller, F. Allegretti, F. Bischoff, S. Fischer, D. A. Duncan, A. C. Papageorgiou, F. Klappenberger, R. G. Acres, T. H. Ngo, and J. V. Barth, "Surface-assisted dehydrogenative homocoupling of porphine molecules," *J. Am. Chem. Soc.*, vol. 136, pp. 9346–9354, 2014.

[112] S. Haq, F. Hanke, M. S. Dyer, M. Persson, P. Iavicoli, D. B. Amabilino, and R. Raval, "Clean coupling of unfunctionalized porphyrins at surfaces to give highly oriented organometallic oligomers," *J. Am. Chem. Soc.*, vol. 133, pp. 12031–12039, 2011.

[113] Y. Nakamura, N. Aratani, H. Shinokubo, A. Takagi, T. Kawai, T. Matsumoto, Z. S. Yoon, D. Y. Kim, T. K. Ahn, D. Kim, A. Muranaka, N. Kobayashi, and A. Osuka, "A directly fused tetrameric porphyrin sheet and its anomalous electronic properties that arise from the planar cyclooctatetraene core," *J. Am. Chem. Soc.*, vol. 128, pp. 4119–4127, 2006.

[114] Y.-Q. Zhang, N. Kepčija, M. Kleinschrodt, K. Diller, S. Fischer, A. C. Papageorgiou, F. Allegretti, J. Björk, S. Klyatskaya, F. Klappenberger, M. Ruben, and J. V. Barth, "Homo-coupling of terminal alkynes on a noble metal surface," *Nat. Commun.*, vol. 3, p. 1286, 2012.

[115] J. Björk, Y.-Q. Zhang, F. Klappenberger, J. V. Barth, and S. Stafström, "Unraveling the mechanism of the covalent coupling between terminal alkynes on a noble metal," *J. Phys. Chem. C*, vol. 118, pp. 3181–3187, 2014.

[116] A. Streitwieser and C. H. Heathcock, *Introduction to organic chemistry.* New York: Macmillan, 1985.

[117] A. L. Pinardi, G. Otero-Irurueta, I. Palacio, J. I. Martinez, C. Sanchez-Sanchez, M. Tello, C. Rogero, A. Cossaro, A. Preobrajenski, B. Gómez-Lor, A. Jancarik, I. G. Stará, I. Starý, M. F. Lopez, J. Méndez, and J. A. Martin-Gago, "Tailored formation of n-doped nanoarchitectures by diffusion-controlled on-surface (cyclo)dehydrogenation of heteroaromatics," *ACS Nano*, vol. 7, pp. 3676–3684, 2013.

[118] T.-C. Tseng, C. Urban, Y. Wang, R. Otero, S. L. Tait, M. Alcami, D. Écija, M. Trelka, J. M. Gallego, N. Lin, M. Konuma, U. Starke, A. Nefedov, A. Langner, C. Woell, M. A. Herranz, F. Martín, N. Martín, K. Kern, and R. Miranda, "Charge-transfer-induced structural rearrangements at both sides of organic/metal interfaces," *Nat. Chem.*, vol. 2, pp. 374–379, 2010.

[119] I. Dabo, A. Ferretti, C.-H. Park, N. Poilvert, Y. Li, M. Cococcioni, and N. Marzari, "Donor and acceptor levels of organic photovoltaic compounds from first principles," *Phys. Chem. Chem. Phys.*, vol. 15, pp. 685–695, 2013.

[120] Y. Yamaguchi, "Time-dependent density functional calculations of fully pi-conjugated zinc oligoporphyrins," *J. Chem. Phys.*, vol. 117, pp. 9688–9694, 2002.

[121] S. S. Zade and M. Bendikov, "From oligomers to polymer: Convergence in the HOMO-LUMO gaps of conjugated oligomers," *Org. Lett.*, vol. 8, pp. 5243–5246, 2006.

[122] S. S. Zade, N. Zamoshchik, and M. Bendikov, "From short conjugated oligomers to conjugated polymers. Lessons from studies on long conjugated oligomers," *Acc. Chem. Res.*, vol. 44, pp. 14–24, 2011.

[123] L. Cardenas, R. Gutzler, J. Lipton-Duffin, C. Fu, J. L. Brusso, L. E. Dinca, M. Vondráček, Y. Fagot-Revurat, D. Malterre, F. Rosei, and D. F. Perepichka, "Synthesis and electronic structure of a two dimensional pi-conjugated polythiophene," *Chem. Sci.*, vol. 4, pp. 3263–3268, 2013.

[124] W. Auwärter, A. Weber-Bargioni, A. Riemann, A. Schiffrin, O. Gröning, R. Fasel, and J. V. Barth, "Self-assembly and conformation of tetrapyridyl-porphyrin molecules on Ag(111)," *J. Chem. Phys.*, vol. 124, pp. 194708–1–194708–6, 2006.

[125] S.-H. Chang, S. Kuck, J. Brede, L. Lichtenstein, G. Hoffmann, and R. Wiesendanger, "Symmetry reduction of metal phthalocyanines on metals," *Phys. Rev. B*, vol. 78, pp. 233409–1–233409–4, 2008.

[126] R. Cuadrado, J. I. Cerda, Y. Wang, G. Xin, R. Berndt, and H. Tang, "CoPc adsorption on Cu(111): Origin of the C4 to C2 symmetry reduction," *J. Chem. Phys.*, vol. 133, pp. 154701–1–154701–7, 2010.

[127] M. Bieri, M.-T. Nguyen, O. Gröning, J. Cai, M. Treier, K. Ait-Mansour, P. Ruffieux, C. A. Pignedoli, D. Passerone, M. Kastler, K. Müllen, and R. Fasel, "Two-dimensional polymer formation on surfaces: Insight into the roles of precursor mobility and reactivity," *J. Am. Chem. Soc.*, vol. 132, pp. 16669–16676, 2010.

[128] R. Gutzler, L. Cardenas, J. Lipton-Duffin, M. El Garah, L. E. Dinca, C. E. Szakacs, C. Fu, M. Gallagher, M. Vondráček, M. Rybachuk, D. F. Perepichka, and F. Rosei, "Ullmann-type coupling of brominated tetrathienoanthracene on copper and silver," *Nanoscale*, vol. 6, pp. 2660–2668, 2014.

[129] K.-H. Chung, B.-G. Koo, H. Kim, J. K. Yoon, J.-H. Kim, Y.-K. Kwon, and S.-J. Kahng, "Electronic structures of one-dimensional metal-molecule hybrid chains studied using scanning tunneling microscopy and density functional theory," *Phys. Chem. Chem. Phys.*, vol. 14, pp. 7304–7308, 2012.

[130] M. Matena, T. Riehm, M. Stöhr, T. A. Jung, and L. H. Gade, "Transforming surface coordination polymers into covalent surface polymers: Linked polycondensed aromatics through oligomerization of n-heterocyclic carbene intermediates," *Angew. Chem. Int. Ed.*, vol. 47, pp. 2414–2417, 2008.

[131] H. Walch, R. Gutzler, T. Sirtl, G. Eder, and M. Lackinger, "Material- and orientation-dependent reactivity for heterogeneously catalyzed carbon-bromine bond homolysis," *J. Phys. Chem. C*, vol. 114, pp. 12604–12609, 2010.

[132] F. Hanke, S. Haq, R. Raval, and M. Persson, "Heat-to-connect: Surface commensurability directs organometallic one-dimensional self-assembly," *ACS Nano*, vol. 5, pp. 9093–9103, 2011.

[133] M. Di Giovannantonio, M. El Garah, J. Lipton-Duffin, V. Meunier, L. Cardenas, Y. Fagot Revurat, A. Cossaro, A. Verdini, D. F. Perepichka, F. Rosei, and G. Contini, "Insight into organometallic intermediate and its evolution to covalent bonding in surface-confined Ullmann polymerization," *ACS Nano*, vol. 7, pp. 8190–8198, 2013.

[134] R. Gutzler, H. Walch, G. Eder, S. Kloft, W. M. Heckl, and M. Lackinger, "Surface mediated synthesis of 2D covalent organic frameworks: 1,3,5-tris(4-bromophenyl)benzene on graphite(001), Cu(111), and Ag(110)," *Chem. Commun.*, pp. 4456–4458, 2009.

[135] J. Eichhorn, T. Strunskus, A. Rastgoo-Lahrood, D. Samanta, M. Schmittel, and M. Lackinger, "On-surface Ullmann polymerization via intermediate organometallic networks on Ag(111)," *Chem. Commun.*, vol. 50, pp. 7680–7682, 2014.

[136] M. Koch, F. Ample, C. Joachim, and L. Grill, "Voltage-dependent conductance of a single graphene nanoribbon," *Nat. Nanotechnol.*, vol. 7, pp. 713–717, 2012.

[137] B. M. Trost, "Selectivity: A key to synthetic efficiency," *Science*, vol. 219, pp. 245–250, 1983.

[138] G. A. Somorjai and J. Y. Park, "Molecular factors of catalytic selectivity," *Angew. Chem. Int. Ed.*, vol. 47, pp. 9212–9228, 2008.

[139] P. Anastas and N. Eghbali, "Green chemistry: Principles and practice," *Chem. Soc. Rev.*, vol. 39, pp. 301–312, 2010.

[140] H.-U. Blaser, B. Pugin, and F. Spindler, "Progress in enantioselective catalysis assessed from an industrial point of view," *J. Mol. Catal. A - Chem.*, vol. 231, pp. 1–20, 2005.

[141] P. Linnane, N. Magnus, and P. Magnus, "Induction of molecular asymmetry by a remote chiral group," *Nature*, vol. 385, pp. 799–801, 1997.

[142] A. Lennartson, S. Olsson, J. Sundberg, and M. Hakansson, "A different approach to enantioselective organic synthesis: Absolute asymmetric synthesis of organometallic reagents," *Angew. Chem. Int. Ed.*, vol. 48, pp. 3137–3140, 2009.

[143] P. Etayo and A. Vidal-Ferran, "Rhodium-catalysed asymmetric hydrogenation as a valuable synthetic tool for the preparation of chiral drugs," *Chem. Soc. Rev.*, vol. 42, pp. 728–754, 2013.

[144] A. Warmflash, B. Sorre, F. Etoc, E. D. Siggia, and A. H. Brivanlou, "A method to recapitulate early embryonic spatial patterning in human embryonic stem cells," *Nat. Methods*, vol. 11, pp. 847–854, 2014.

[145] O. I. Kolodiazhnyi, "Multiple stereoselectivity and its application in organic synthesis," *Tetrahedron*, vol. 59, pp. 5953–6018, 2003.

[146] K. Gopalaiah, "Chiral iron catalysts for asymmetric synthesis," *Chem. Rev.*, vol. 113, pp. 3248–3296, 2013.

[147] M. Heitbaum, F. Glorius, and I. Escher, "Asymmetric heterogeneous catalysis," *Angew. Chem. Int. Ed.*, vol. 45, pp. 4732–4762, 2006.

[148] G. Kyriakou, S. K. Beaumont, and R. M. Lambert, "Aspects of heterogeneous enantioselective catalysis by metals," *Langmuir*, vol. 27, pp. 9687–9695, 2011.

[149] A. Violi, "Cyclodehydrogenation reactions to cyclopentafused polycyclic aromatic hydrocarbons," *J. Phys. Chem. A*, vol. 109, pp. 7781–7787, 2005.

[150] M. Treier, C. A. Pignedoli, T. Laino, R. Rieger, K. Müllen, D. Passerone, and R. Fasel, "Surface-assisted cyclodehydrogenation provides a synthetic route towards easily processable and chemically tailored nanographenes," *Nat. Chem.*, vol. 3, pp. 61–67, 2011.

[151] G. DiSanto, S. Blankenburg, C. Castellarin-Cudia, M. Fanetti, P. Borghetti, L. Sangaletti, L. Floreano, A. Verdini, E. Magnano, F. Bondino, C. A. Pignedoli, M.-T. Nguyen, R. Gaspari, D. Passerone, and A. Goldoni, "Supramolecular engineering through temperature-induced chemical modification of 2H-tetraphenylporphyrin on Ag(111): Flat phenyl conformation and possible dehydrogenation reactions," *Chem. Europ. J.*, vol. 17, pp. 14354–14359, 2011.

[152] F. Buchner, I. Kellner, W. Hieringer, A. Gorling, H.-P. Steinrück, and H. Marbach, "Ordering aspects and intramolecular conformation of tetraphenylporphyrins on Ag(111)," *Phys. Chem. Chem. Phys.*, vol. 12, pp. 13082–13090, 2010.

[153] A. Wiengarten, J. A. Lloyd, K. Seufert, J. Reichert, W. Auwärter, R. Han, D. A. Duncan, F. Allegretti, S. Fischer, S. C. Oh, O. Saglam, L. Jiang, S. Vijayaraghavan, D. Écija, A. C. Papageorgiou, and J. V. Barth, "Surface-assisted cyclodehydrogenation; break the symmetry, enhance the selectivity," *accepted by Chem. Europ. J.*

[154] P. W. Atkins and J. de Paula, *Elements of Physical Chemistry.* Oxford: Wiley-VCH, 2013.

[155] J. Hennig and H.-H. Limbach, "Kinetic study of hydrogen tunnelling in meso-tetraphenylporphine by nuclear magnetic resonance lineshape analysis and selective $T_{1\rho}$-relaxation time measurements," *J. Chem. Soc. Farad. T. 2*, vol. 75, pp. 752–766, 1978.

[156] M. Röckert, M. Franke, Q. Tariq, S. Ditze, M. Stark, P. Uffinger, D. Wechsler, U. Singh, J. Xiao, H. Marbach, H.-P. Steinrück, and O. Lytken, "Coverage- and temperature-dependent metalation and dehydrogenation of tetraphenylporphyrin on Cu(111)," *Chem. Europ. J.*, vol. 20, pp. 8948–8953, 2014.

[157] M. Koch, *Growth and Characterization of Single Molecular Wires on Metal Surfaces.* PhD thesis, Freie Universität Berlin, 2013.

[158] K. Diller, F. Klappenberger, M. Marschall, K. Hermann, A. Nefedov, C. Wöll, and J. V. Barth, "Self-metalation of 2h-tetraphenylporphyrin on Cu(111): An x-ray spectroscopy study," *J. Chem. Phys.*, vol. 136, pp. 014705–1–014705–13, 2012.

[159] J. A. A. Elemans, R. van Hameren, R. J. M. Nolte, and A. E. Rowan, "Molecular materials by self-assembly of porphyrins, phthalocyanines, and perylenes," *Adv. Mater.*, vol. 18, pp. 1251–1266, 2006.

[160] R. Zhou, F. Josse, W. Göpel, Z. Z. Öztürk, and O. Bekaroglu, "Phthalocyanines as sensitive materials for chemical sensors," *Appl. Organomet. Chem.*, vol. 10, pp. 557–577, 1996.

[161] T. Tsuzuki, Y. Shirota, J. Rostalski, and D. Meissner, "The effect of fullerene doping on photoelectric conversion using titanyl phthalocyanine and a perylene pigment," *Sol. Energ. Mat. Sol. C*, vol. 61, pp. 1–8, 2000.

[162] C. Di, F. Zhang, and D. Zhu, "Multi-functional integration of organic field-effect transistors (OFETs): Advances and perspectives," *Adv. Mater.*, vol. 25, pp. 313–330, 2013.

[163] B. W. Heinrich, C. Iacovita, T. Brumme, D.-J. Choi, L. Limot, M. V. Rastei, W. A. Hofer, J. Kortus, and J.-P. Bucher, "Direct observation of the tunneling channels of a chemisorbed molecule," *J. Phys. Chem. Lett.*, vol. 1, pp. 1517–1523, 2010.

[164] L. Gao, W. Ji, Y. B. Hu, Z. H. Cheng, Z. T. Deng, Q. Liu, N. Jiang, X. Lin, W. Guo, S. X. Du, W. A. Hofer, X. C. Xie, and H.-J. Gao, "Site-specific Kondo effect at ambient temperatures in iron-based molecules," *Phys. Rev. Lett.*, vol. 99, pp. 106402–1–106402–4, 2007.

[165] A. Mugarza, R. Robles, C. Krull, R. Korytár, N. Lorente, and P. Gambardella, "Electronic and magnetic properties of molecule-metal interfaces: Transition-metal phthalocyanines adsorbed on Ag(100)," *Phys. Rev. B*, vol. 85, pp. 155437–1–155437–13, 2012.

[166] R. Rehman, W. Dou, H. Qian, H. Mao, F. Floether, H. Zhang, H. Li, P. He, and S. Bao, "Adsorption behavior of iron phthalocyanine at the initial stage on Cu(100) surface," *Surf. Sci.*, vol. 606, pp. 1749–1754, 2012.

[167] H. Karacuban, M. Lange, J. Schaffert, O. Weingart, T. Wagner, and R. Möller, "Substrate-induced symmetry reduction of CuPc on Cu(111): An LT-STM study," *Surf. Sci.*, vol. 603, pp. L39–L43, 2009.

[168] Y. Wang, J. Kröger, R. Berndt, and W. Hofer, "Structural and electronic properties of ultrathin tin-phthalocyanine films on Ag(111) at the single-molecule level," *Angew. Chem. Int. Ed.*, vol. 48, pp. 1261–1265, 2009.

[169] J. D. Baran and J. A. Larsson, "Theoretical insights into adsorption of cobalt phthalocyanine on Ag(111): A combination of chemical and van der Waals bonding," *J. Phys. Chem. C*, vol. 117, pp. 23887–23898, 2013.

[170] K. Manandhar, T. Ellis, K. Park, T. Cai, Z. Song, and J. Hrbek, "A scanning tunneling microscopy study on the effect of post-deposition annealing of copper phthalocyanine thin films," *Surf. Sci.*, vol. 601, pp. 3623–3631, 2007.

[171] A. Scarfato, S.-H. Chang, S. Kuck, J. Brede, G. Hoffmann, and R. Wiesendanger, "Scanning tunneling microscope study of iron(II) phthalocyanine growth on metals and insulating surfaces," *Surf. Sci.*, vol. 602, pp. 677–683, 2008.

[172] M. Ziegler, N. Néel, A. Sperl, J. Kröger, and R. Berndt, "Local density of states from constant-current tunneling spectra," *Phys. Rev. B*, vol. 80, pp. 125402–1–125402–6, 2009.

[173] O. Snezhkova. Private Communication.

[174] A. Gulino, T. Gupta, P. G. Mineo, and M. E. van der Boom, "Selective NO_x optical sensing with surface-confined osmium polypyridyl complexes," *Chem. Commun.*, pp. 4878–4880, 2007.

[175] B. R. Takulapalli, G. M. Laws, P. A. Liddell, J. Andreasson, Z. Erno, D. Gust, and T. J. Thornton, "Electrical detection of amine ligation to a metalloporphyrin via a hybrid SOI-MOSFET," *J. Am. Chem. Soc.*, vol. 130, pp. 2226–2233, 2008.

[176] N. Ballav, C. Wäckerlin, D. Siewert, P. M. Oppeneer, and T. A. Jung, "Emergence of on-surface magnetochemistry," *J. Phys. Chem. Lett.*, vol. 4, pp. 2303–2311, 2013.

[177] A. Stróżecka, M. Soriano, J. I. Pascual, and J. J. Palacios, "Reversible change of the spin state in a manganese phthalocyanine by coordination of CO molecule," *Phys. Rev. Lett.*, vol. 109, p. 147202, 2012.

[178] N. Tsukahara, E. Minamitani, Y. Kim, M. Kawai, and N. Takagi, "Controlling orbital-selective Kondo effects in a single molecule through coordination chemistry," *J. Chem. Phys.*, vol. 141, pp. 054702–1–054702–9, 2014.

[179] P. Gambardella, S. Stepanow, A. Dmitriev, J. Honolka, F. M. F. de Groot, M. Lingenfelder, S. S. Gupta, D. D. Sarma, P. Bencok, S. Stanescu, S. Clair, S. Pons, N. Lin, A. P. Seitsonen, H. Brune, J. V. Barth, and K. Kern, "Supramolecular control of the magnetic anisotropy in two-dimensional high-spin Fe arrays at a metal interface," *Nat. Mater.*, vol. 8, pp. 189–193, 2009.

[180] C. Wäckerlin, D. Chylarecka, A. Kleibert, K. Müller, C. Iacovita, F. Nolting, T. A. Jung, and N. Ballav, "Controlling spins in adsorbed molecules by a chemical switch," *Nat. Commun.*, vol. 1, p. 61, 2010.

[181] C. Coperet, M. Chabanas, R. Petroff Saint-Arroman, and J.-M. Basset, "Homogeneous and heterogeneous catalysis: Bridging the gap through surface organometallic chemistry," *Angew. Chem. Int. Ed.*, vol. 42, pp. 156–181, 2003.

[182] G. A. Somorjai, A. M. Contreras, M. Montano, and R. M. Rioux, "Clusters, surfaces, and catalysis," *P. Natl. Acad. Sci.*, vol. 103, pp. 10577–10583, 2006.

[183] J. V. Barth, G. Costantini, and K. Kern, "Engineering atomic and molecular nanostructures at surfaces," *Nature*, vol. 437, pp. 671–679, 2005.

[184] W. Hieringer, K. Flechtner, A. Kretschmann, K. Seufert, W. Auwärter, J. V. Barth, A. Görling, H.-P. Steinrück, and J. M. Gottfried, "The surface trans effect: Influence of axial ligands on the surface chemical bonds of adsorbed metalloporphyrins," *J. Am. Chem. Soc.*, vol. 133, pp. 6206–6222, 2011.

[185] B. A. Springer, S. G. Sligar, J. S. Olson, and G. N. J. Phillips, "Mechanisms of ligand recognition in myoglobin," *Chem. Rev.*, vol. 94, pp. 699–714, 1994.

[186] J. T. Groves and R. Quinn, "Aerobic epoxidation of olefins with ruthenium porphyrin catalysts," *J. Am. Chem. Soc.*, vol. 107, pp. 5790–5792, 1985.

[187] M. Bowker, *The basis and applications of heterogeneous catalysis.* Oxford University Press, 1998.

[188] F. Buchner, V. Schwald, K. Comanici, H.-P. Steinrück, and H. Marbach, "Microscopic evidence of the metalation of a free-base porphyrin monolayer with iron," *Chem. Phys. Chem.*, vol. 8, pp. 241–243, 2007.

[189] S. Joshi, F. Bischoff, R. Koitz, D. Écija, K. Seufert, A. P. Seitsonen, J. Hutter, K. Diller, J. I. Urgel, H. Sachdev, J. V. Barth, and W. Auwärter, "Control of molecular organization and energy level alignment by an electronically nanopatterned boron nitride template," *ACS Nano*, vol. 8, pp. 430–442, 2014.

[190] V. D. Pham, J. Lagoute, O. Mouhoub, F. Joucken, V. Repain, C. Chacon, A. Bellec, Y. Girard, and S. Rousset, "Electronic interaction between nitrogen-doped graphene and porphyrin molecules," *ACS Nano*, vol. 8, pp. 9403–9409, 2014.

[191] M. Palummo, C. Hogan, F. Sottile, P. Bagalá, and A. Rubio, "Ab initio electronic and optical spectra of free-base porphyrins: The role of electronic correlation," *J. Chem. Phys.*, vol. 131, pp. 084102–1–084102–7, 2009.

[192] X. Blase, C. Attaccalite, and V. Olevano, "First-principles *GW* calculations for fullerenes, porphyrins, phtalocyanine, and other molecules of interest for organic photovoltaic applications," *Phys. Rev. B*, vol. 83, p. 115103, 2011.

[193] J. I. Urgel, M. Schwarz, M. Garnica, D. Stassen, D. Bonifazi, D. Ecija, J. V. Barth, and W. Auwärter, "Controlling coordination reactions and assembly on a Cu(111) supported boron nitride monolayer," *J. Am. Chem. Soc.*, vol. 137, pp. 2420–2423, 2015.

[194] K. Seufert, W. Auwärter, and J. V. Barth, "Discriminative response of surface-confined metalloporphyrin molecules to carbon and nitrogen monoxide," *J. Am. Chem. Soc.*, vol. 132, pp. 18141–18146, 2010.

[195] M. F. Perutz, "Regulation of oxygen affinity of hemoglobin: Influence of structure of the globin on the heme iron," *Annu. Rev. Biochem.*, vol. 48, pp. 327–386, 1979.

[196] H. Chen, M. Ikeda-Saito, and S. Shaik, "Nature of the Fe-O2 bonding in oxy-myoglobin: Effect of the protein," *J. Am. Chem. Soc.*, vol. 130, pp. 14778–14790, 2008.

[197] D. A. Duncan. Private Communication.

[198] Y. Bai, F. Buchner, I. Kellner, M. Schmid, F. Vollnhals, H.-P. Steinrück, H. Marbach, and J. M. Gottfried, "Adsorption of cobalt (II) octaethylporphyrin and 2H-octaethylporphyrin on Ag(111): new insight into the surface coordinative bond," *New J. Phys.*, vol. 11, p. 125004, 2009.

[199] A. Fujishima and K. Honda, "Electrochemical photolysis of water at a semiconductor electrode," *Nature*, vol. 238, pp. 37–38, 1972.

[200] A. L. Sobolewski and W. Domcke, "Photoinduced water splitting with oxotitanium porphyrin: a computational study," *Phys. Chem. Chem. Phys.*, vol. 14, pp. 12807–12817, 2012.

[201] O. Morawski, K. Izdebska, E. Karpiuk, J. Nowacki, A. Suchocki, and A. L. Sobolewski, "Photoinduced water splitting with oxotitanium tetraphenylporphyrin," *Phys. Chem. Chem. Phys.*, vol. 16, pp. 15256–15262, 2014.

[202] P. S. Deimel, "Ligation of adducts to tetrapyrrolic metal-organic complexes adsorbed on Ag(111)," Master's thesis, Technical University of Munich, 2014.

[203] B. E. Murphy, S. A. Krasnikov, N. N. Sergeeva, A. A. Cafolla, A. B. Preobrajenski, A. N. Chaika, O. Lübben, and I. V. Shvets, "Homolytic cleavage of molecular oxygen by manganese porphyrins supported on Ag(111)," *ACS Nano*, vol. 8, pp. 5190–5198, 2014.

[204] T. M. Clarke and J. R. Durrant, "Charge photogeneration in organic solar cells," *Chem. Rev.*, vol. 110, pp. 6736–6767, 2010.

[205] R. R. Lunt and V. Bulovic, "Transparent, near-infrared organic photovoltaic solar cells for window and energy-scavenging applications," *Appl. Phys. Lett.*, vol. 98, pp. 113305–1–113305–3, 2011.

[206] H. Hoppe and N. S. Sariciftci, "Organic solar cells: An overview," *J. Mater. Res.*, vol. 19, pp. 1924–1945, 2004.

[207] M. T. Lloyd, J. E. Anthony, and G. G. Malliaras, "Photovoltaics from soluble small molecules," *Mater. Today*, vol. 10, pp. 34–41, 2007.

[208] N. Martín, L. Sánchez, B. Illescas, and I. Pérez, "C60-based electroactive organofullerenes," *Chem. Rev.*, vol. 98, pp. 2527–2548, 1998.

[209] A. Ojala, A. Petersen, A. Fuchs, R. Lovrincic, C. Pölking, J. Trollmann, J. Hwang, C. Lennartz, H. Reichelt, H. W. Höffken, A. Pucci, P. Erk, T. Kirchartz, and F. Würthner, "Merocyanine/C_{60} planar heterojunction solar cells: Effect of dye orientation on exciton dissociation and solar cell performance," *Adv. Func. Mater.*, vol. 22, pp. 86–96, 2012.

[210] P. Erwin and M. E. Thompson, "Elucidating the interplay between dark current coupling and open circuit voltage in organic photovoltaics," *Appl. Phys. Lett.*, vol. 98, no. 22, pp. 223305–1–223305–3, 2011.

[211] B. P. Rand, D. Cheyns, K. Vasseur, N. C. Giebink, S. Mothy, Y. Yi, V. Coropceanu, D. Beljonne, J. Cornil, J.-L. Brédas, and J. Genoe, "The impact of molecular orientation on the photovoltaic properties of a phthalocyanine/fullerene heterojunction," *Adv. Func. Mater.*, vol. 22, pp. 2987–2995, 2012.

[212] M. Olguin, R. R. Zope, and T. Baruah, "Effect of geometrical orientation on the charge-transfer energetics of supramolecular (tetraphenyl)-porphyrin/C_{60} dyads," *J. Chem. Phys.*, vol. 138, pp. 074306–1–074306–8, 2013.

[213] J. R. Tumbleston, B. A. Collins, L. Yang, A. C. Stuart, E. Gann, W. Ma, W. You, and H. Ade, "The influence of molecular orientation on organic bulk heterojunction solar cells," *Nat. Photonics*, vol. 8, pp. 385–391, 2014.

[214] T. Sakurai, X.-D. Wang, Q. Xue, Y. Hasegawa, T. Hashizume, and H. Shinohara, "Scanning tunneling microscopy study of fullerenes," *Prog. Surf. Sci.*, vol. 51, pp. 263–408, 1996.

[215] S. Vijayaraghavan, D. Écija, W. Auwärter, S. Joshi, K. Seufert, A. P. Seitsonen, K. Tashiro, and J. V. Barth, "Selective supramolecular fullerene-porphyrin interactions and switching in surface-confined C_{60}-Ce(TPP)$_2$ dyads," *Nano Lett.*, vol. 12, pp. 4077–4083, 2012.

Acknowledgment

In the end, I would like to thank everybody who contributed to this work and supported me during this time.

At first, I thank Prof. Dr. Johannes Barth for supervising my work and giving me the opportunity to experience the inspiring atmosphere of his group. I am thankful for his expert scientific advice, the interesting discussions and his support. For the supervision of my work I am also very grateful to Prof. Dr. Willi Auwärter. He knows both the experimental setup and the scientific background and was always able to answer my questions. I am thankful for the scientific discussions, the proof-reading, the support in the lab and the enjoyable working atmosphere. Furthermore, I would like to thank Dr. Knud Seufert for introducing me to the STM and the lab, for supervising many of my experiments and for passing on the porphyrins to me.

I am grateful to the whole LT-STM/AFM group. The size and composition changed quite a bit but it was always a productive and friendly environment and I enjoyed the common times in the lab, the discussions and the support from everybody. I thank Dr. Saranyan Vijayaraghavan and Sushobhan Joshi for introducing me to the lab; Felix Bischoff, José I. Urgel Tendero and Tobias Kaposi for the teamwork during the past three years; Dr. David Écija and Dr. Manuela Garnica Alonso for the scientific and other advice and Yuanqin He, Martin Schwarz, Jacob Ducke and Domenik Zimmermann for their support.

Moreover, I would like to thank Dr. Anthoula Papageorgiou, Dr. Joachim Reichert, Dr. Francesco Allegretti, Dr. Carlos-Andres Palma, Dr. Özge Saglam, Dr. Florian Klappenberger, Dr. David A. Duncan, Dr. Katharina Diller, Julian Lloyd and Prof. Dr. Peter Feulner for the joint projects and for always answering my questions.

I am also grateful to Karl Eberle, Reinhold Schneider and Max Glanz for their advice and their expertise. In addition, I thank our secretary Viktoria Blaschek for her support and her helpfulness.

Furthermore, I thank all the people from my office, Dr. Claudia Majer, Dr. Sebastian Jakob, Dr. Knud Seufert, Richard Steinacher, Felix Bischoff, Juan Li, Li Jiang, Bi Hai, Martin Schwarz and Martin Schäffer, for the nice atmosphere in our "Kofferraum". Moreover, I thank everybody from E20 for the support, for the scientific advice, for exciting stories from all over the world and the overall great and inspiring atmosphere in the group.

I am very thankful to the International Max Planck Research School of Advanced Photon Science (IMPRS) for the scholarship and the scientific program. I thank the IMPRS coordinators Dr. Vladislav S. Yakovlev, Dr. Nick Karpowicz and Prof. Dr. Matthias Kling and all the IMPRS students for the insightful and enjoyable meetings and I thank the secretary Monika Wild for her organizational talent and her enthusiasm.

For the fruitful and enriching collaboration I am grateful to Prof. Dr. Joachim Schnadt and Olesia Snezhkova. I also thank Dr. Thien H. Ngo for the synthesis of molecules. Furthermore, I am